Aeroelastic Modeling and CFD Simulation of Wind-Tunnel Scale Aspect Ratio 13.5 Common Research Model

Juntao Xiong*
KBR Wyle, Inc., Moffett Field, CA 94035
Nhan Nguyen†
NASA Ames Research Center, Moffett Field, CA 94035
Bret K. Stanford‡, *Robert E. Bartels*§
NASA Langley Research Center, Hampton, VA 23681

This paper presents an aeroelastic modeling and simulation study of an aspect ratio 13.5 wind-tunnel scale Common Research Model (CRM) with distributed flaps. A vortex-lattice VSPAERO model of the CRM model is developed. A transonic small disturbance/integral boundary layer correction method is implemented in the VSPAERO model to account for the transonic and viscous flow effects. The structural deformation of the CRM model is calculated using a NASTRAN equivalent beam model. The VSPAERO model is coupled to the NASTRAN equivalent beam model to provide a rapid aero-structural analysis. A validation of the VSPAERO aeroelastic model is conducted by comparing the results to FUN3D CFD aeroelastic simulation results. An aerodynamic database is generated using the developed VSPAERO aeroelastic model for the real-time drag optimization and maneuver load alleviation study of the wind-tunnel scale CRM model.

I. Introduction

The aircraft industry has been responding to the need for energy-efficient aircraft by redesigning airframes to be aerodynamically efficient, employing light-weight materials for aircraft structures and incorporating more energy-efficient aircraft engines. Reducing airframe operational empty weight (OEW) using advanced composite materials is one of the major considerations for improving energy efficiency. The Boeing 787 transport is an example of a modern airframe design that employs lightweight structures. Modern light-weight materials can provide less structural rigidity while maintaining sufficient load carrying capacity. As structural flexibility increases, aeroelastic interactions with aerodynamic forces and moments can alter aircraft aerodynamics significantly.[1] One option for managing the aeroelastic behavior of the aircraft is through control system design. The control system could be made to both suppress undesirable motion and shape the flexible structure in pursuit of improved performance goals.

The concept of variable-camber continuous trailing-edge flap (VCCTEF) for the active control of an aeroelastic wing developed by NASA was proposed by Nguyen in 2010.[2,3] The use of VCCTEF for the active control of a aeroelastic wing such as suppressing flutter, stabilizing the vehicle response to gusts, and reducing drag have been extensively studied.[1,4,5,6] Nguyen et al.[1] first demonstrated real-time drag optimization of the Common Research Model (CRM) in a low-speed wind tunnel experiment using the VCCTEF. In order to further discover the capability of the trailing-edge flap for the real-time drag optimization, maneuver load alleviation, and gust load alleviation, Boeing develops integrated adaptive wing control technologies for an aspect ratio 13.5 CRM with distributed trailing edge flaps under a NASA contract with the NASA Advanced Air Transport Technology (AATT) project. The aspect ratio 13.5 CRM is developed from the original aspect ratio 8.3 CRM.[7] The aspect ratio 13.5 CRM configuration employs a distributed mini-plain flap system which comprises 10 small trailing edge flaps positioned along the wing span. These mini-plain flaps can be used for a real-time drag optimization, maneuver load alleviation, and gust load alleviation strategies. Figure 1 illustrates the aspect ratio 13.5 wind-tunnel scale CRM configuration. To support the wind-tunnel experiment and the development of the real-time drag optimization and maneuver load alleviation algorithms using the mini-plain flaps, a computationally efficient aero-structural analysis solver is desired to generate a reliable aerodynamic database.

*Aerospace Engineer, Intelligent System Division, juntao.xiong@nasa.gov, AIAA Member
†Senior Research Scientist and Technical Group Lead, Intelligent Systems Division, nhan.t.nguyen@nasa.gov, Associate Fellow AIAA
‡Research Aerospace Engineer, Aeroelasticity Branch, bret.k.stanford@nasa.gov, AIAA Associate Fellow
§Research Aerospace Engineer, NASA Langley Research Center, MS 340, robert.e.bartels@nasa.gov, AIAA Senior Member

In this paper, a VSPAERO aeroelastic model of the wind-tunnel scale CRM model is developed. Transonic and viscous flow corrections for the steady-state aerodynamics are implemented in the vortex-lattice model using a transonic small disturbance (TSD) code called TSFOIL coupled to an in-house integral boundary layer (IBL) code.[8] The CRM model structural deformation is calculated using a NASTRAN equivalent beam model. The VSPAERO model is coupled to the NASTRAN equivalent beam model to provide a rapid aero-structural analysis. A high-fidelity CFD model of the CRM is developed using FUN3D to validate the VSPAERO model. At the end, an aerodynamic database is generated using the developed VSPAERO aeroelastic model for the real-time drag optimization and maneuver load alleviation study of the wind-tunnel scale CRM model.

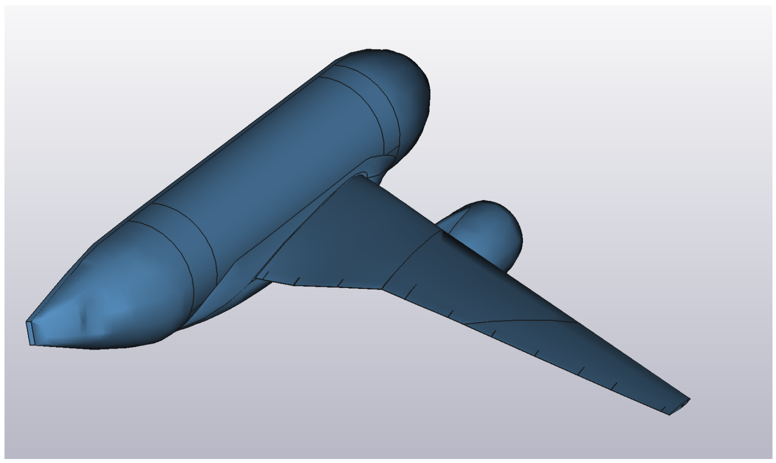

Figure 1 Common Research Model (CRM) Concept

II. Aerodynamic Modeling of the CRM

A. VSPAERO Model

In order to develop a rapid aeroelastic analysis that facilitates a vehicle MDAO process, a lower-fidelity aerodynamic model of the CRM is necessary. VSPAERO is a solver that includes both the vortex lattice method and the full panel method based on generalized vortex rings. The core VSPAERO solver is based on an agglomerated multi-pole approach, coupled with a preconditioned linear solver, to reduce solution times. Adaptive wakes, time-accurate, unsteady analyses, and propeller modeling are all supported. VSPAERO is part of the OpenVSP design package and is freely available under the NASA open source license.

Figure 2 illustrates the CRM geometry profiles used in the VSPAERO models. The wind-tunnel side walls are not included in the model. The free-stream condition is used for the VSPAEO model, which might introduce some modeling uncertainties. The fuselage and wind-tunnel side wall interference effects will be estimated using high-fidelity FUN3D simulation.

Figure 3 shows the differential pressure coefficient contour at Mach 0.85 and an angle of attack of 0° for the VSPAERO vortex-lattice model. The shed wakes are shown in Fig. 3 to illustrate the time-stepping wake capability in VSPAERO.

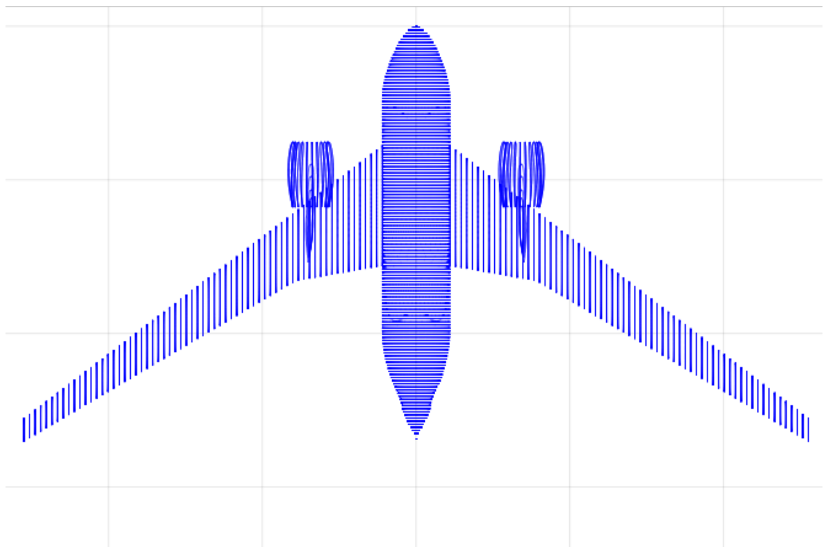

Figure 2 VSPAERO Model of CRM

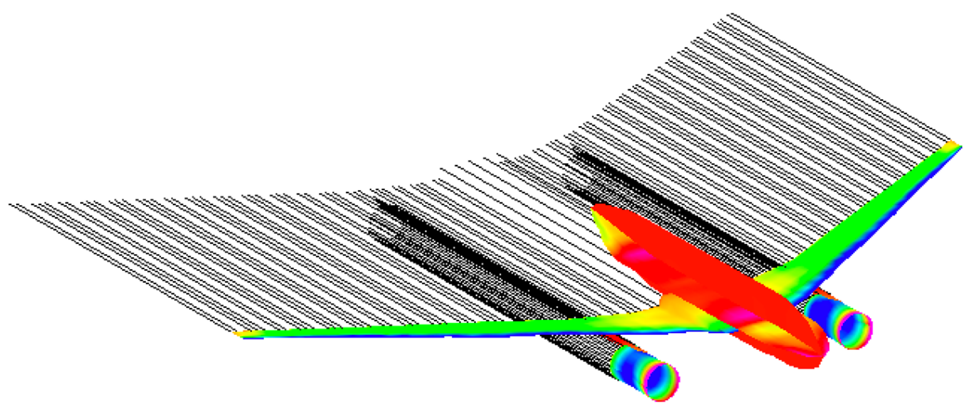

Figure 3 Differential Pressure Coefficient Contour of VSPAERO Vortex-Lattice Model of CRM

B. Transonic and Viscous Flow Correction

Because of the missing transonic effect in the linear potential flow method, a method for transonic and viscous corrections has been developed.[9,10,11] In this method, a full-configuration aerodynamic model can be based on the vortex-lattice or panel method. The wing is discretized into several spanwise sections at which the section lift coefficients computed by the potential flow method are used to correct for the transonic and viscous flow effects.[10,11] The transonic and viscous correction method is an iterative process to compute the incremental section lift coefficient due to transonic and viscous flow by a virtual re-twist of the individual wing sections to account for the accompanied change in the effective local angle of attack.[11] Implementation of the correction begins by initializing the virtual twist angle due to transonic and viscous corrections, $\gamma(y)$, to zero. The effective 2D angle of attack is then calculated for each airfoil using

$$\alpha_{2D}(y) = \alpha_0(y) + \frac{c_{l_{3D}}(y)}{c_{l_\alpha}} - \gamma(y), \quad (1)$$

where α_{2D} is the effective airfoil angle of attack, α_0 is the the airfoil zero-lift angle of attack, $c_{l_{3D}}$ is the section lift coefficient obtained via VSPAERO, and c_{l_α} is the 2D lift curve slope corrected for sweep as follows:

$$c_{l_\alpha} = \frac{2\pi}{\sqrt{1 - M_\Lambda^2}}. \quad (2)$$

Here, M_Λ is the Mach number based on the mid-chord sweep angle. Each airfoil is analyzed by the TSD/IBL model at the effective angle of attack. The transonic flow correction is handled by the transonic small disturbance (TSD) code TSFOIL.[12] This code is loosely coupled to the in-house integral boundary layer (IBL) code developed by Nguyen et al.[9] to correct for the viscous flow interaction with the transonic shock on an airfoil. Optionally, the correction method can be performed using the 2D Euler CFD code MSES with an integral boundary layer method developed by Mark Drela[13] as an available option.. The virtual twist angle is then updated for each section according to:

$$\gamma_{i+1}(y) = \gamma_i(y) + \frac{c_{l_{2D_i}}(y) - c_{l_{3D_i}}(y)}{c_{l_\alpha}}, \quad (3)$$

where $c_{l_{2D_i}}$ corresponds to the airfoil lift coefficient calculated by TSFOIL or MSES for iteration i.

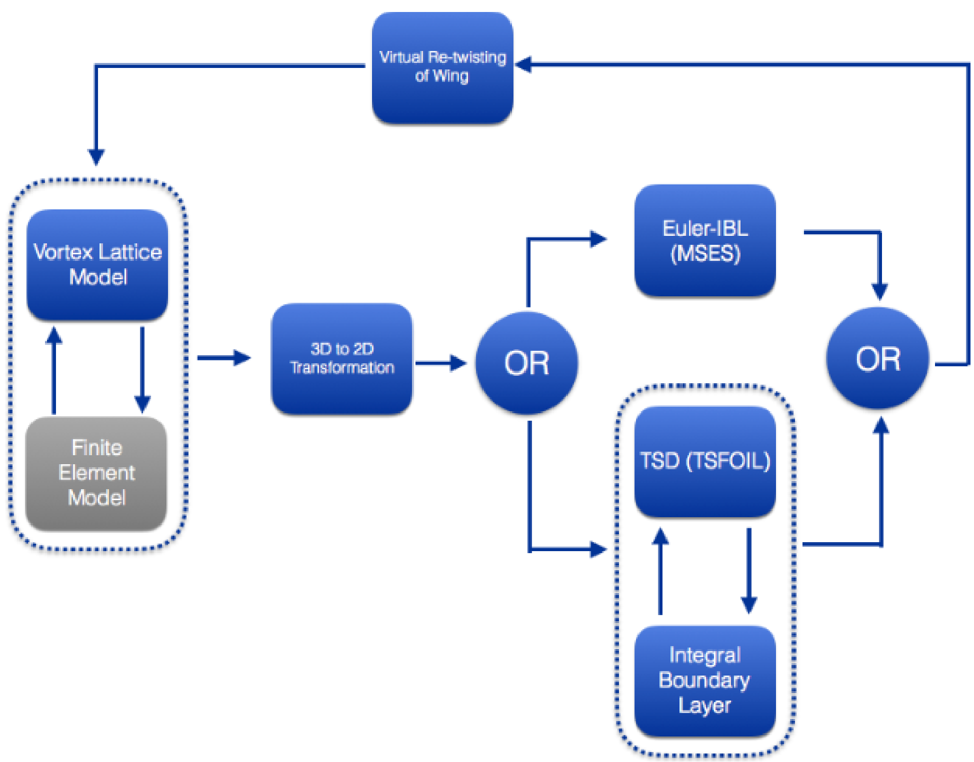

Figure 4 Transonic and Viscous Correction Flow Chart

The coupling and iterative update process is repeated until the 3D wing section lift and the 2D airfoil lift computed by the TSD/IBL correction method converge for all sections. Wave and friction drag are calculated by the TSD/IBL correction method, whereas lift. The sectional lift is also calculated by the TSD/IBL code from the surface pressure. The flow chart of the transonic and viscous flow correction method is shown in Figure 4.[11] An extensive validation of the transonic and viscous flow correction method has been performed to compare the method against RANS CFD solvers.[8] The solution method agrees quite well in terms of key aerodynamic parameters and pressure distribution results. The major advantage of using a potential flow method coupled to the transonic and viscous flow corrections is the computational efficiency of the method, which is several orders of magnitude faster than a typical RANS CFD solution. This computational efficiency becomes highly important when the potential flow solver is coupled to a structural analysis model for aero-structural modeling analysis.

C. Flap Gap Model

In order to model the flap gap area of the wind-tunnel scale CRM, two truncated airfoil profiles are used to represent each flap gap area. Figure 5 shows the close-up view of one of the flap gap. This flap gap model should be able to capture the lift-induced drag due to the lift circulation at the flap side edges. However, the skin friction drag on the exposed flap side edges in the flap gap area can not be captured by VSPAERO. A simple model is proposed to estimate the skin friction drag on the exposed flap edges. The flow in this narrow passage in the flap gap area may be assumed to be similar to the turbulent Couette flow. The skin friction drag can be calculated by Eq. 4.

$$C_{Dgap} = \frac{\sum_{i=1}^{10} S_{edge,i} C_{f,i} q_{gap,i}}{q_\infty S_{ref}}, \tag{4}$$

where S_{edge} is the exposed area of the flap side edges, C_f is the skin friction coefficient of the Couette flow, q_{gap} is the dynamic pressure of the Couette flow, q_∞ is the free stream dynamic pressure and S_{ref} is the CRM reference area. Since the flow in the narrow passage could be choked, the Mach number in the passage is assumed 1. The Couette flow Reynolds number based on the gap length is about $30,000$. The skin friction coefficient is about 0.005 for the Mach 1 compressible turbulent Couette flow from the experimental measurements.[14] Based on the turbulent Couette flow model, the skin friction drag is about 1.6 counts on the exposed flap edges in the flap gap areas.

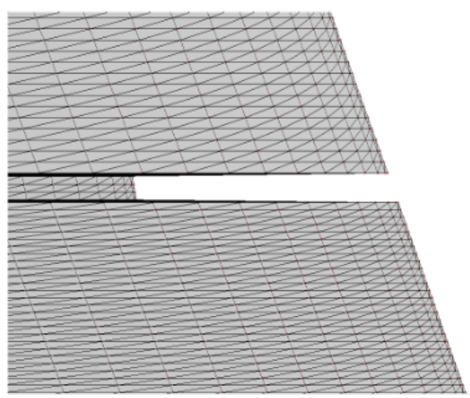

Figure 5 Close-up view of CRM Flap Gap Model

III. Structural Model of the CRM

A. NASTRAN Equivalent Beam Model

In order to calculate the CRM model aeroelastic deformation under aerodynamic force, a NASTRAN equivalent beam model is developed. The full CRM NASTRAN model is simplified to an equivalent beam model with 21 element along the wing elastic axis. Table 1 presents the equivalent beam parameter values. The NASTRAN linear elastic solution SOL101 is used to calculate the geometry deformation and rotation. The deformations and rotations under different constant loads are presented in Table 2 and compared with the full NASTRAN model for validation. In the first threes case a nodal force F_z along z direction, a moment M_x around x-axis, and a moment M_y around y-axis are applied at the wing tip, respectively. In the fourth case, the wing structure gravity force is considered. The NASTRAN output parameters u_z, ϕ_x, and ϕ_y indicate the displacement along the z direction, rotation about the x-axis, and rotation about the y-axis, respectively. The values calculated by the equivalent beam method agree well with the full NASTRAN model. The equivalent beam model therefore is validated and used to simulate the CRM model deformations.

Table 1 Equivalent Beam Parameters

Element	EI (lb-in^2)	GJ (lb-in^2)	Mass (lbs)
1	596090251.6	1225067992	39.164541
2	267767580.8	91703659.37	28.850588
3	156270585.9	50522605.94	28.131987
4	89598494.7	32990812.77	18.031611
5	61177361.01	40996289.7	21.166652
6	35659938.93	38857814.23	16.932877
7	26084630.94	16181777.16	14.105819
8	20890266.82	12680743.47	11.4122424
9	17082562.69	8971640.126	10.1651251
10	14590027.89	7288799.822	11.8637597
11	11292642.2	5877978.602	7.6045671
12	8803458.902	3787547.159	9.4835104
13	7035359.905	3286371.728	6.9069494
14	5340154.359	2664193.349	7.5238423
15	3929904.677	1782682.863	6.0452665
16	3079425.007	3464481.863	6.4351118
17	1997458.824	1232705.53	4.8415692
18	1262128.998	637840.7779	5.2699855
19	840961.4978	354115.9213	2.4023519
20	567207.5985	221117.8909	1.8341973
21	304923.1871	121006.2934	2.2223344

Table 2 Deformation and Rotation under Constant Loads

Case	F_z (lb)	M_x (lb-in)	M_y (lb-in)	u_{zFull} (in)	ϕ_{xFull}	ϕ_{yFull}	$u_{zEquivalent}$	$\phi_{xEquivalent}$	$\phi_{yEquivalent}$
1	50	0	0	3.9732	0.0645	-0.0444	3.9449	0.0655	-0.0452
2	0	2000	0	2.5815	0.2066	0.0881	2.6215	0.2066	0.0880
3	0	0	2000	-1.7778	0.0881	0.2739	-1.8062	0.0880	0.2738
4	Self Weight	0	0	-1.6489	-0.0148	0.0089	-1.6220	-0.0154	0.0106

B. Static Aeroelastic Analysis

A basic schematic of the aeroelastic modeling strategy is depicted by Fig. 6. The VSPAERO model is couple to the NASTRAN equivalent beam model to provide a rapid aero-structural analysis. At each iteration of the aeroelastic simulation the aerodynamic force F_z and moments M_x and M_y converted from wing sectional lift and pitching moment are applied to the NASTRAN equivalent beam model.

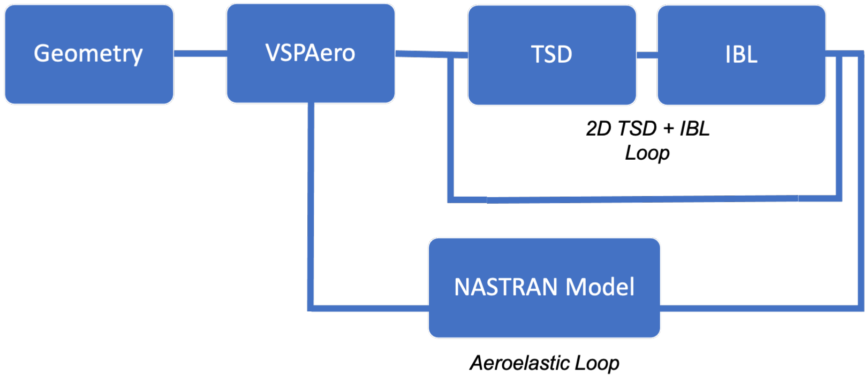

Figure 6 Aeroelastic Simulation Scheme Flow Chart

The wing coordinate system is shown in the following Fig. 7.

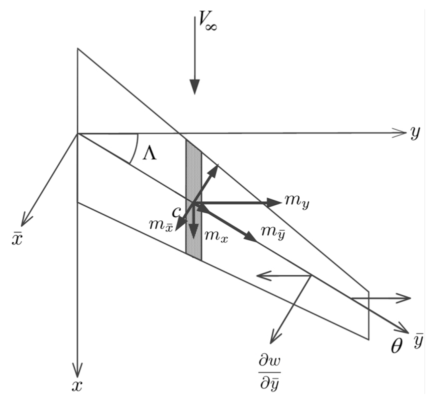

Figure 7 Wing Coordinate System

The distributed force and moments in the elastic axis coordinate system $(\bar{x}, \bar{y}, z)$ due to aerodynamics are given by

$$f_z = c_l q_\infty c \cos\Lambda \tag{5}$$

$$m_{\bar{x}} = \left[\left(c_{m_{ac}} + c_{m_x}\tan\Lambda\right) q_\infty c^2 + c_l q_\infty c e\right]\cos\Lambda\sin\Lambda \tag{6}$$

$$m_{\bar{y}} = \left[\left(c_{m_{ac}} + c_{m_x}\tan\Lambda\right) q_\infty c^2 + c_l q_\infty c e\right]\cos^2\Lambda \tag{7}$$

The hermite cubic interpolation function for the beam element in the finite-element method is

$$\mathbf{N}_w^{(i)^\top}(\bar{y}_i) = \begin{bmatrix} 1 - 3\left(\frac{\bar{y}_i}{l_i}\right)^2 + 2\left(\frac{\bar{y}_i}{l_i}\right)^3 \\ l_i\left[\frac{\bar{y}_i}{l_i} - 2\left(\frac{\bar{y}_i}{l_i}\right)^2 + \left(\frac{\bar{y}_i}{l_i}\right)^3\right] \\ 3\left(\frac{\bar{y}_i}{l_i}\right)^2 - 2\left(\frac{\bar{y}_i}{l_i}\right)^3 \\ l_i\left[-\left(\frac{\bar{y}_i}{l_i}\right)^2 + \left(\frac{\bar{y}_i}{l_i}\right)^3\right] \end{bmatrix} \tag{8}$$

$$\frac{d\mathbf{N}_w^{(i)^\top}(\bar{y}_i)}{d\bar{y}} = \begin{bmatrix} \frac{1}{l_i}\left[-6\left(\frac{\bar{y}_i}{l_i}\right) + 6\left(\frac{\bar{y}_i}{l_i}\right)^2\right] \\ 1 - 4\left(\frac{\bar{y}_i}{l_i}\right) + 3\left(\frac{\bar{y}_i}{l_i}\right)^2 \\ \frac{1}{l_i}\left[6\left(\frac{\bar{y}_i}{l_i}\right) - 6\left(\frac{\bar{y}_i}{l_i}\right)^2\right] \\ -2\left(\frac{\bar{y}_i}{l_i}\right) + 3\left(\frac{\bar{y}_i}{l_i}\right)^2 \end{bmatrix} \tag{9}$$

The elemental force vector due to bending in the element coordinate system $(\bar{x}, \bar{y}, z)$ is

$$\mathbf{F}_w^{(i)} = \begin{bmatrix} F_{z_1} \\ M_{\bar{x}_1} \\ F_{z_2} \\ M_{\bar{x}_2} \end{bmatrix} = \int_0^{l_i} \mathbf{N}_w^{(i)^\top}(\bar{y}_i)\left(f_z + \frac{dm_{\bar{x}}}{d\bar{y}_i}\right) d\bar{y}_i = \int_0^{l_i} \mathbf{N}_w^{(i)^\top}(\bar{y}_i)\, f_z d\bar{y}_i - \int_0^{l_i} \frac{d\mathbf{N}_w^{(i)^\top}(\bar{y}_i)}{d\bar{y}} m_{\bar{x}} d\bar{y}_i \tag{10}$$

The elemental force vector due to bending in the aircraft coordinate system (x, y, z) is

$$\mathbf{F}_w^{(i)} = \begin{bmatrix} F_{z_1} \\ M_{x_1} \\ M_{y_1} \\ F_{z_2} \\ M_{x_2} \\ M_{y_2} \end{bmatrix} = \begin{bmatrix} F_{z_1} \\ M_{\bar{x}_1}\cos\Lambda \\ -M_{\bar{x}_1}\sin\Lambda \\ F_{z_2} \\ M_{\bar{x}_2}\cos\Lambda \\ -M_{\bar{x}_2}\sin\Lambda \end{bmatrix} \tag{11}$$

The linear interpolation function for the rod element in the finite-element method is

$$\mathbf{N}_\theta^{(i)^\top}(\bar{y}_i) = \begin{bmatrix} 1 - \frac{x_i}{l_i} \\ \frac{x_i}{l_i} \end{bmatrix} \tag{12}$$

The elemental force vector due to torsion in the element coordinate system $(\bar{x}, \bar{y}, z)$ is

$$\mathbf{F}_\theta^{(i)} = \begin{bmatrix} M_{\bar{y}_1} \\ M_{\bar{y}_2} \end{bmatrix} = \int_0^{l_i} \mathbf{N}_\theta^{(i)^\top}(\bar{y}_i)\, m_{\bar{y}} d\bar{y}_i \tag{13}$$

The elemental force vector due to torsion in the aircraft coordinate system (x, y, z) is

$$\mathbf{F}_\theta^{(i)} = \begin{bmatrix} M_{x_1} \\ M_{y_1} \\ M_{x_2} \\ M_{y_2} \end{bmatrix} = \begin{bmatrix} M_{\bar{y}_1}\sin\Lambda \\ M_{\bar{y}_1}\cos\Lambda \\ M_{\bar{y}_2}\sin\Lambda \\ M_{\bar{y}_2}\cos\Lambda \end{bmatrix} \tag{14}$$

The total element force vector in the aircraft coordinate system (x, y, z) is

$$\mathbf{F}_w^{(i)} = \begin{bmatrix} F_{z_1} \\ M_{x_1} \\ M_{y_1} \\ F_{z_2} \\ M_{x_2} \\ M_{y_2} \end{bmatrix} = \begin{bmatrix} F_{z_1} \\ M_{\bar{x}_1}\cos\Lambda + M_{\bar{y}_1}\sin\Lambda \\ -M_{\bar{x}_1}\sin\Lambda + M_{\bar{y}_1}\cos\Lambda \\ F_{z_2} \\ M_{\bar{x}_2}\cos\Lambda + M_{\bar{y}_2}\sin\Lambda \\ -M_{\bar{x}_2}\sin\Lambda + M_{\bar{y}_2}\cos\Lambda \end{bmatrix} \tag{15}$$

The nodal forces on an element is shown in the following Fig. 8

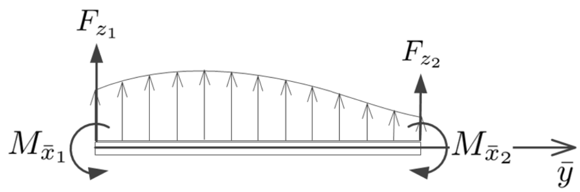

Figure 8   Wing Nodal Force Flow Chart

The NASTRAN SOL 101 solution provides the structural deformation of the CRM wing. Figure 9 shows the CRM wing bending deflection and twist at Mach 0.80, 0° angle of attack, and the dynamic pressure q_∞ = 200 psf. Figure 10 shows the deformed CRM VSPAERO model wing deflects under the aerodynamic loading. Figure 11 shows the CRM wing bending deflections for a varying dynamic pressure from 200 to 450 psf at Mach 0.8 and 0° angle of attack. The CRM wing tip deflection reaches a constant value asymptotic as the dynamic pressure increases.

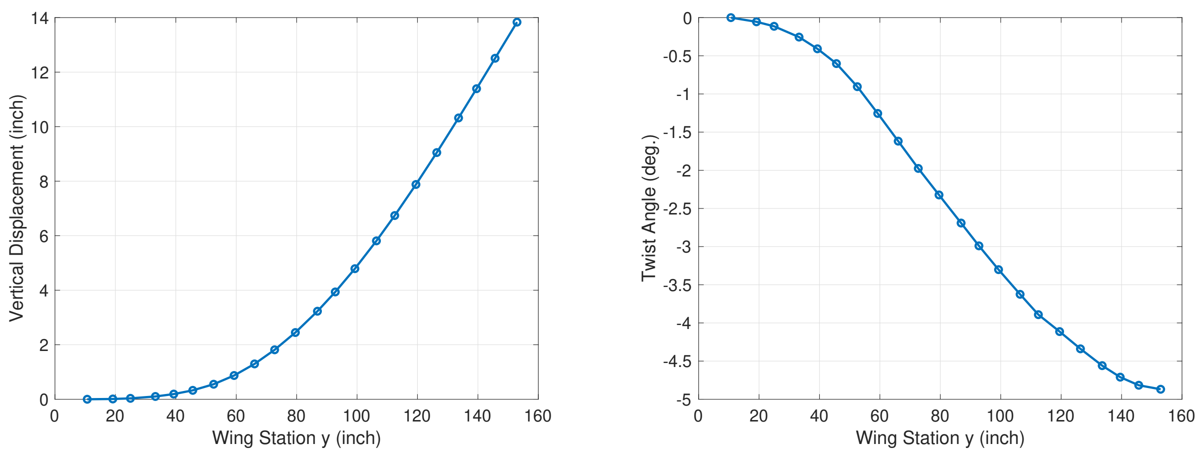

(a) Bending Deflection

(b) Twist Angle

Figure 9   CRM Wing Bending Deflection and Twist at Mach 0.80, α = 0°, and q_∞ = 200 psf

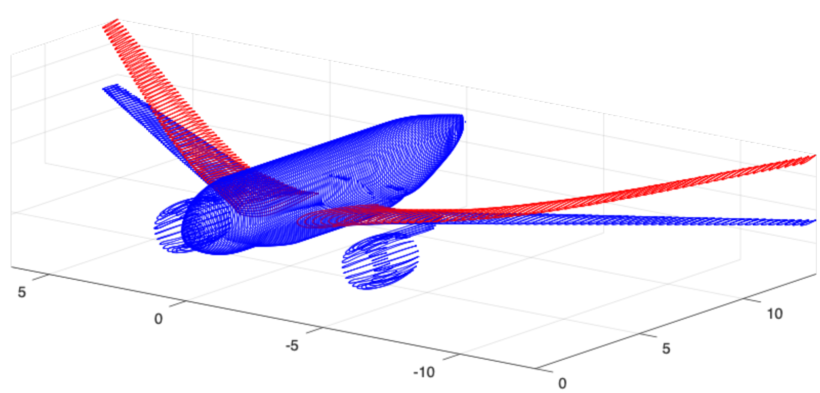

Figure 10   VSPAERO Model of Deformed CRM Flow Chart

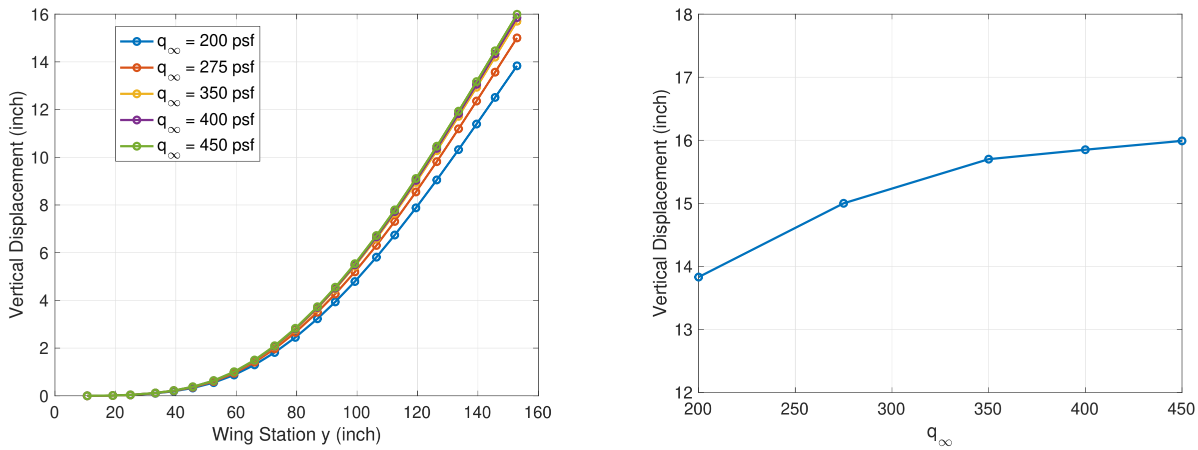

(a) Bending Deflection

(b) Twist Angle

Figure 11 CRM Wing Bending Deflection under varying Dynamic Pressure

IV. High-fidelity CFD Simulation

To validate the developed VSPAERO aeroelastic model, a validation study using high-fidelity CFD solver FUN3D is performed. FUN3D[15,16] solves the unsteady three-dimensional Navier-Stokes equations on mixed-element grids using a vertices-centered finite-volume method. Information exchange for flow computation on different partitions using multiple CPUs is implemented through the MPI (Message Passing Interface) protocol. It employs an implicit upwind algorithm in which the inviscid fluxes are obtained with a flux-difference-splitting scheme. At interfaces that delimits the neighboring control volumes, the inviscid fluxes are computed using an approximate Riemann solver based on the values on either side of the interfaces. The Roe flux difference splitting[17] is used in the current study. For second-order accuracy, the interface values are obtained by extrapolation of the control volume centroidal values, based on the gradients computed at the mesh vertices, using an unweighted least squares technique. The Venkatakrishnan[18] limiter is used in the current study to limit the reconstructed values when necessary. In this study, the tetrahedral mesh with prism layers is used. In FUN3D, for tetrahedral meshes, the full viscous fluxes are discretized using a finite-volume formulation in which the required velocity gradients on the dual faces are computed using the Green-Gauss theorem. The solution at each time-step is updated with a backward Euler time-differencing scheme. At each time step, the system of equations is approximately solved with either a multi-color point-implicit procedure or an implicit-line relaxation scheme. Local time-step scaling is employed to accelerate convergence to steady-state. To model turbulent flows, the one-equation model of Spalart-Allmaras[19] (S-A) is used in this study.

A.Fuselage and Side Wall Interference Effects

During the initial study, Two FUN3D simulations are conducted to examine the wall interference effects between the fuselage and the test section side wall. The two FUN3D simulations are for the rigid CRM geometry with and without the test section wall.

For the geometry with the test section side wall, the volume mesh includes a solid wall extended beyond the CRM geometry. The geometry of the test section side wall is 8 ft in length and 16 in height. The volume mesh is shown in Fig.12. The total number of the nodes for the mesh is about 57 million. The volume mesh is comprised of tetrahedral elements and a prism layer near the wall. The prism layer is used to resolve the turbulent boundary layer. The $y+$ of the first cell from the wall is less than 1.

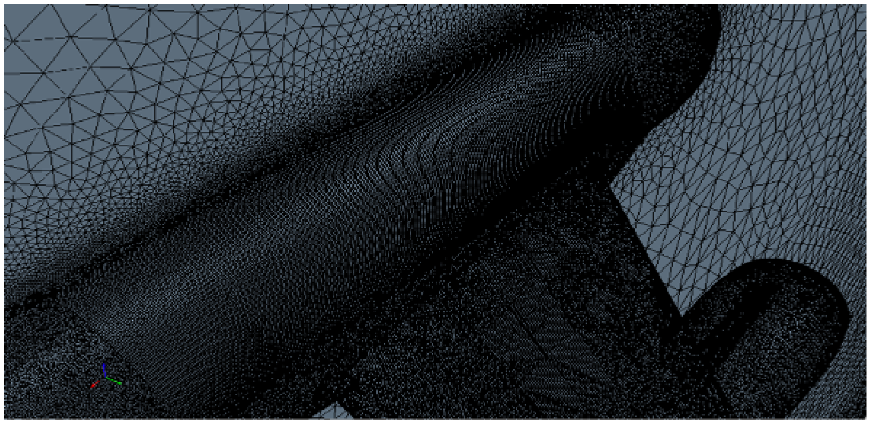

Figure 12 Close View of CRM CFD Mesh

Figure 13 shows the pressure comparison between the simulations with and without the side wall at Mach 0.85, the dynamic pressure of 230 psf, and −0.5° angle of attack. With the side wall, the shock wave turns much weaker on the fuselage surface. The lift coefficient and drag polar comparison are presented in the Fig. 14. The lift coefficient is reduced about 0.02 at the same angle of attack when the side wall is considered. However, the drag coefficient is slightly increased when the side wall is considered. For this study the effect of wall interference on the flow at the wing tip is not studied. Future work may consider including the wing tip side wall in the model.

The VSPAERO simulation results for the rigid CRM without side wall are also shown in the Fig. 14. The VSPAERO simulation results match well with the FUN3D simulation results for the rigid CRM. The incremental lift and drag coefficients correction caused by the side wall can be estimated with,

$$\Delta C_L = C_{L\ with\ wall} - C_{L\ without\ wall} \tag{16}$$

$$\Delta C_D = C_{D\ with\ wall} - C_{D\ without\ wall} \tag{17}$$

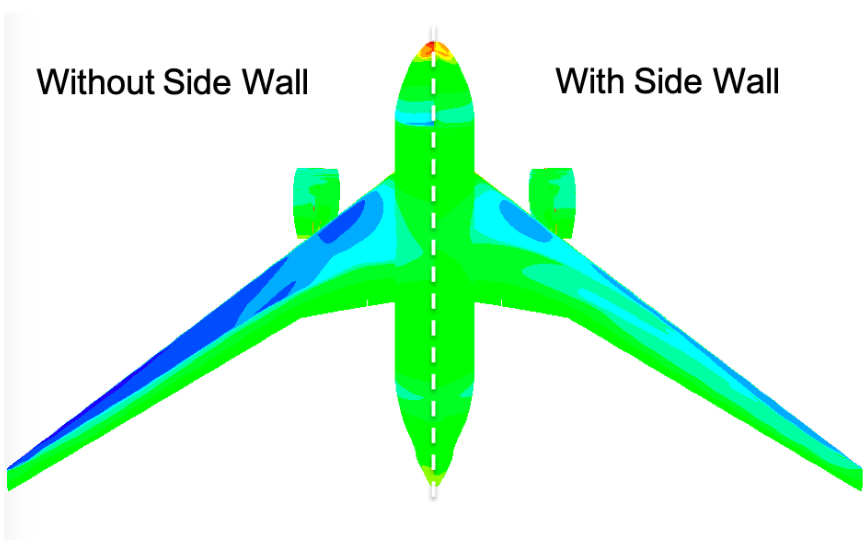

Figure 13 Pressure Coefficient Contour on the CRM Rigid Geometry Surfaces at Mach 0.85 and $\alpha = -0.5°$

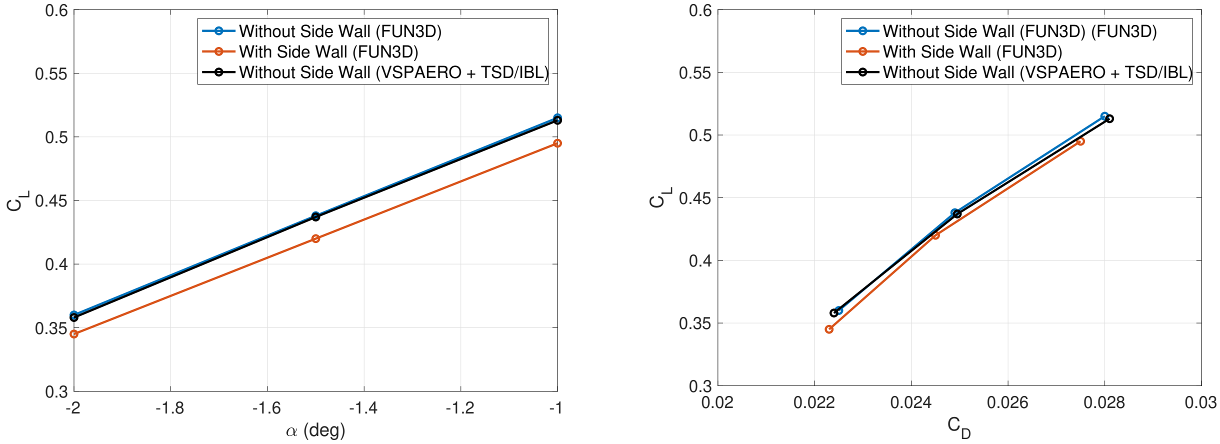

(a) Lift Curve

(b) Drag Polar

Figure 14 CRM Rigid Geometry Aerodynamic Performance at Mach 0.85.

B.FUN3D Aeroelastic Simulation

The static aeroelastic simulation module in FUN3D is used for the aeroelastic simulation. The mode shapes are extracted from full NASTRAN model. Figure 15 shows the wind-tunnel scale CRM first six mode shapes. Figure 16 shows the pressure coefficient contour on the CRM surfaces at Mach 0.85, $q_\infty = 230$ psf, and $\alpha = 0°$. The CRM wing is deflected to the upward 15.18 inches and the shock wave on the wing surface turns weaker.

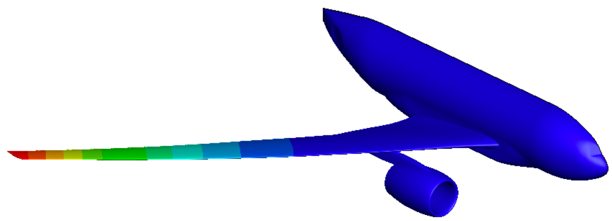

(a) 1st Mod

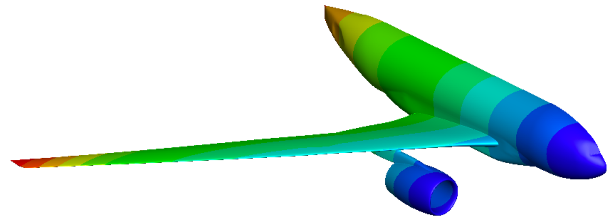

(b) 2nd Mode

(c) 3rd Mode

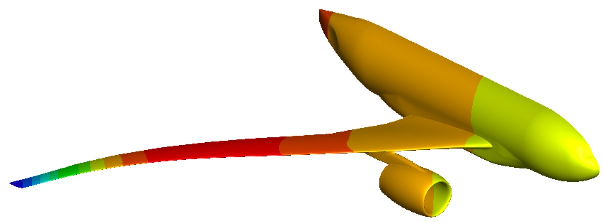

(d) 4th Mode

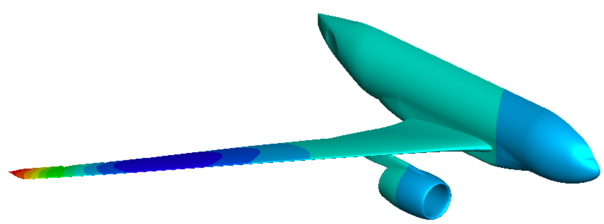

(e) 5th Mode

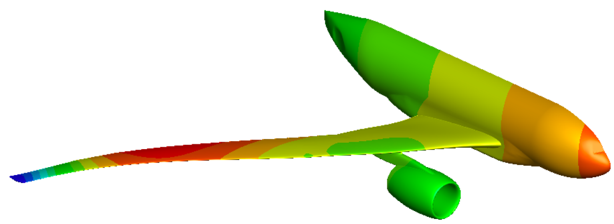

(f) 6th Mode

Figure 15 CRM Mode Shapes

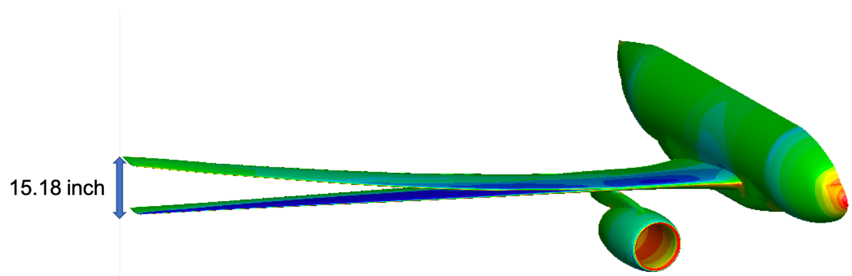

Figure 16 Pressure Coefficient Contour on the CRM Surfaces at Mach 0.85, $q_\infty = 230$ psf and $\alpha = 0°$

V. CRM Aeroelastic Simulation Results

A. VSPAERO Model Validation

First, the VSPAERO model coupled with NASTRAN equivalent beam is validated with the high-fidelity FUN3D simulation results. The fuselage side wall and wing tip side wall are not included in the VSPAERO and FUN3D aeroelastic simulations. The simulated tunnel condition is at Mach 0.85 and $q_\infty = 230$ psf . Figure 17 compares the lift, drag, lift-to-drag ratio, and wing tip deflections calculated by the VSPAERO model and FUN3D for the CRM with zero flap deflection angles. The converged solution for the VSPAERO model can not be obtained when the angle of attack is higher than 6 degrees. The data calculated by the VSPAERO model show excellent agreement with the FUN3D simulation especially when the lift is less than 0.8. The discrepancy increases as the lift coefficient increases, which might be caused by a flow separation. The current VSPAERO model has some limitation in its ability to predict the flow separation, but overall the VSPAERO model demonstrates an excellent predictive capability at a much lower computational cost when compared to FUN3D aeroelastic simulations. Therefore, it is appropriate to use the VSAPERO model to generate the aerodynamic database for the wind-tunnel scale CRM, considering the relative accuracy and computational efficiency.

Another aspect of the VSPAERO modeling effort is the consideration of the distributed flap system. In the VSPAERO model, the flap edges are modeled explicitly in the model. The flap gap model accounts for inviscid drag due to the flow circulation around the flap side edges. The viscous drag due to the flow through the flap gap area is modeled by the compressible Couette flow as discussed. This model predicts an additional viscous drag of 1.6 counts by all the flap gaps. In contrast, the flap gap modeling in FUN3D CFD model is computationally prohibitive. The flap gap has a width of 0.08% of the wing span on the average. To model the viscous flow, a fine mesh for the boundary layer must be incorporated in the flap gap regions for the 10 mini-plain flaps. This would significantly increase the mesh resolution and the mesh generation and refinement could become an extremely laborious process.

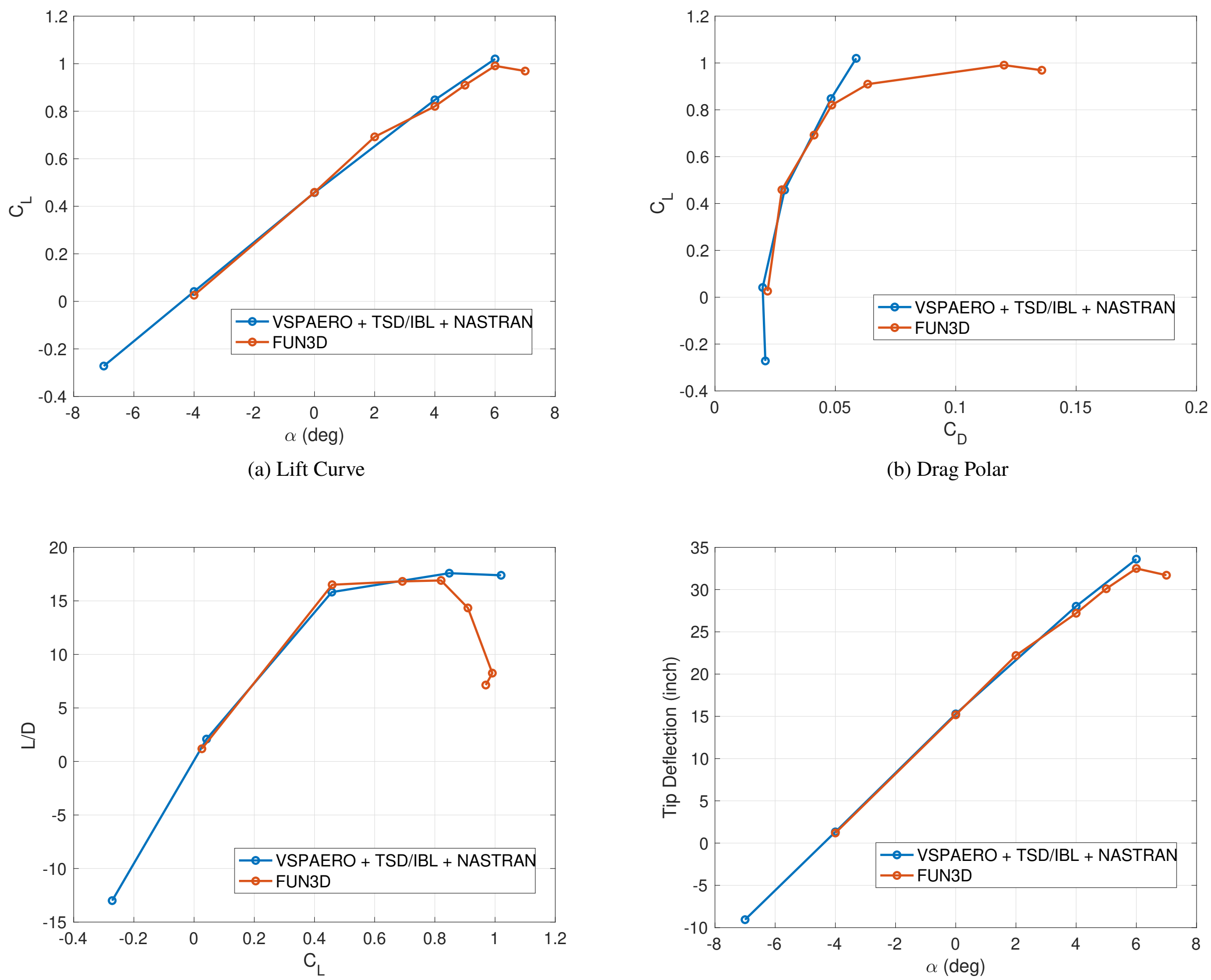

(a) Lift Curve

(b) Drag Polar

(c) Lift-to-Drag Ratio

(d) Wing Tip Deflection

Figure 17 CRM Aerodynamic Performance at Mach 0.85 and $q_\infty = 230$ psf.

B. Aerodynamic Database

The VSPAERO model is used to generate an aerodynamic database for five wind tunnel conditions at Mach 0.70 and q_∞ = 230 psf, Mach 0.80 and q_∞ = 200 psf, Mach 0.80 and q_∞ = 230 ps, Mach 0.85 and q_∞ = 230 psf, and Mach 0.85 and q_∞ = 140 psf. There are 10 mini-plain trailing edge flaps on the CRM. Figure 18 shows the planform of the flaps. The red line in the figure represents the flaps. Figure 19 illustrates the flap deflection definition. The deflection angle is positive when the flap is deflected downward.

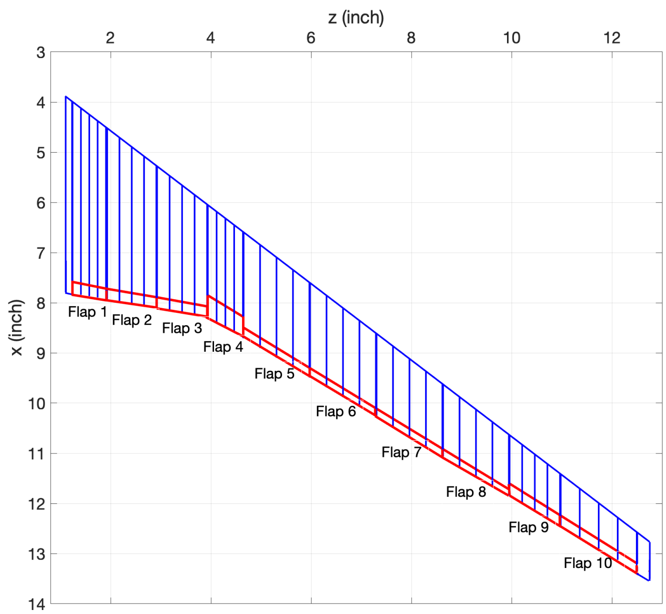

Figure 18 CRM Flap Planform

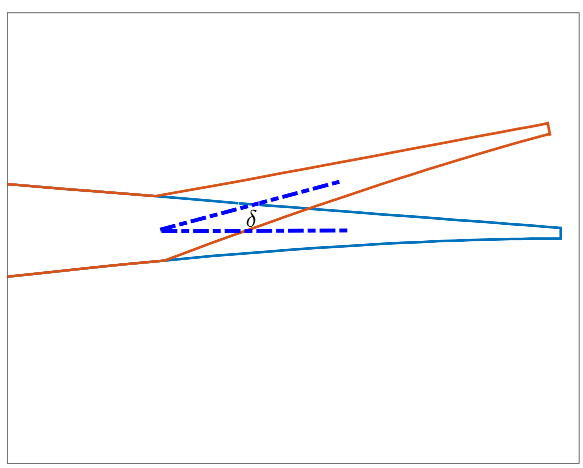

Figure 19 CRM Flap Deflection Definition

Figure 20 shows the lift, drag, moment, drag polar, and lift to drag ratio and Figure 21 shows the wing tip deflection, wing tip twist angle, wing root bending moment, and wing root twist moment for Mach 0.7 and $q_\infty = 230$ psf at the angle of attacks of $-6°$, $-4°$, $0°$, $4°$, and $6°$. The incremental aerodynamic and structural data are presented in the Appendix A. The flap deflection angle are from $-20°$ to $20°$. The incremental changes of lift and moment are generally linear with respect to the flap deflection. The incremental changes of drag coefficient follows a parabolic relationship. The incremental changes of the wing root bending moment and twist moment are also linear with respect to the flap deflection.

Figure 22 shows the lift, drag, moment, drag polar, and lift to drag ratio and Figure 23 shows the wing tip deflection, wing tip twist angle, wing root bending moment, and wing root twist moment for Mach 0.8 and $q_\infty = 200$ psf. The incremental aerodynamic and structural data are presented in the Appendix B.

Figure 24 shows the lift, drag, moment, drag polar, and lift to drag ratio and Figure 25 shows the wing tip deflection, wing tip twist angle, wing root bending moment, and wing root twist moment for Mach 0.8 and $q_\infty = 230$ psf. The incremental aerodynamic and structural data are presented in the Appendix C.

Figure 26 shows the lift, drag, moment, drag polar, and lift to drag ratio and Figure 27 shows the wing tip deflection, wing tip twist angle, wing root bending moment, and wing root twist moment for Mach 0.85 and $q_\infty = 230$ psf. The incremental aerodynamic and structural data are presented in the Appendix D.

Figure 28 shows the lift, drag, moment, drag polar, and lift to drag ratio and Figure 29 shows the wing tip deflection, wing tip twist angle, wing root bending moment, and wing root twist moment for Mach 0.85 and $q_\infty = 140$ psf. The incremental aerodynamic and structural data are presented in the Appendix E.

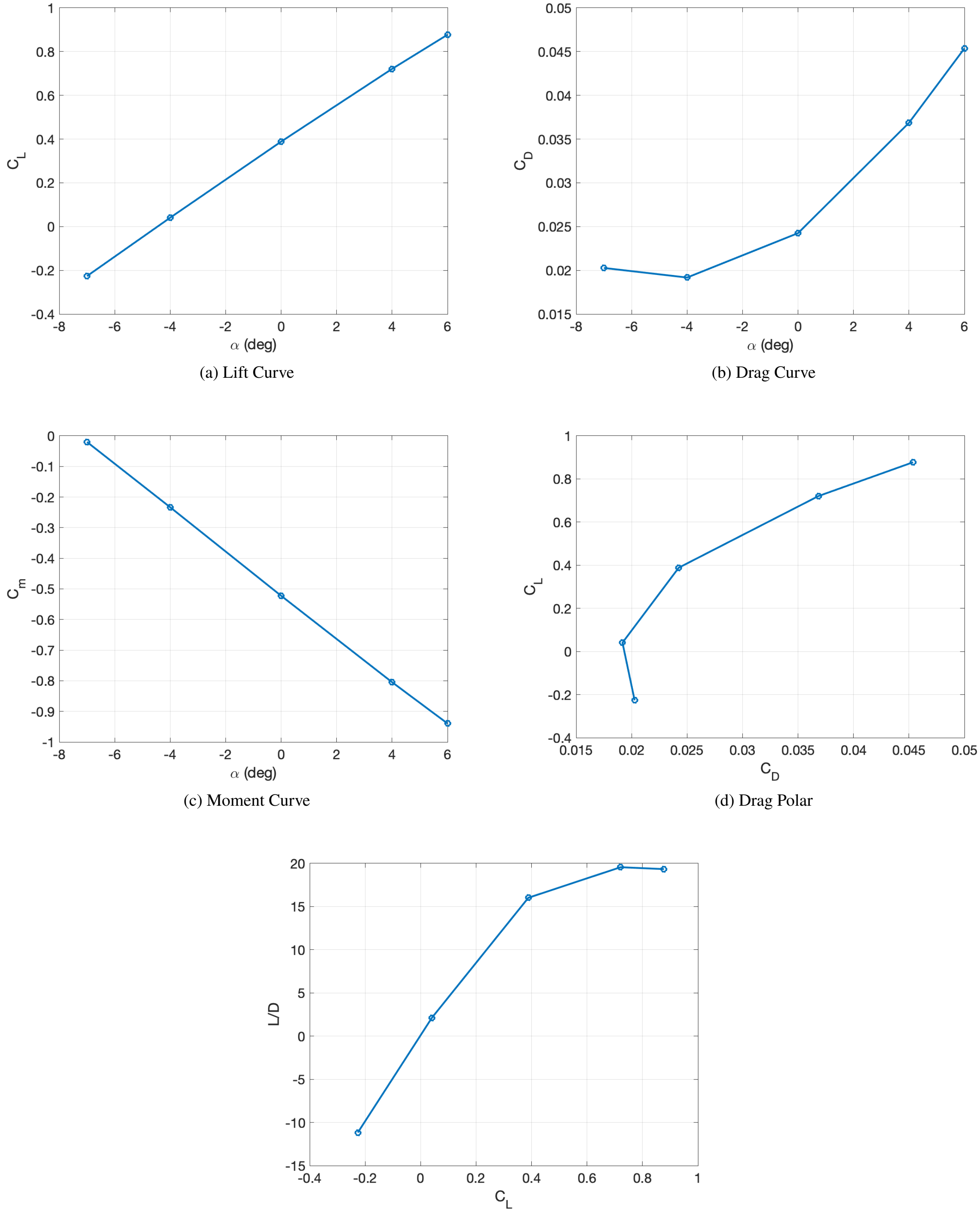

(a) Lift Curve

(b) Drag Curve

(c) Moment Curve

(d) Drag Polar

(e) Lift to Drag Ratio

Figure 20 CRM Aerodynamic Data at Mach 0.70 and q_∞ = 230 **psf**

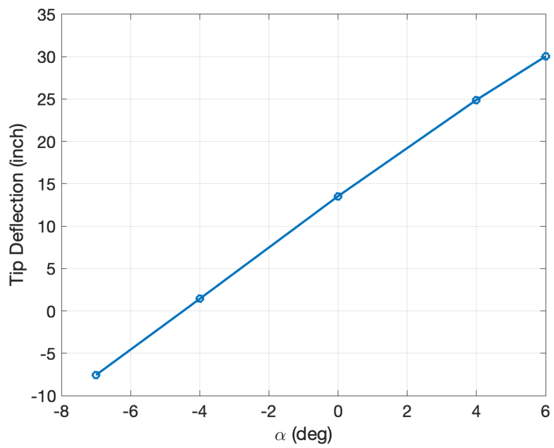

(a) Tip Deflection

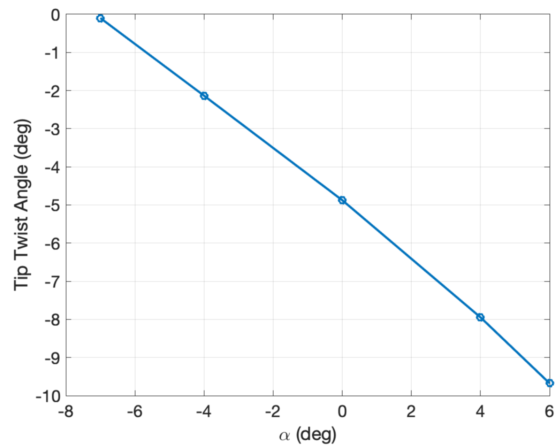

(b) Tip Twist Angle

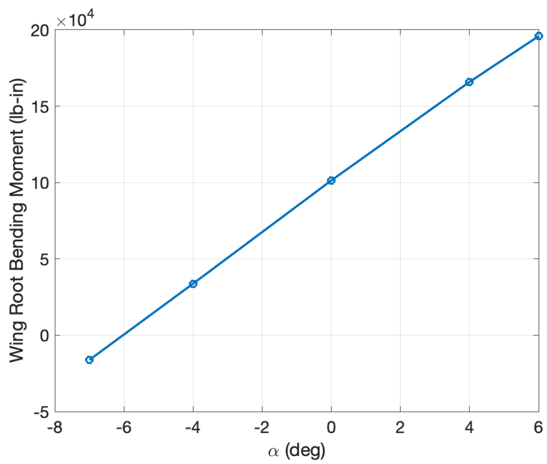

(c) Wing Root Bending Moment

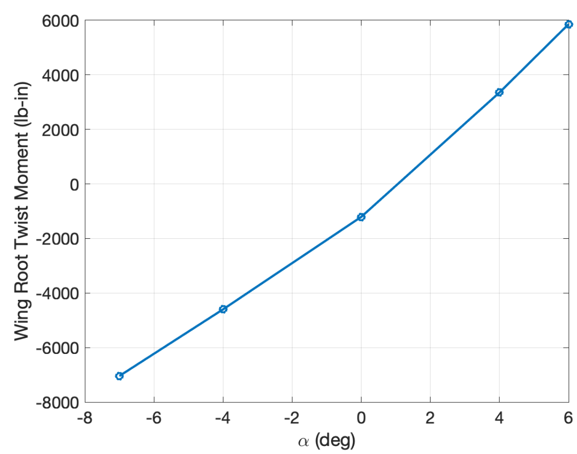

(d) Wing Root Twist Moment

Figure 21 CRM Structural Data at Mach 0.70 and q_∞ = 230 psf

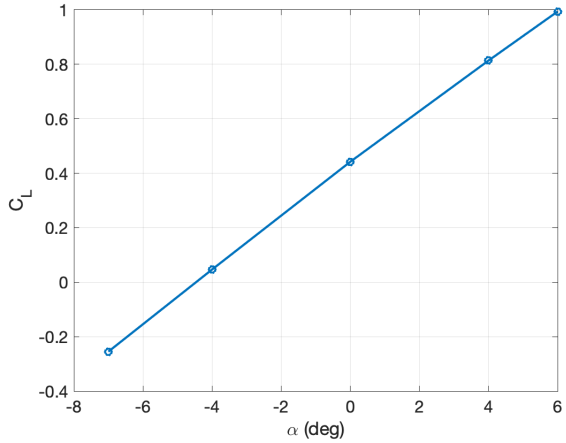

(a) Lift Curve

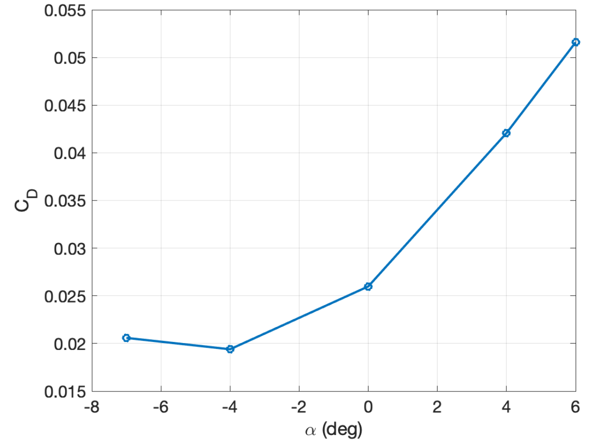

(b) Drag Curve

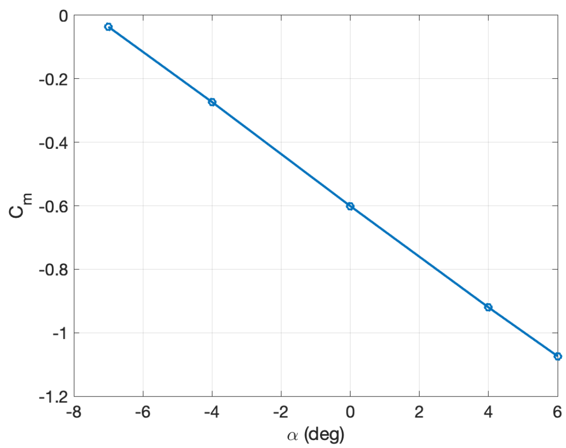

(c) Moment Curve

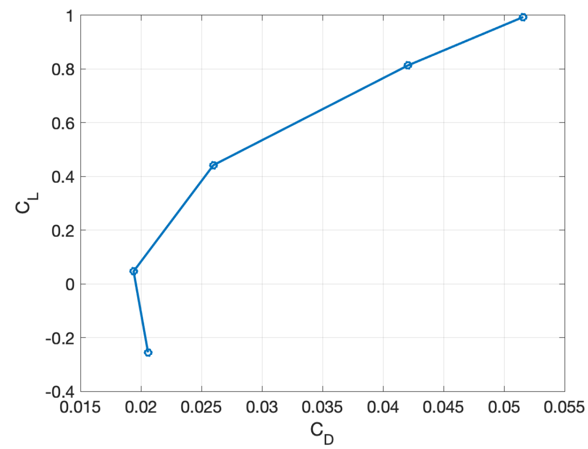

(d) Drag Polar

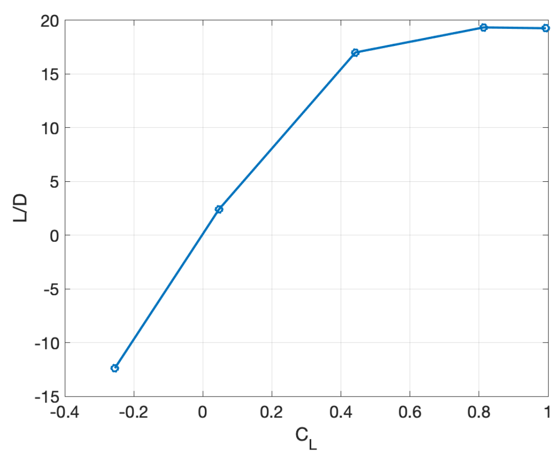

(e) Lift to Drag Ratio

Figure 22 CRM Aerodynamic Data at Mach 0.80 and $q_\infty = 200$ **psf**

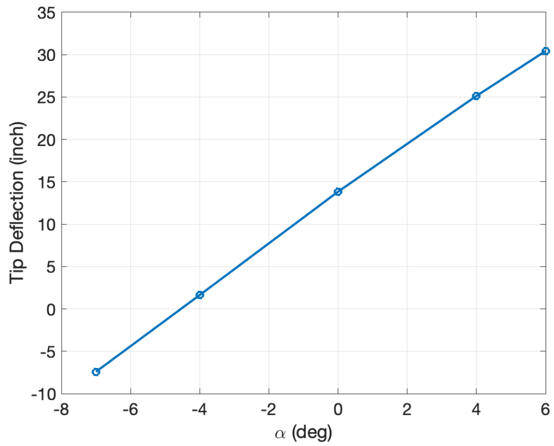

(a) Tip Deflection

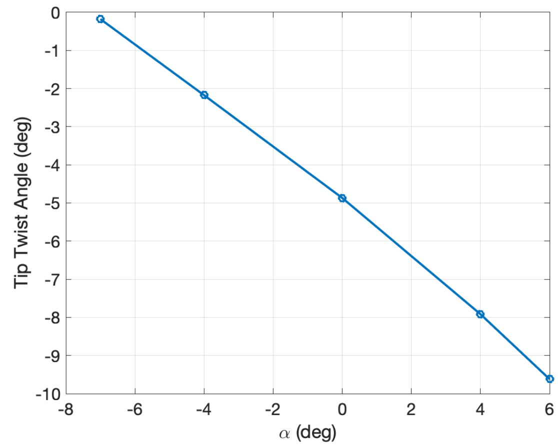

(b) Tip Twist Angle

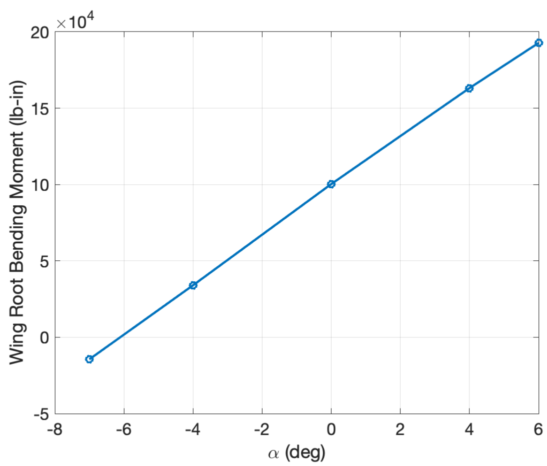

(c) Wing Root Bending Moment

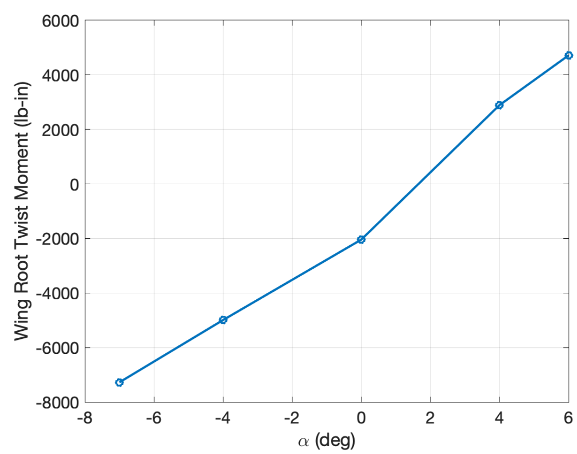

(d) Wing Root Twist Moment

Figure 23 CRM Structural Data at Mach 0.80 and $q_\infty = 200$ **psf**

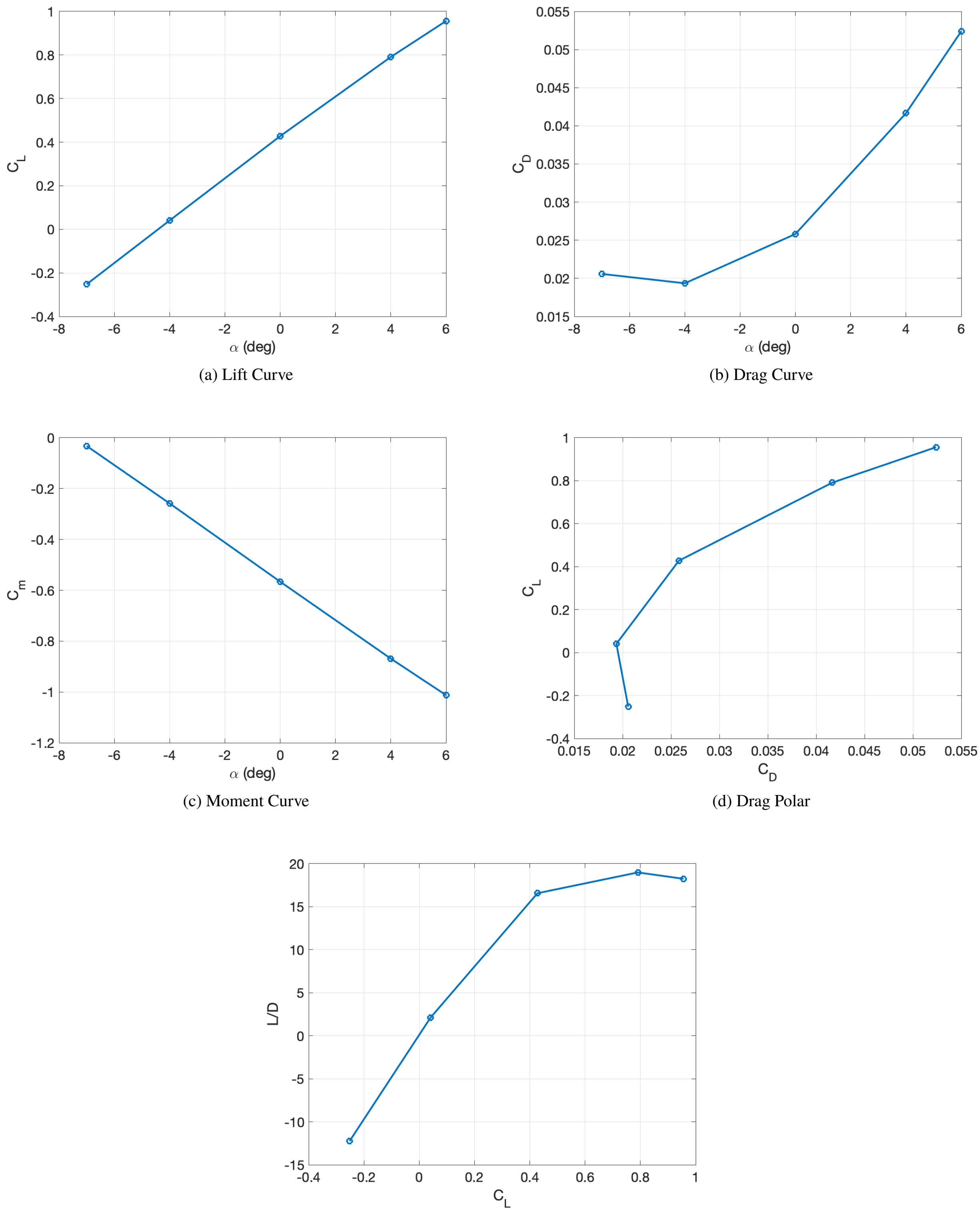

(a) Lift Curve

(b) Drag Curve

(c) Moment Curve

(d) Drag Polar

(e) Lift to Drag Ratio

Figure 24 CRM Aerodynamic Data at Mach 0.80 and q_∞ = 230 psf

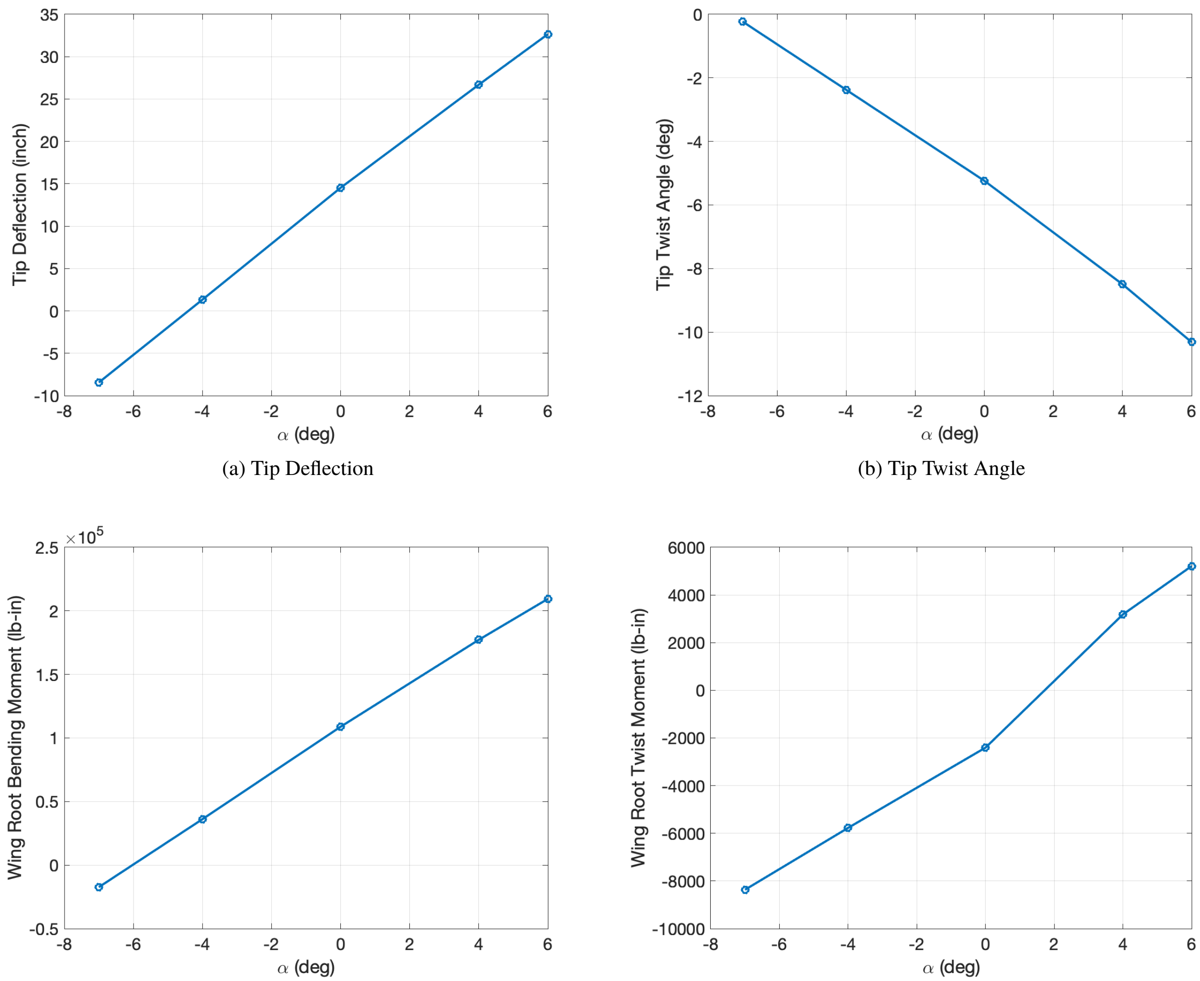

(a) Tip Deflection

(b) Tip Twist Angle

(c) Wing Root Bending Moment

(d) Wing Root Twist Moment

Figure 25 CRM Structural Data at Mach 0.80 and q_∞ = 230 psf

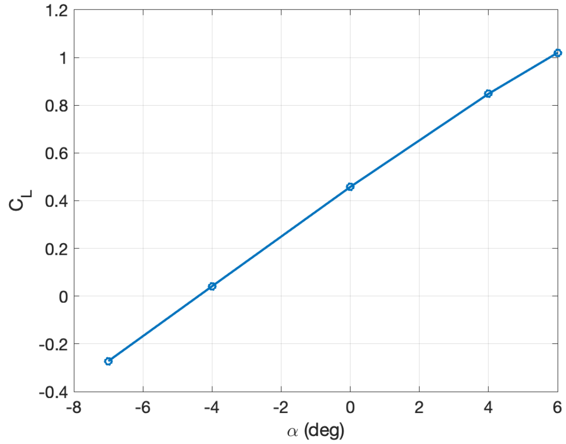

(a) Lift Curve

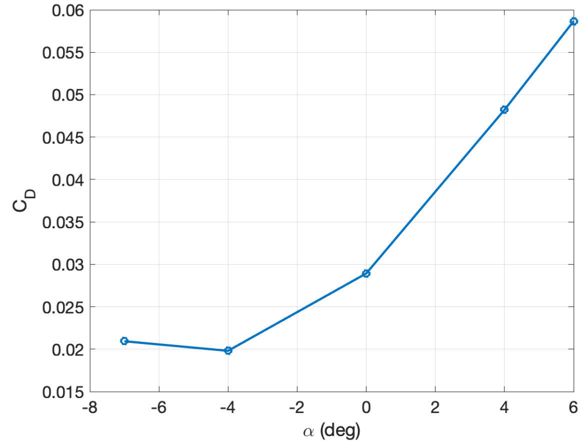

(b) Drag Curve

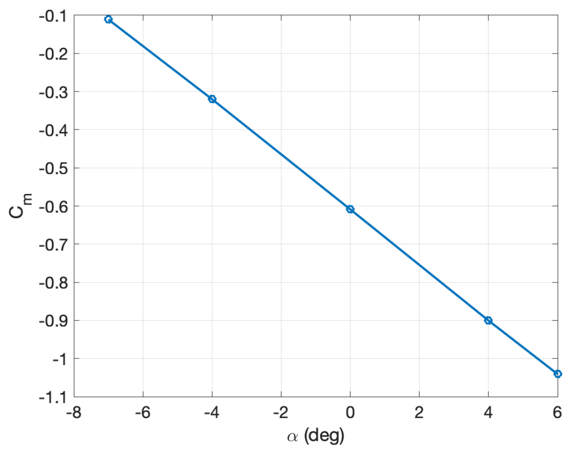

(c) Moment Curve

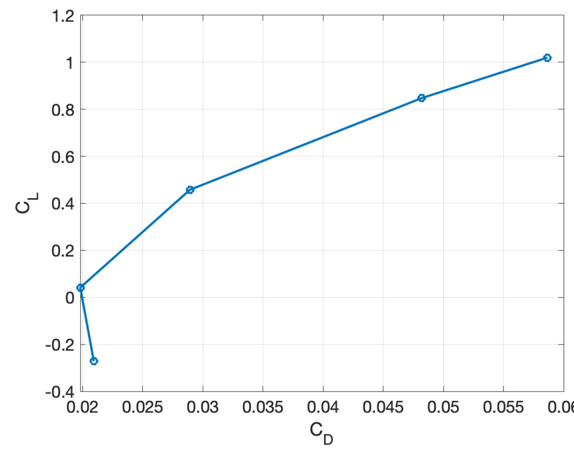

(d) Drag Polar

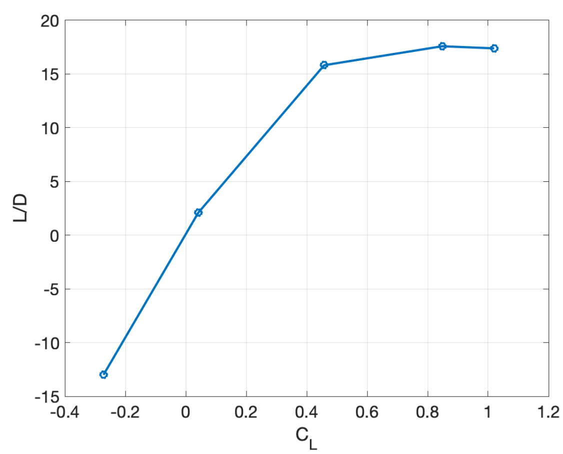

(e) Lift to Drag Ratio

Figure 26 CRM Aerodynamic Data at Mach 0.85 and $q_\infty = 230$ psf

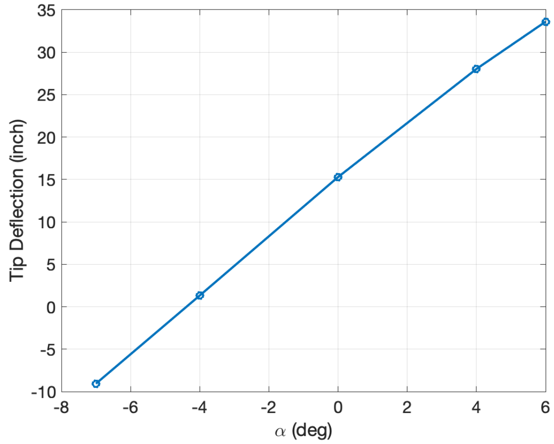

(a) Tip Deflection

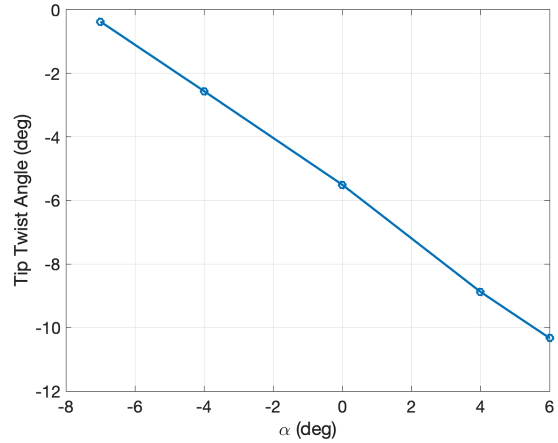

(b) Tip Twist Angle

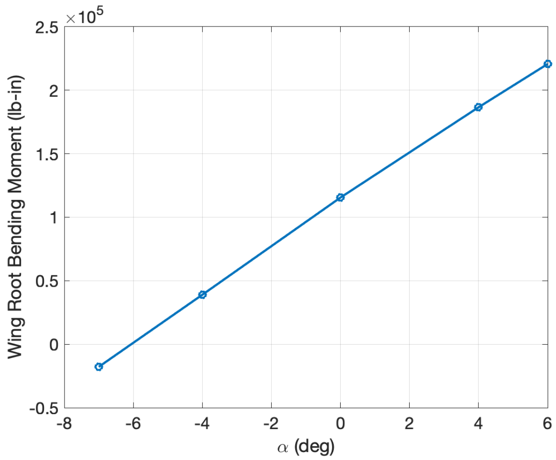

(c) Wing Root Bending Moment

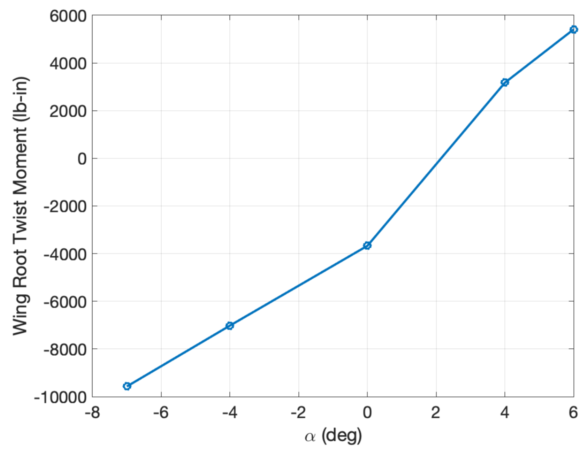

(d) Wing Root Twist Moment

Figure 27 CRM Structural Data at Mach 0.85 and q_∞ = 230 psf

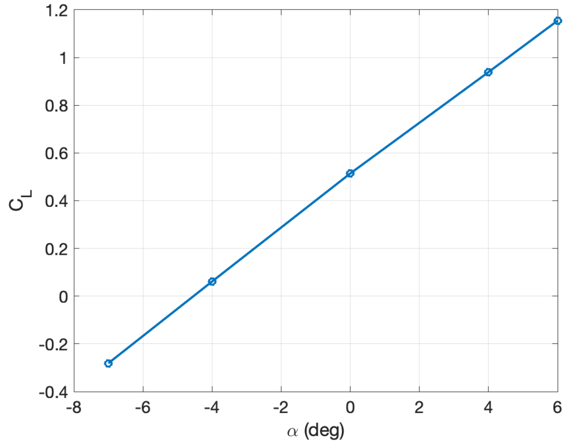

(a) Lift Curve

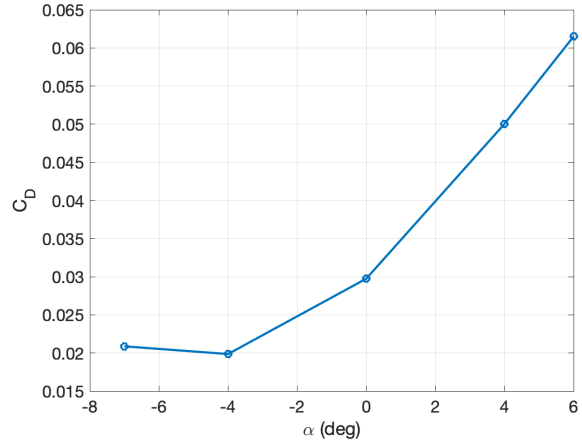

(b) Drag Curve

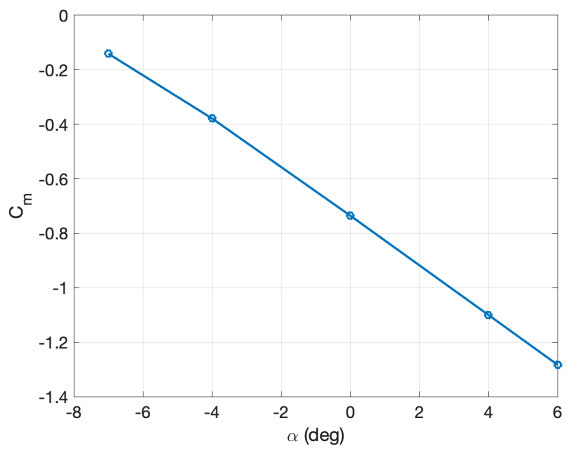

(c) Moment Curve

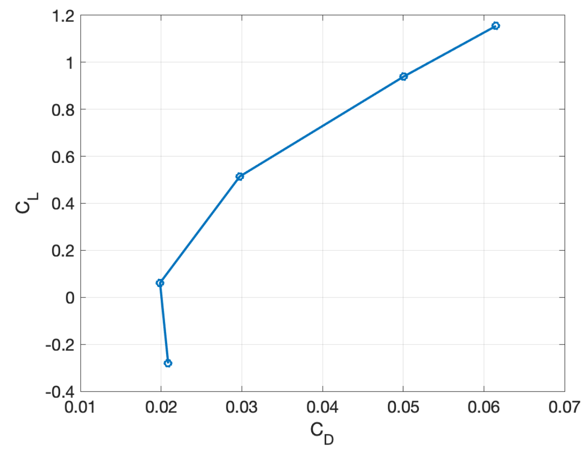

(d) Drag Polar

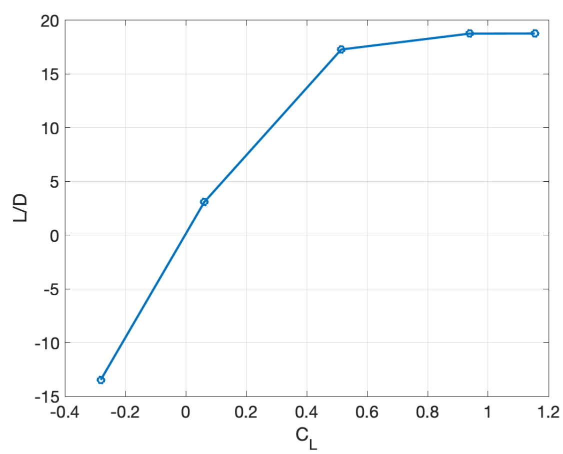

(e) Lift to Drag Ratio

Figure 28 CRM Aerodynamic Data at Mach 0.85 and q_∞ = 140 psf

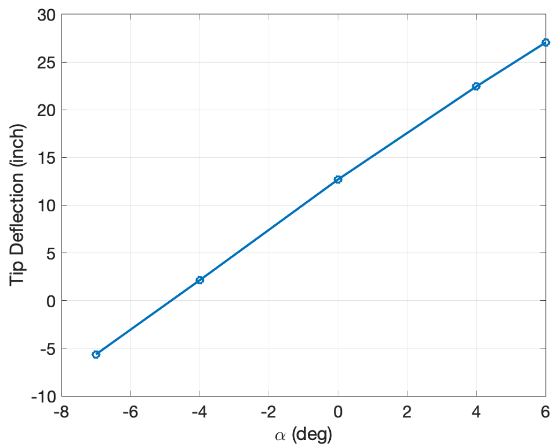

(a) Tip Deflection

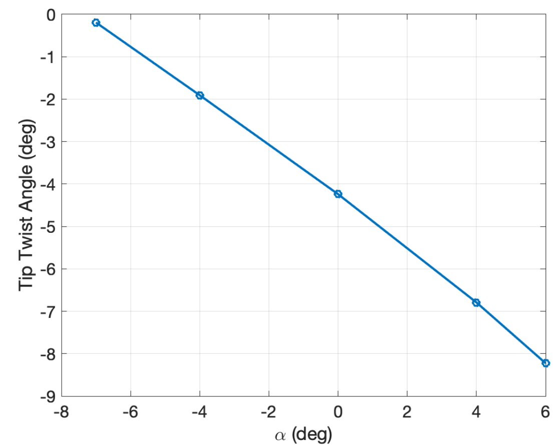

(b) Tip Twist Angle

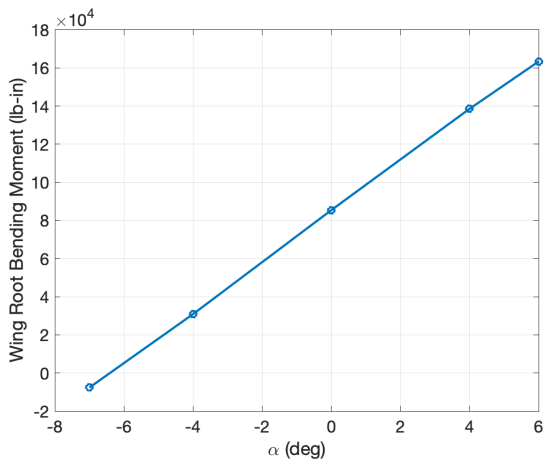

(c) Wing Root Bending Moment

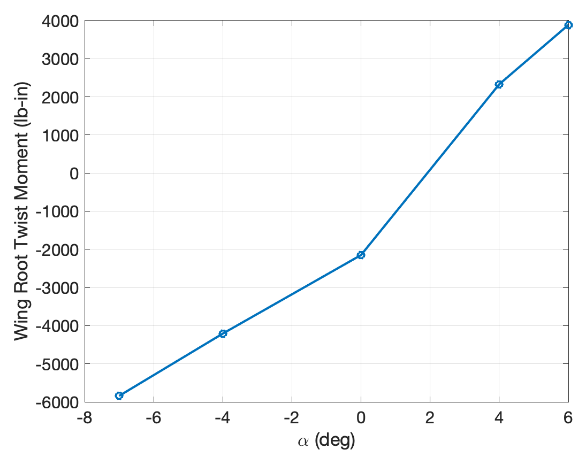

(d) Wing Root Twist Moment

Figure 29 CRM Structural Data at Mach 0.85 and q_∞ = 140 psf

Conclusions

In this paper, a VSPAERO aeroelastic simulation model of the wind-tunnel scale CRM model is developed. The structural deformation is calculated using a NASTRAN equivalent beam model. The VSPAERO model is coupled to the NASTRAN equivalent beam model to provide a rapid aero-structural analysis. A high-fidelity CFD model of the CRM is developed using FUN3D to validate the VSPAERO model. The data calculated by the VSPAERO model show a good agreement with the FUN3D simulation especially when the lift is less than 0.8. An aerodynamic database is generated using the developed VSPAERO aeroelastic model for the real-time drag optimization and maneuver load alleviation study of the wind-tunnel scale CRM model.

Acknowledgment

The authors wish to acknowledge NASA Advanced Air Transport Technology (AATT) project for the funding support of this work. The authors also wish to acknowledge Boeing Research and Technology, in particular Dr. John Quindlen, for providing the aerodynamic data to support this work under NASA contract NNL15AA00A with the AATT project.

References

[1] Nguyen, N., Livne, E., Precup, N., Urnes, J., Nelson, C., Ting, E. and Lebofsky, S., "Experimental Investigation of a Flexible Wing with a Variable Camber Continuous Trailing Edge Flap Design, " AIAA 2014-2441, June. 2014

[2] Nguyen, N., "Elastically Shaped Future Air Vehicle Concept, " NASA Innovation Fund Award 2010 Report, October 2010, Submitted to NASA Innovative Partnerships Program,

[3] Nguyen, N. and Urnes, J., "Aeroelastic Modeling of Elastically Shaped Aircraft Concept via Wing Shaping Control for Drag Reduction," AIAA Atmospheric Flight Mechanics Conference, AIAA-2012-4642, August 2012.

[4] Lebofsky, S., Ting, E., Trinh, K. V., Nguyen, N. T., "Optimization for Load Alleviation of Truss-Braced Wing Aircraft With Variable Camber Continuous Trailing Edge Flap," 33rd AIAA Applied Aerodynamics Confererence, AIAA-2015-2723, June 2015.

[5] Ting, E., Chaparro D., Nguyen, N. T., Fujiwara, G. E., "Optimization of Variable-Camber Continuous Trailing-Edge Flap Configuration for Drag Reduction," Journal of Aircraft, Vol. 55, No. 6, pp. 2217-2239, 2018.

[6] Bartels, R. E., Stanford B. K., Waite, J. M., "Performance Enhancement of the Flexible Transonic Truss-Braced Wing Aircraft Using Variable-Camber Continuous Trailing-Edge Flaps," AIAA 2019-0316, June 17-21, 2019, Dallas, Texas

[7] Vassberg, J., Dehaan M., Rivers, M., and Wahls, R., "Development of a Common Research Model for Applied CFD Validation Studies," 26th AIAA Applied Aerodynamics Conference, AIAA-2008-6919, August 2008.

[8] Fugate, J., Nguyen, N., and Xiong, J., "Aero-Structural Modeling of the Truss-BracedWing Aircraft Using Potential Method with Correction Methods for Transonic Viscous Flow andWing-Strut Interference Aerodynamics," AIAA Aviation Conference, AIAA-2019-3028, June 2019.

[9] Fujiwara, G., Chaparro, D., and Nguyen, N., "An Integral Boundary Layer Direct Method Applied to 2D Transonic Small-Disturbance Equations," 34th AIAA Applied Aerodynamics Conference, AIAA-2016-3160, June 2016.

[10] Chaparro, D., Fujiwara, G., Ting, E., and Nguyen, N., "Aerodynamic Modeling of Transonic Aircraft Using Vortex Lattice Coupled with Transonic Small Disturbance for Conceptual Design," 34th AIAA Applied Aerodynamics Conference, AIAA-2016-3012, June 2016.

[11] Chaparro, D., Fujiwara, G. E., Ting, E., and Nguyen, N. T., "Transonic and Viscous Potential Flow Method Applied to Flexible Wing Transport Aircraft," 35th AIAA Applied Aerodynamics Conference, AIAA-2017-4221, June 2017.

[12] Stahara, S. S., "Operational Manual for Two-Dimensional Transonic Code TSFOIL," NASA Contractor Report 3064, December, 1978.

[13] Drela, M., "A User's Guide to MSES 3.05," MIT Department of Aeronautics and Astronautics, July 2007.

[14] Korkegi, R. H. and Briggs, R. A., "Compressible Turbulent Plane Couette Flow," ARL 67-0223, Nov. 1967.

[15] Biedron, R. T., et al., "FUN3D Manual 13.2,", NASA TM-2017-219661, Aug. 2017

[16] Lee-Rausch, E. M., Hammond, D. P., Nielsen, E. J., Pirzadeh, S. Z., and Rumsey, C. L., "Application of the FUN3D Unstructured-Grid Navier-Stokes Solver to the 4th AIAA Drag Prediction Workshop cases," AIAA Aviation Conference, AIAA-2010-4511, January 2019.

[17] Roe, P. L., "Approximate Riemann Solvers, Parameter Vectors and Difference Schemes,", Journal of Computational Physics, Vol. 46, No. 2, 1980, pp. 357-378

[18] Venkatakrishnan, V., "Convergence to Steady State Solutions of the Euler Equations on Unstructured Grids with Limiters,", Journal of Computational Physics, Vol. 118, No. 1, 1995, pp. 120-130

[19] Spalart, P. R. and Allmaras, S. R., "A One-Equation Turbulence Model for Aerodynamic Flows," AIAA Science and Technology Forum and Exposition, AIAA-1992-0439, January 1992.

Appendix A

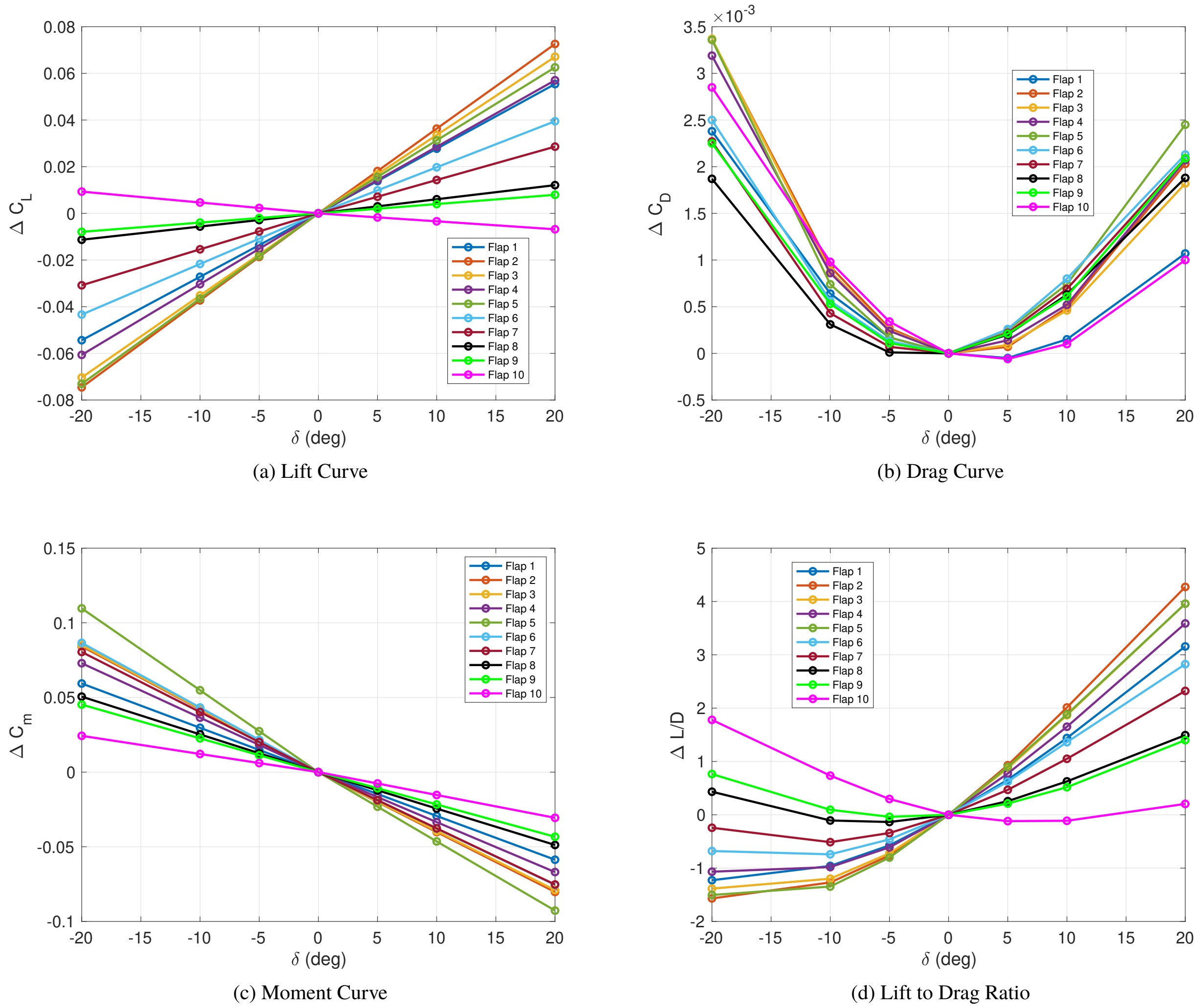

(a) Lift Curve

(b) Drag Curve

(c) Moment Curve

(d) Lift to Drag Ratio

Figure 30 Incremental Aerodynamic Data for CRM at Mach 0.70, $q_\infty = 230$ psf, and $\alpha = -7°$

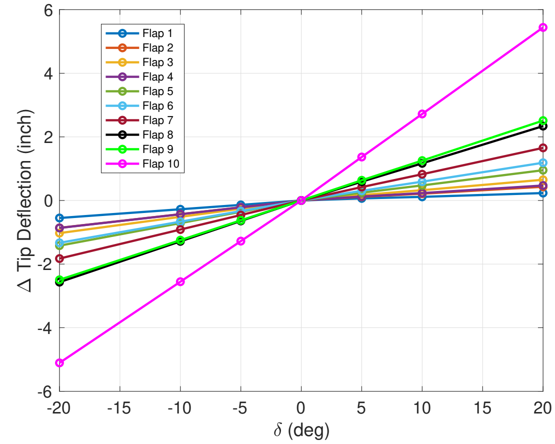

(a) Tip Deflection

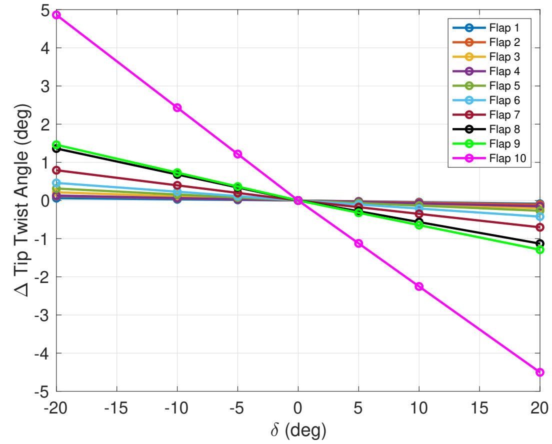

(b) Tip Twist Angle

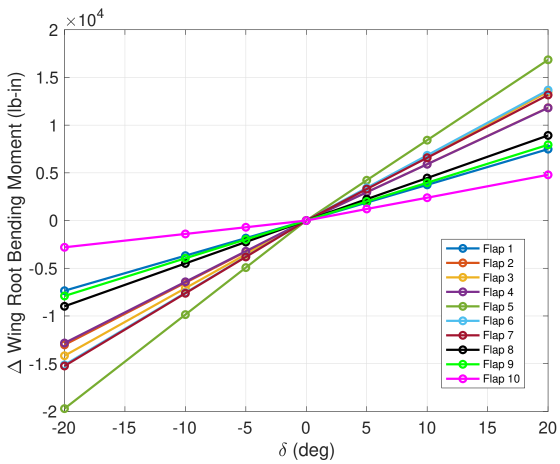

(c) Wing Root Bending Moment

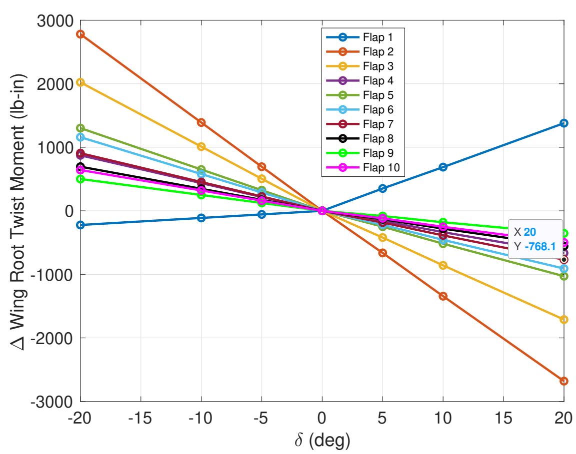

(d) Wing Root Twist Moment

Figure 31 Incremental Structural Data for CRM at Mach 0.70, $q_\infty = 230$ psf, and $\alpha = -7°$

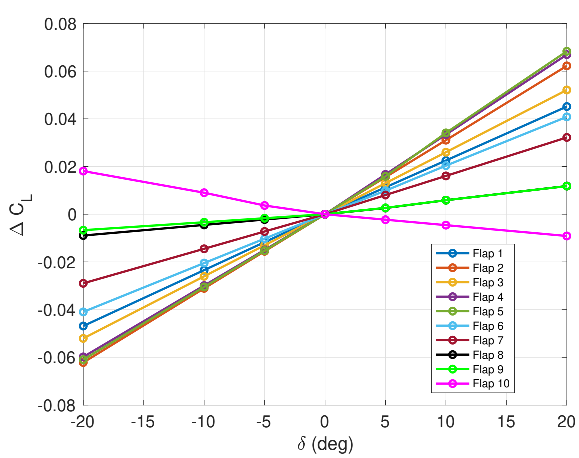

(a) Lift Curve

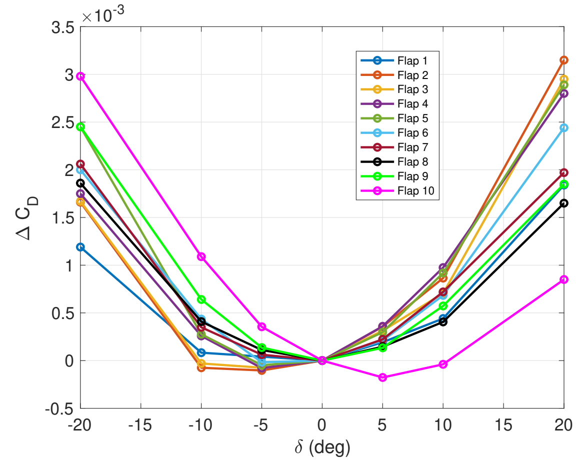

(b) Drag Curve

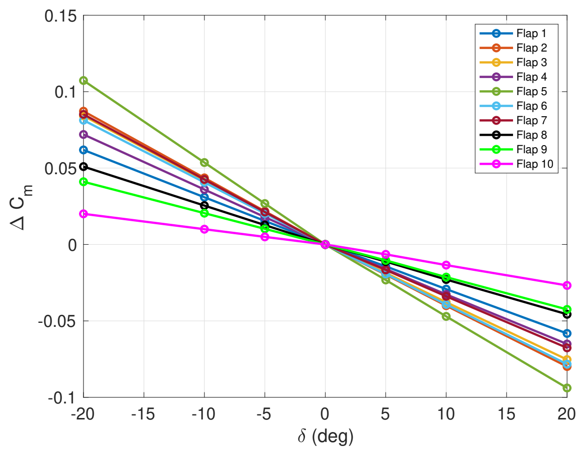

(c) Moment Curve

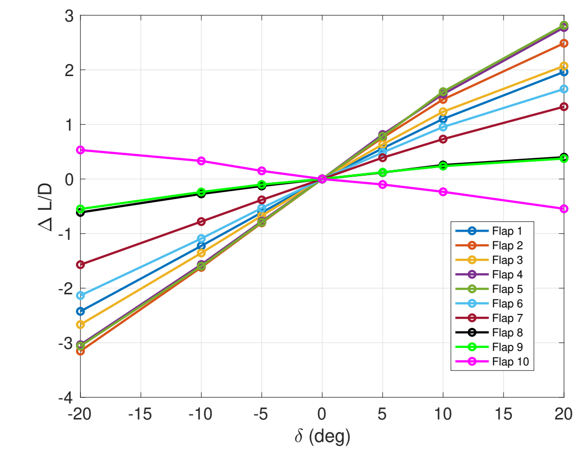

(d) Lift to Drag Ratio

Figure 32 Incremental Aerodynamic Data for CRM at Mach 0.70, $q_\infty = 230$ **psf, and** $\alpha = -4°$

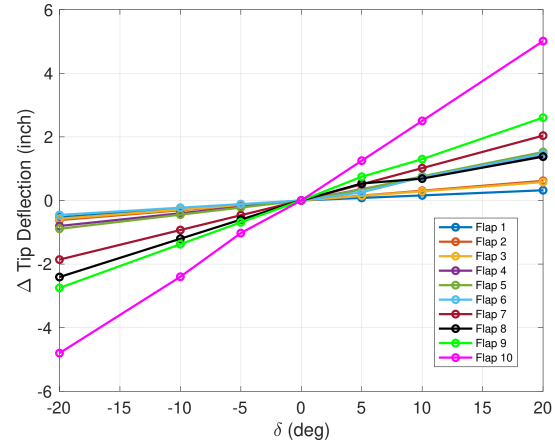

(a) Tip Deflection

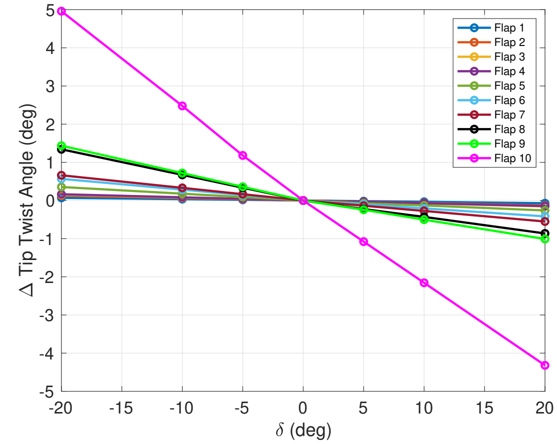

(b) Tip Twist Angle

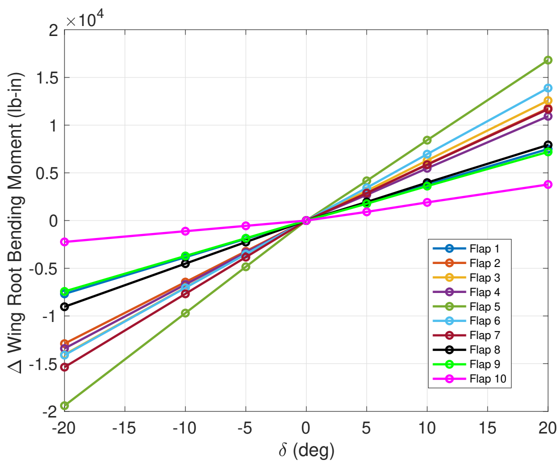

(c) Wing Root Bending Moment

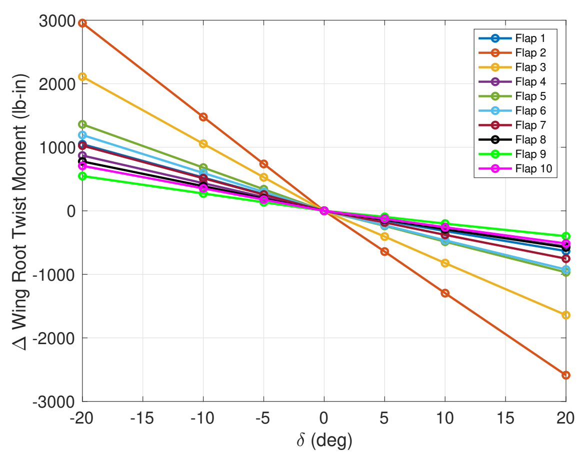

(d) Wing Root Twist Moment

Figure 33 Incremental Structural Data for CRM at Mach 0.70, $q_\infty = 230$ psf, and $\alpha = -4°$

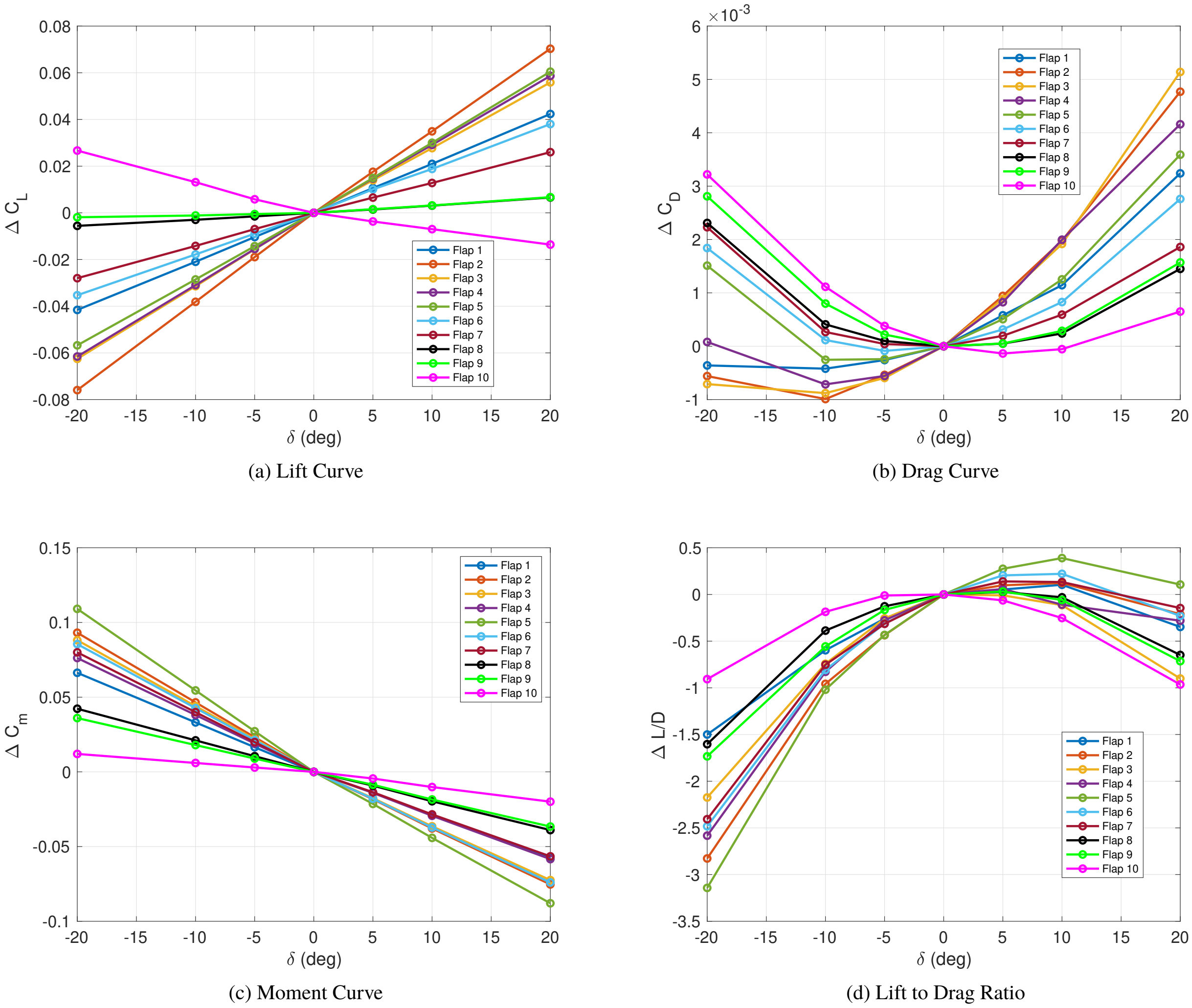

(a) Lift Curve

(b) Drag Curve

(c) Moment Curve

(d) Lift to Drag Ratio

Figure 34 Incremental Aerodynamic Data for CRM at Mach 0.70, q_∞ = 230 psf, and α = 0°

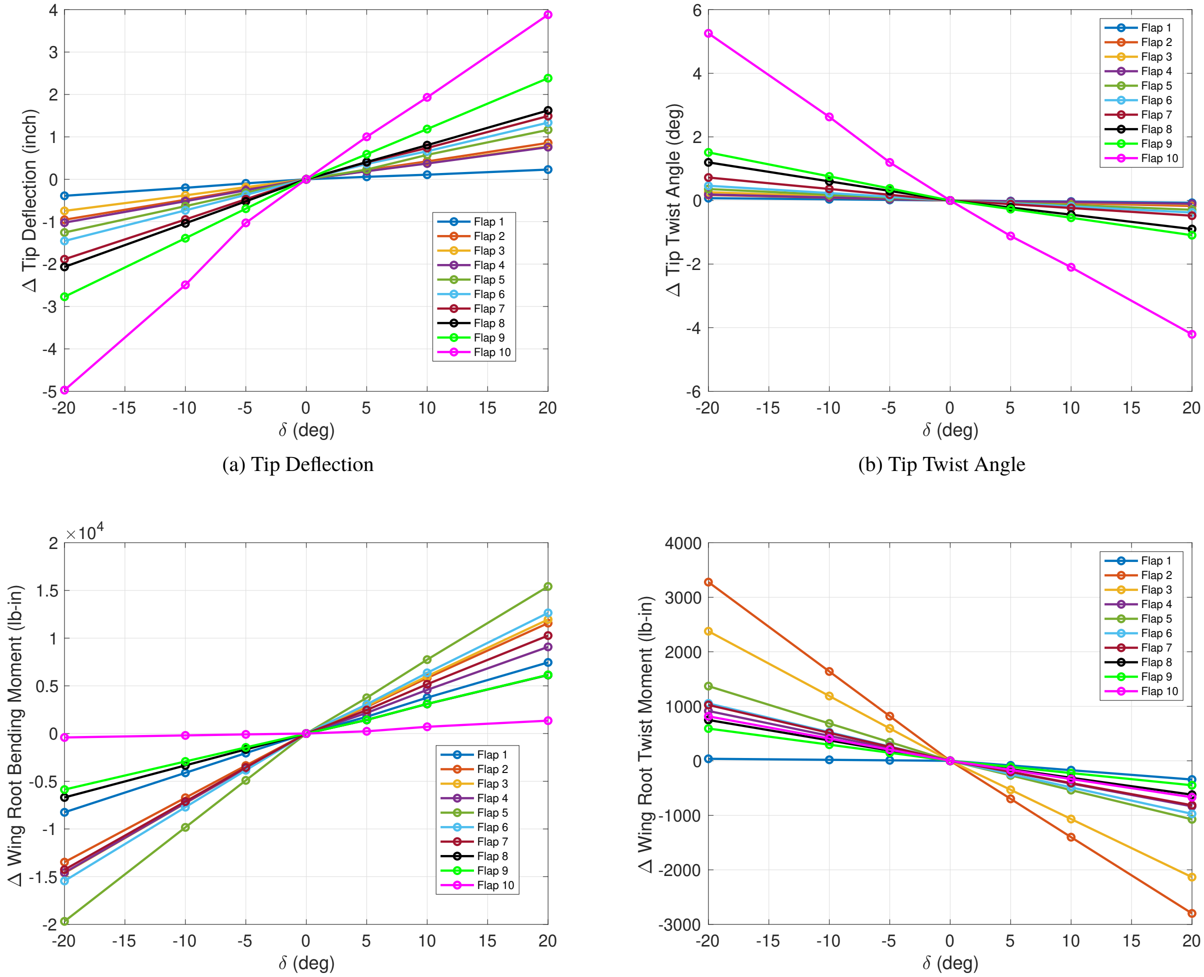

(a) Tip Deflection

(b) Tip Twist Angle

(c) Wing Root Bending Moment

(d) Wing Root Twist Moment

Figure 35 Incremental Structural Data for CRM at Mach 0.70, $q_\infty = 230$ psf, and $\alpha = 0°$

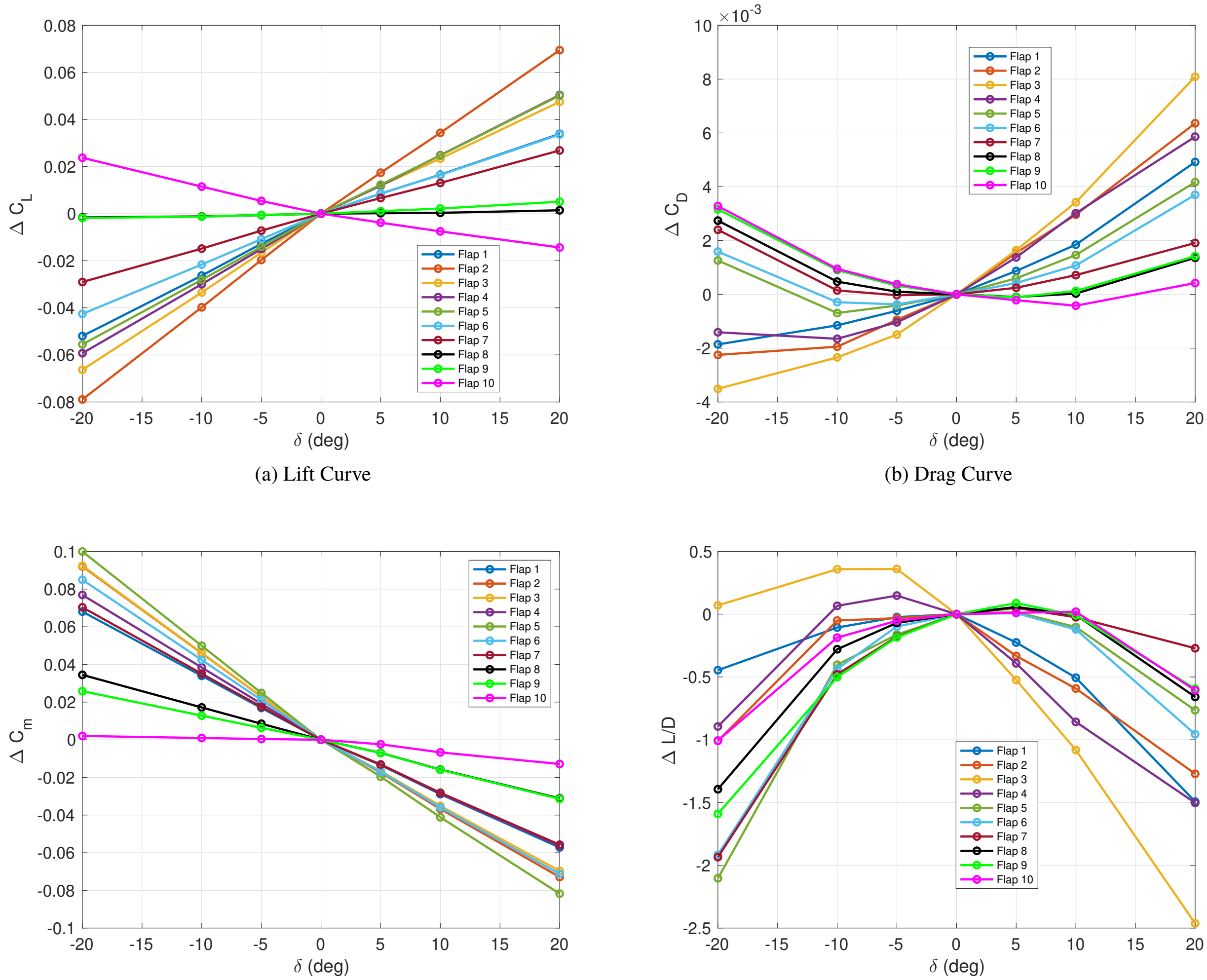

(a) Lift Curve

(b) Drag Curve

(c) Moment Curve

(d) Lift to Drag Ratio

Figure 36 Incremental Aerodynamic Data for CRM at Mach 0.70, $q_\infty = 230$ psf, and $\alpha = 4°$

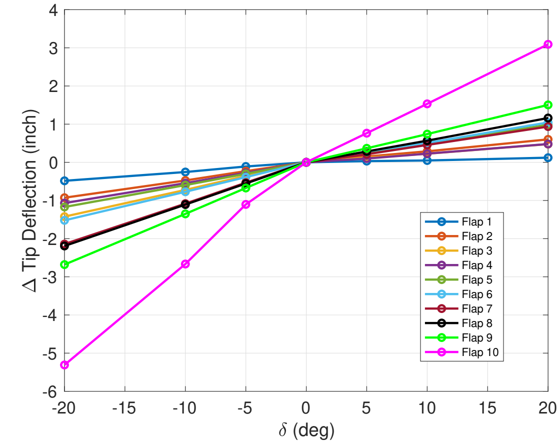

(a) Tip Deflection

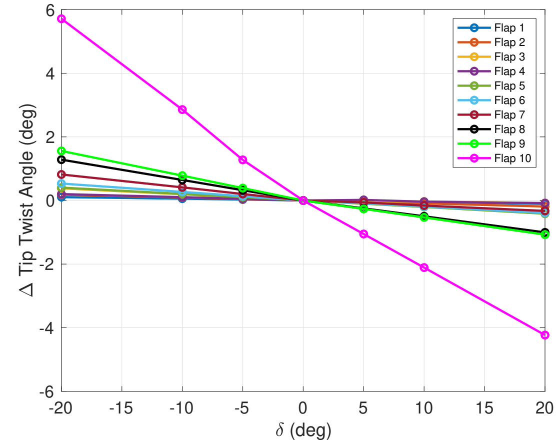

(b) Tip Twist Angle

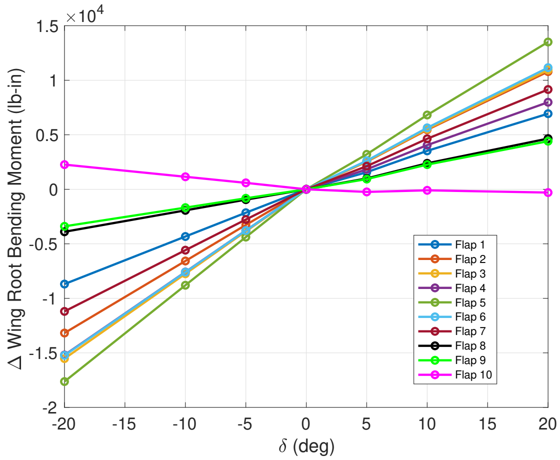

(c) Wing Root Bending Moment

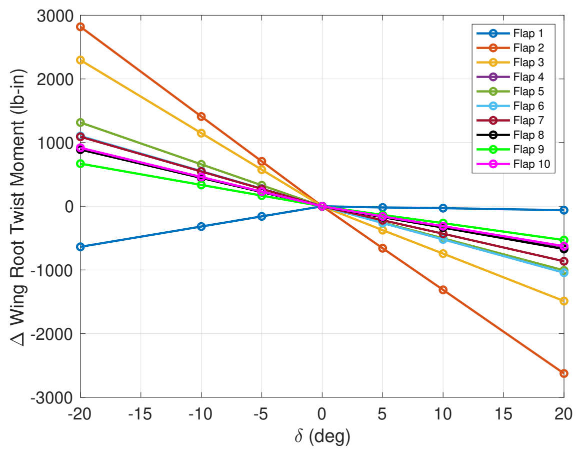

(d) Wing Root Twist Moment

Figure 37 Incremental Structural Data for CRM at Mach 0.70, $q_\infty = 230$ **psf, and** $\alpha = 4°$

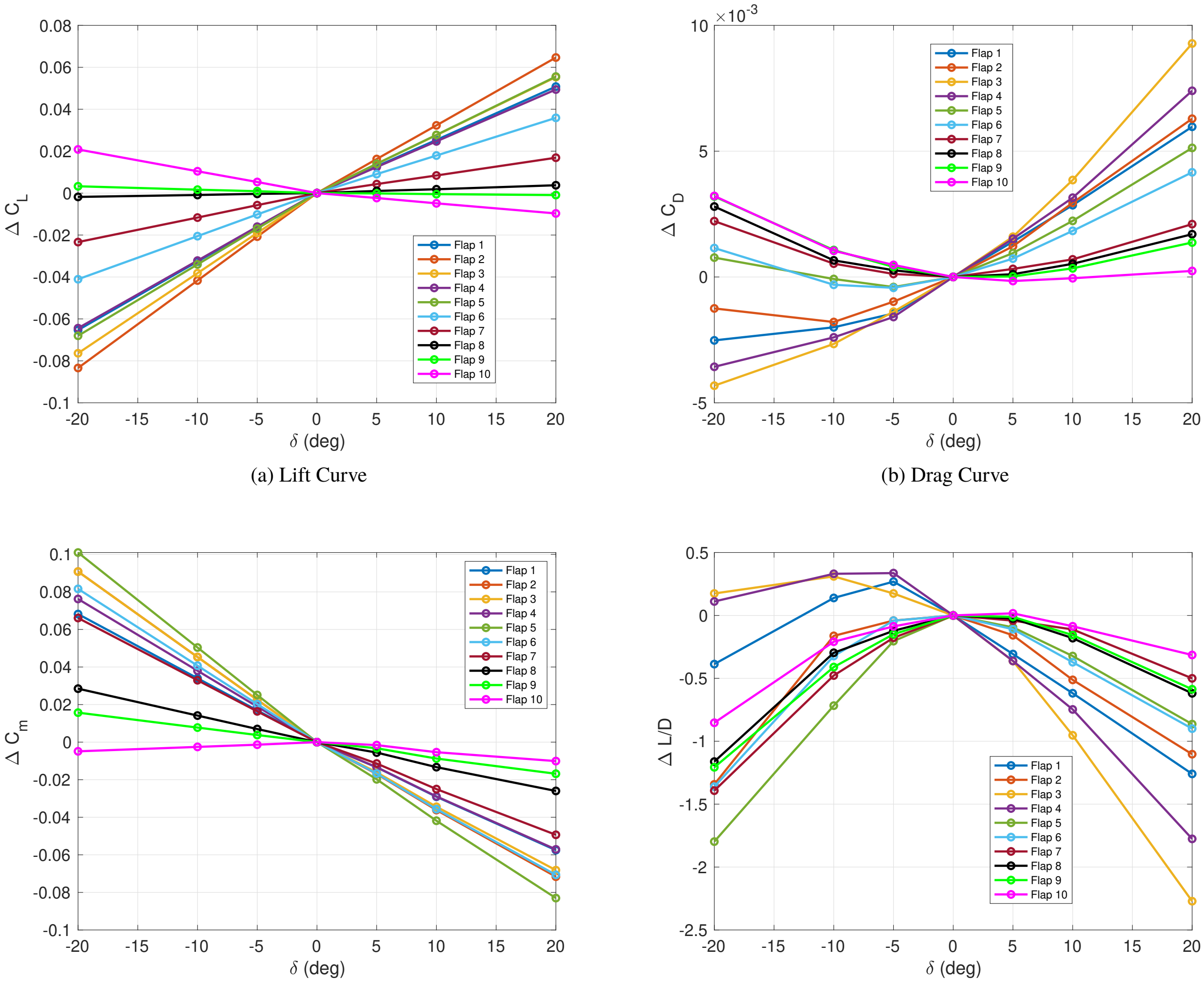

(a) Lift Curve

(b) Drag Curve

(c) Moment Curve

(d) Lift to Drag Ratio

Figure 38 Incremental Aerodynamic Data for CRM at Mach 0.70, $q_\infty = 230$ psf, and $\alpha = 6°$

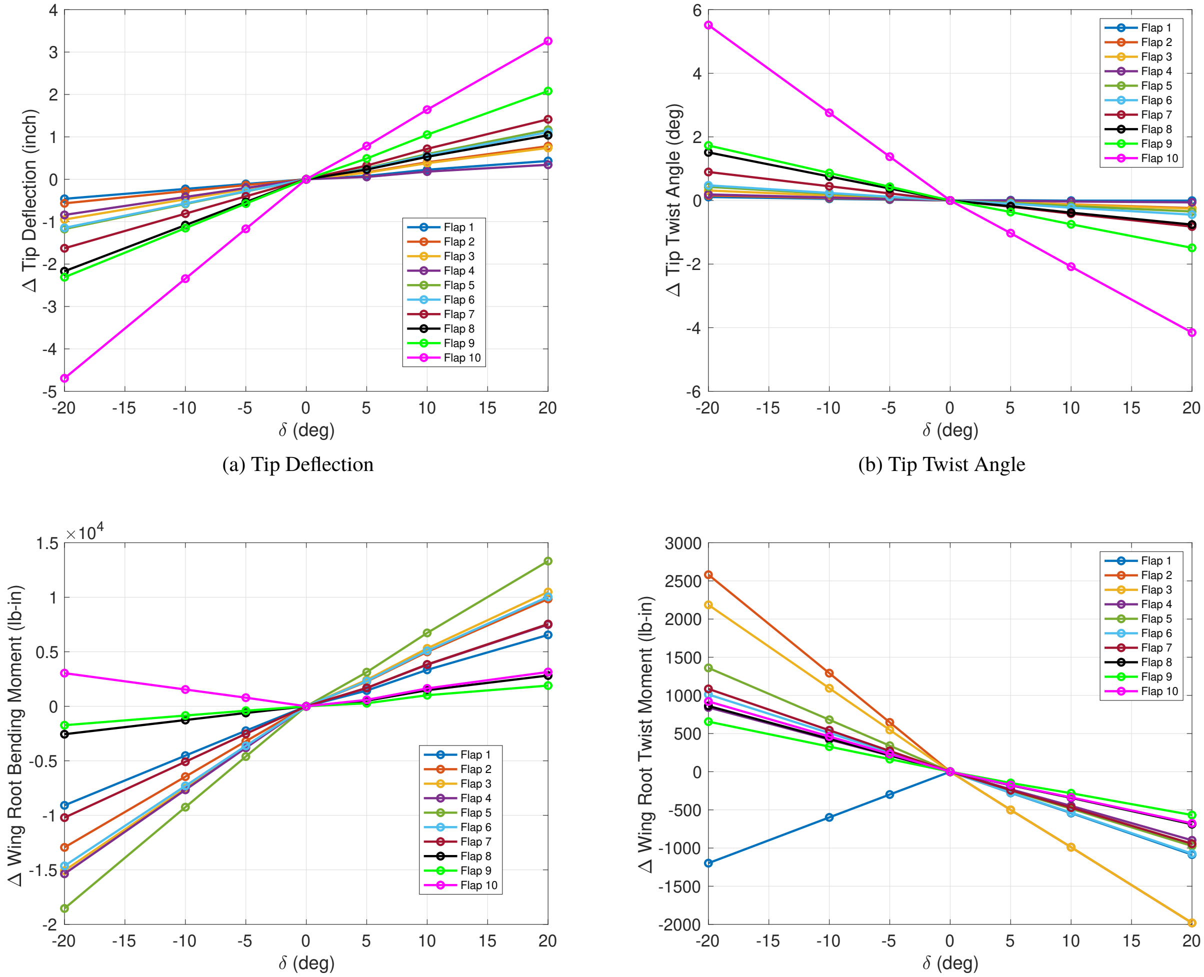

(a) Tip Deflection

(b) Tip Twist Angle

(c) Wing Root Bending Moment

(d) Wing Root Twist Moment

Figure 39 Incremental Structural Data for CRM at Mach 0.70, $q_\infty = 230$ psf, and $\alpha = 6°$

Appendix B

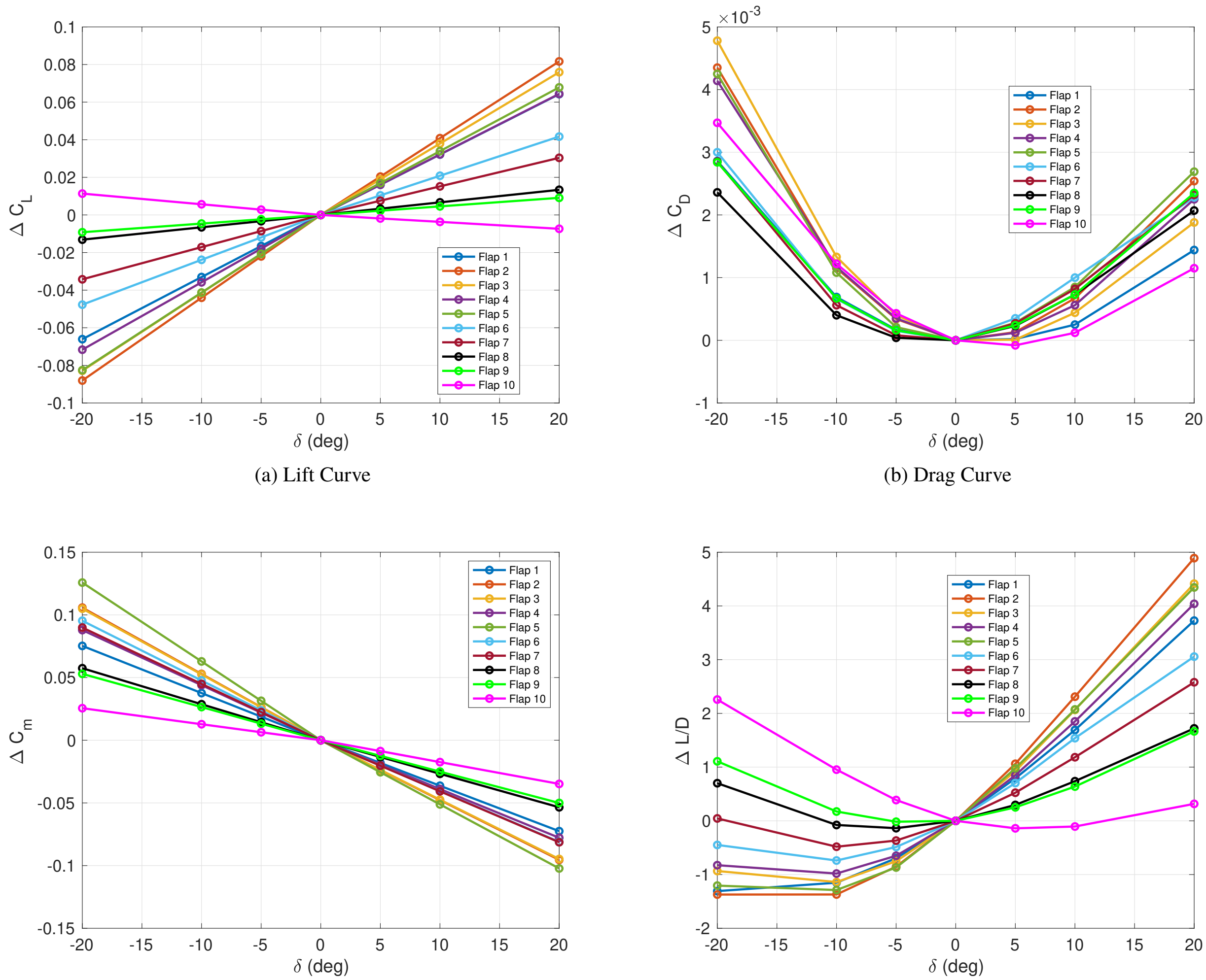

(a) Lift Curve

(b) Drag Curve

(c) Moment Curve

(d) Lift to Drag Ratio

Figure 40 Incremental Aerodynamic Data for CRM at Mach 0.80, $q_\infty = 200$ psf, and $\alpha = -7°$

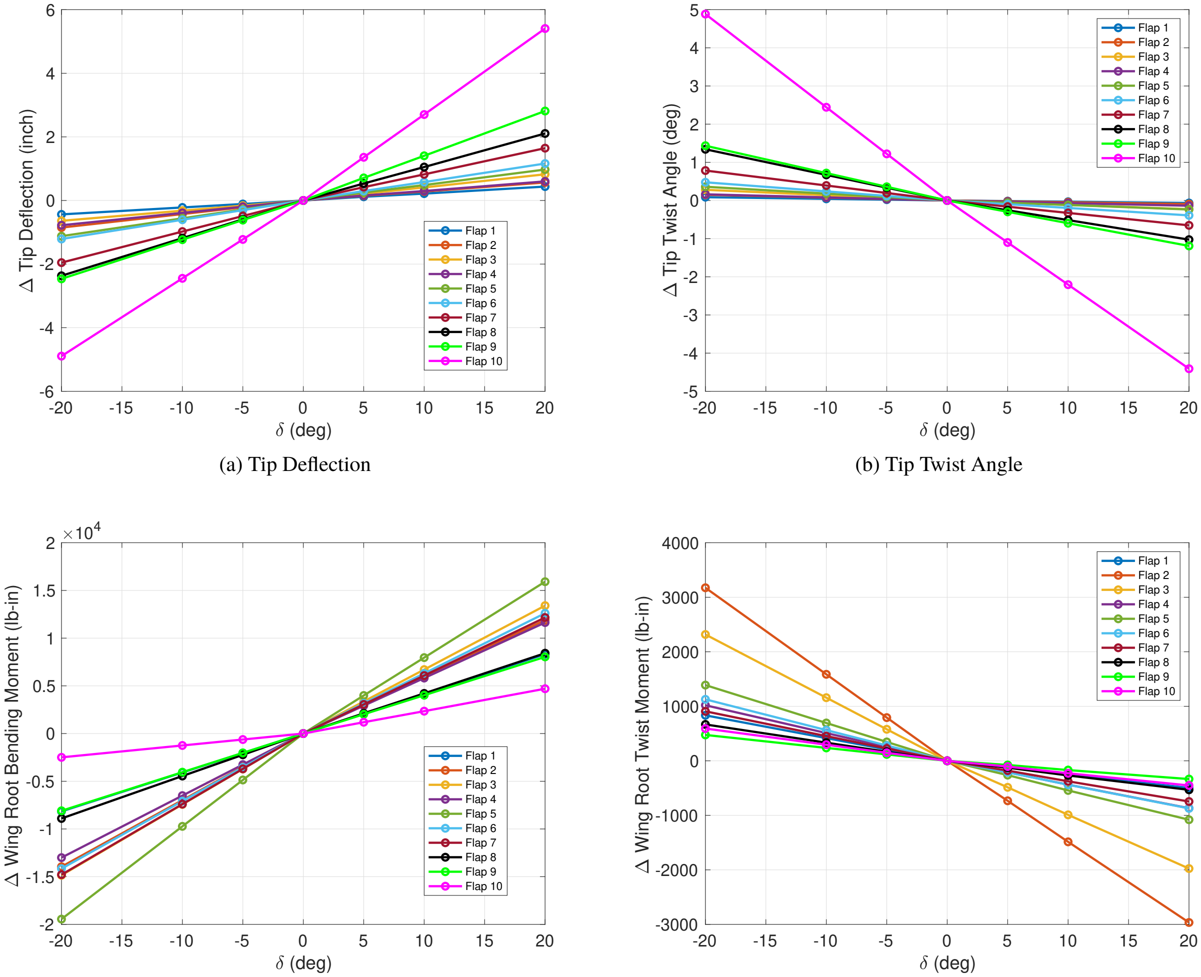

(a) Tip Deflection

(b) Tip Twist Angle

(c) Wing Root Bending Moment

(d) Wing Root Twist Moment

Figure 41 Incremental Structural Data for CRM at Mach 0.80, $q_\infty = 200$ psf, and $\alpha = -7°$

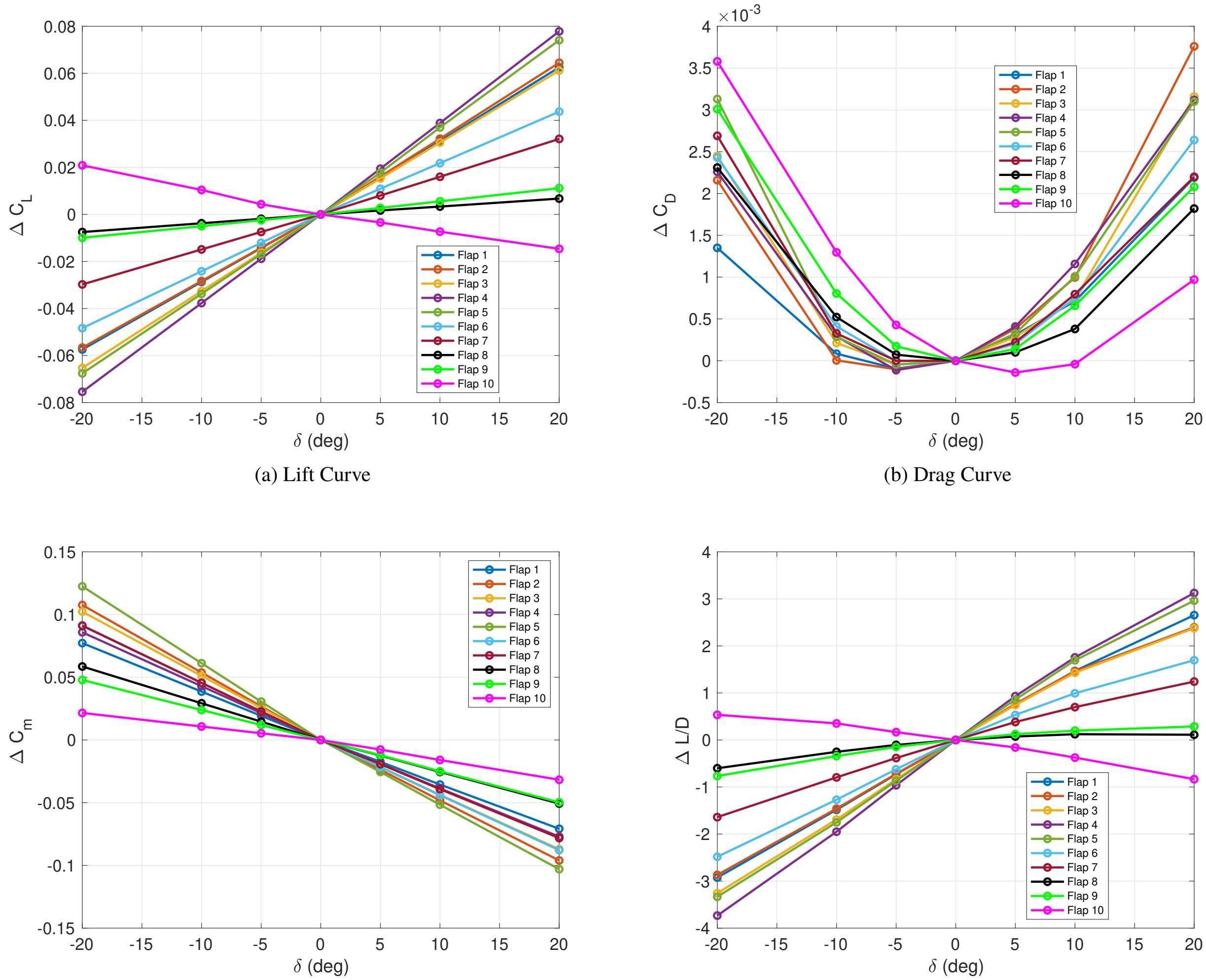

(a) Lift Curve

(b) Drag Curve

(c) Moment Curve

(d) Lift to Drag Ratio

Figure 42 Incremental Aerodynamic Data for CRM at Mach 0.80, $q_\infty = 200$ **psf, and** $\alpha = -4°$

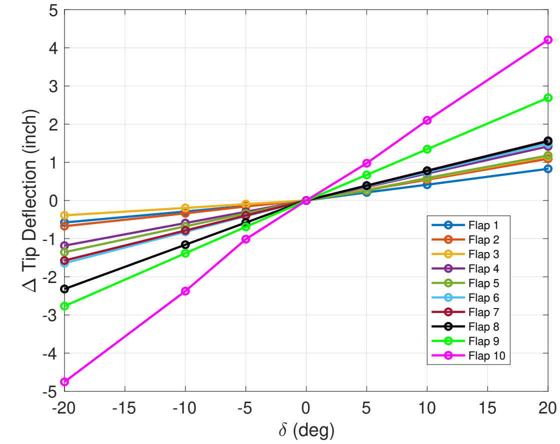

(a) Tip Deflection

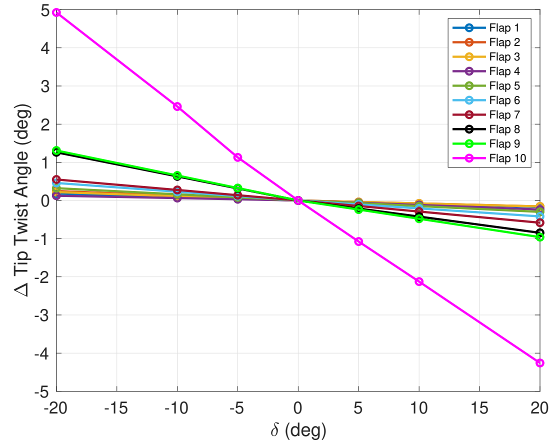

(b) Tip Twist Angle

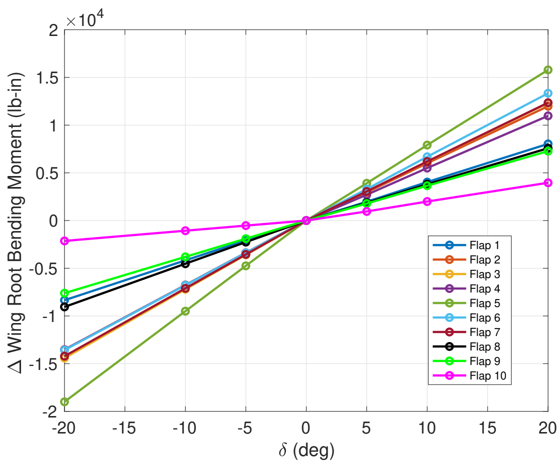

(c) Wing Root Bending Moment

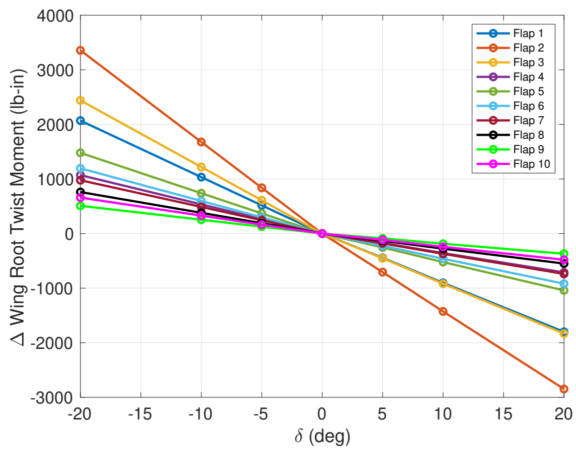

(d) Wing Root Twist Moment

Figure 43 Incremental Structural Data for CRM at Mach 0.80, $q_\infty = 200$ psf, and $\alpha = -4°$

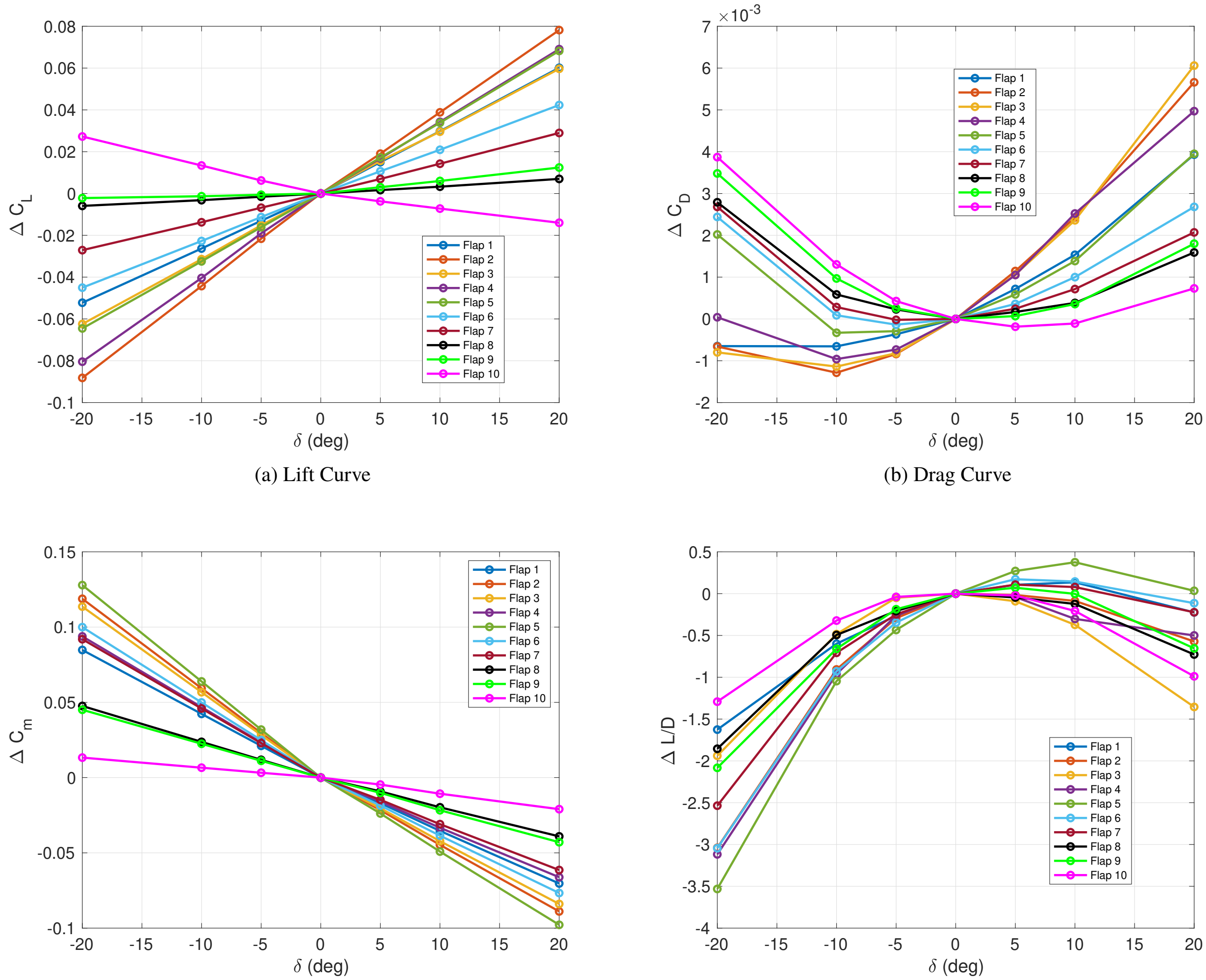

(a) Lift Curve (b) Drag Curve

(c) Moment Curve (d) Lift to Drag Ratio

Figure 44 Incremental Aerodynamic Data for CRM at Mach 0.80, $q_\infty = 200$ psf, and $\alpha = 0°$

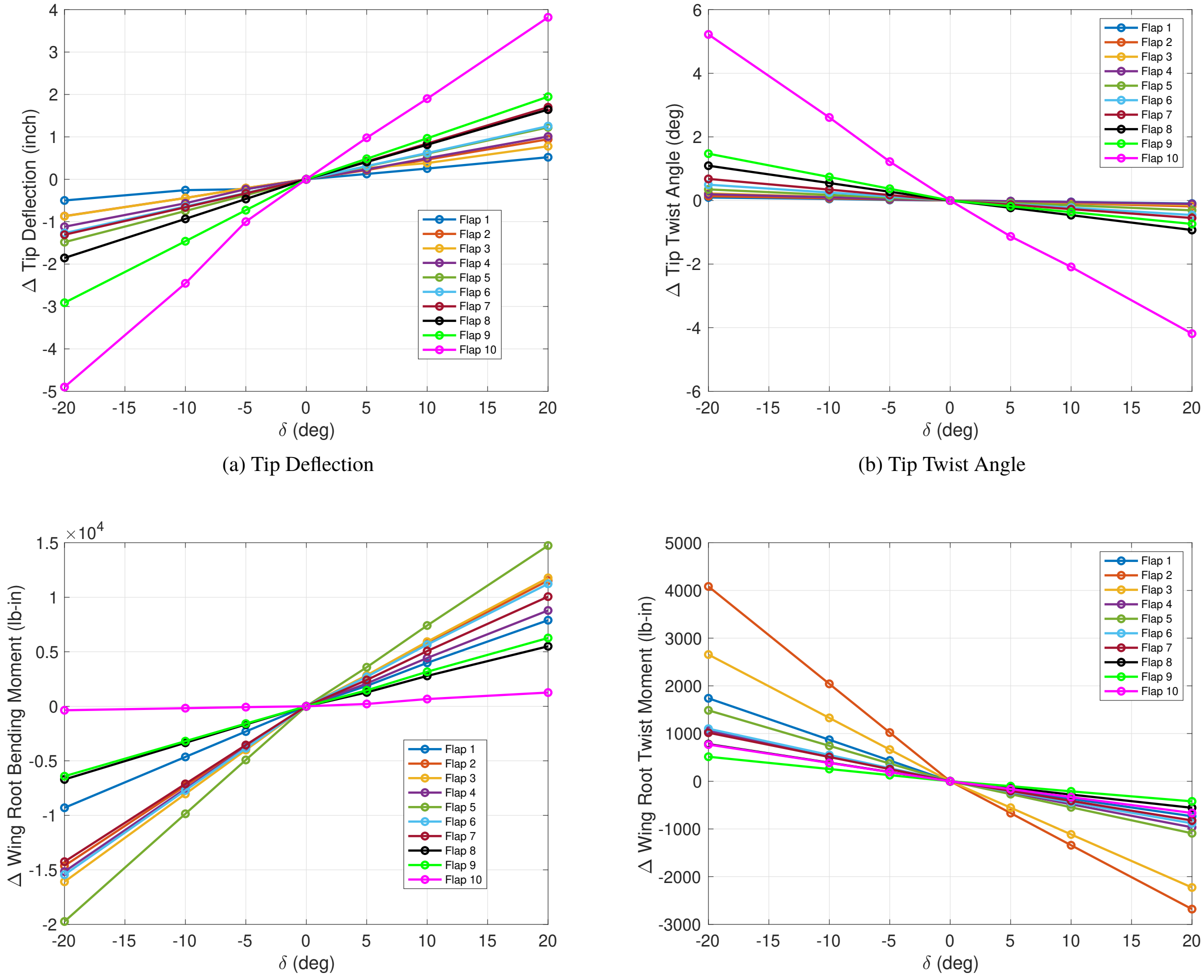

(a) Tip Deflection

(b) Tip Twist Angle

(c) Wing Root Bending Moment

(d) Wing Root Twist Moment

Figure 45 Incremental Structural Data for CRM at Mach 0.80, $q_\infty = 200$ psf, and $\alpha = 0°$

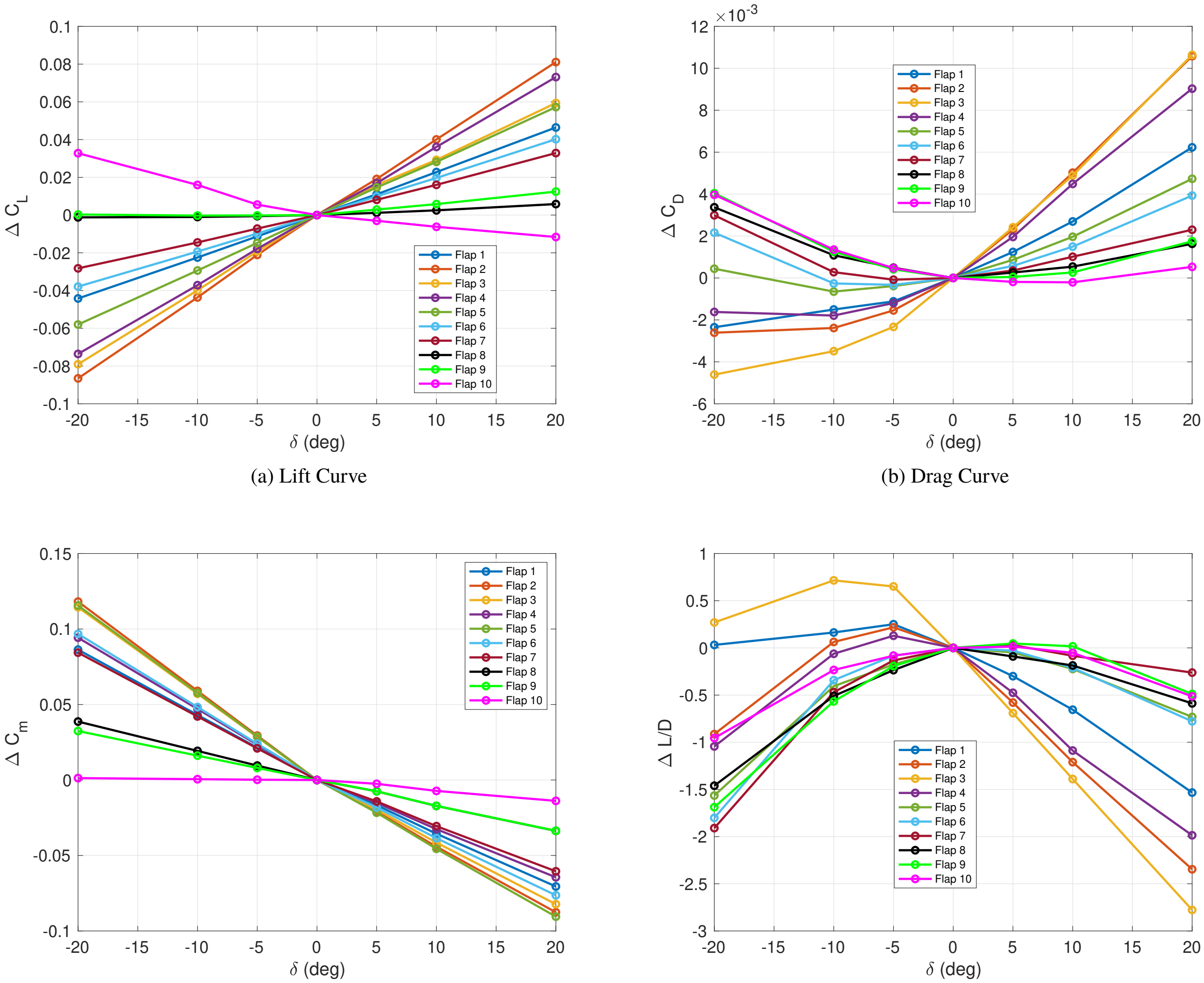

(a) Lift Curve

(b) Drag Curve

(c) Moment Curve

(d) Lift to Drag Ratio

Figure 46 Incremental Aerodynamic Data for CRM at Mach 0.80, $q_\infty = 200$ psf, and $\alpha = 4°$

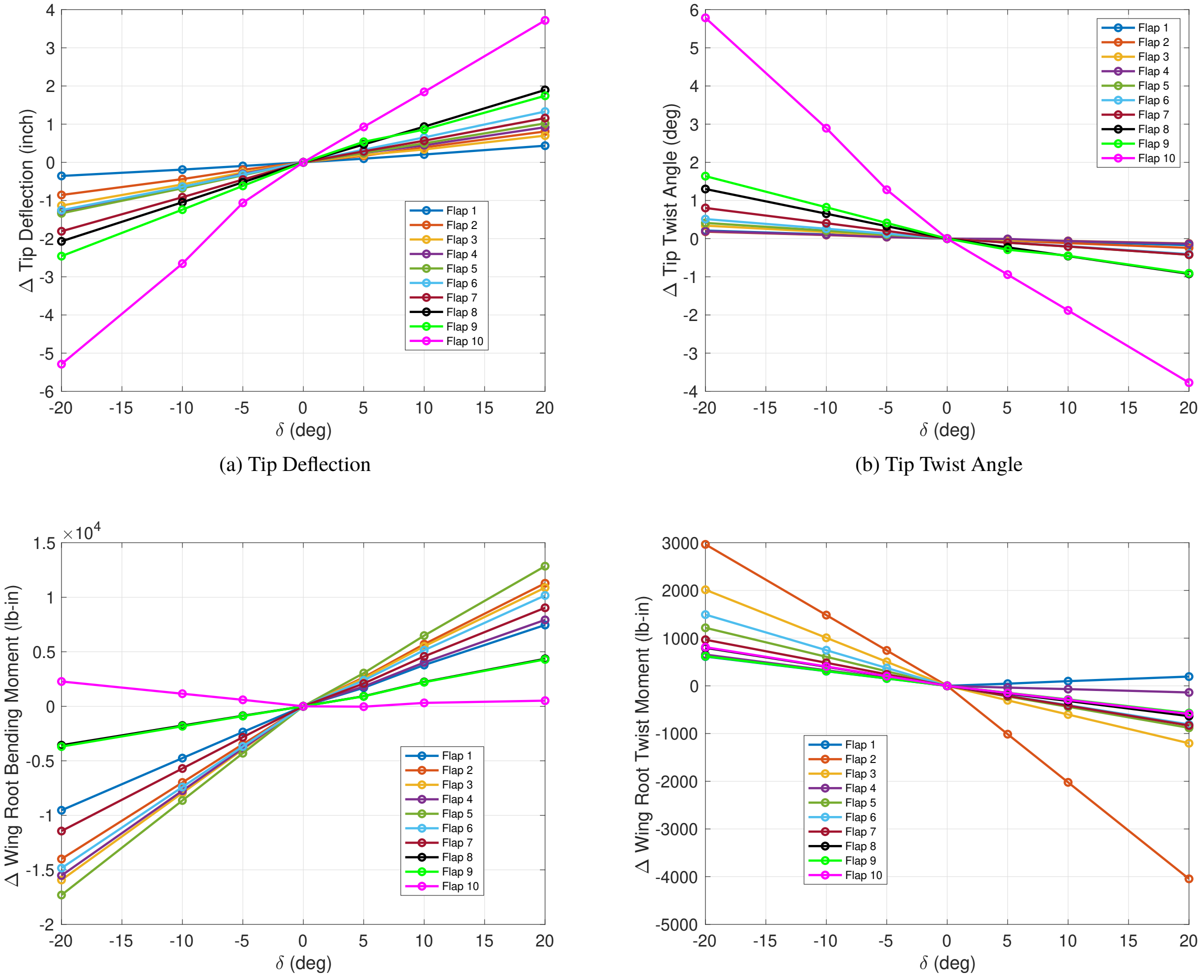

(a) Tip Deflection

(b) Tip Twist Angle

(c) Wing Root Bending Moment

(d) Wing Root Twist Moment

Figure 47 Incremental Structural Data for CRM at Mach 0.80, $q_\infty = 200$ psf, and $\alpha = 4°$

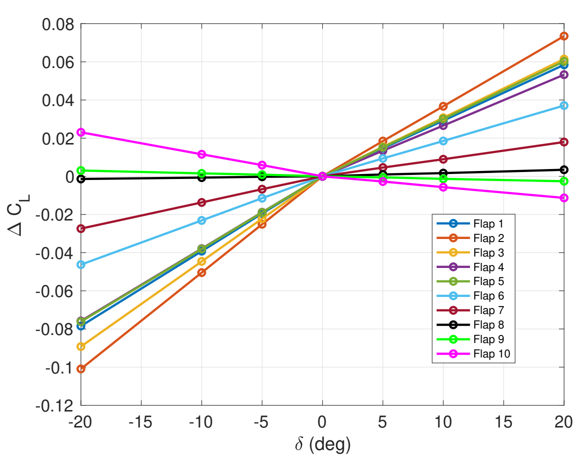

(a) Lift Curve

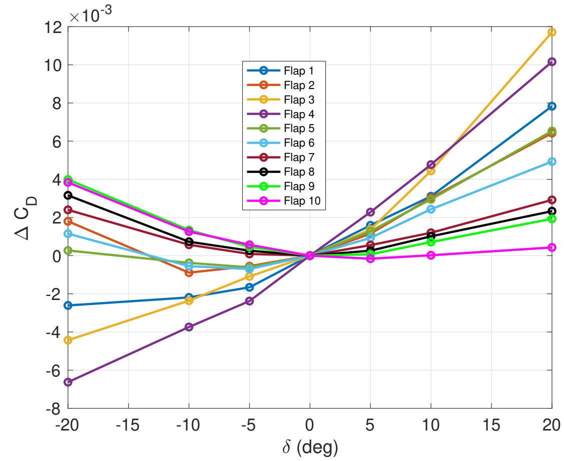

(b) Drag Curve

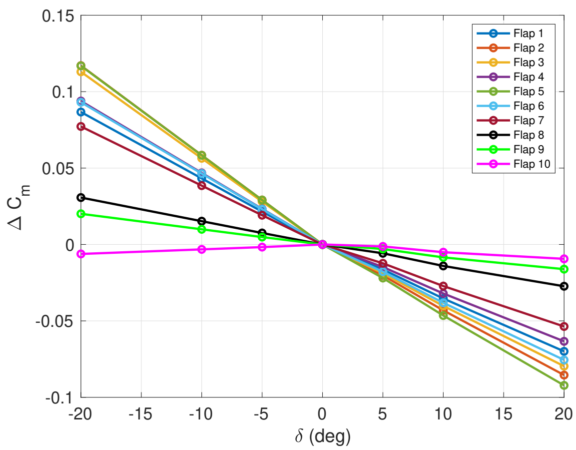

(c) Moment Curve

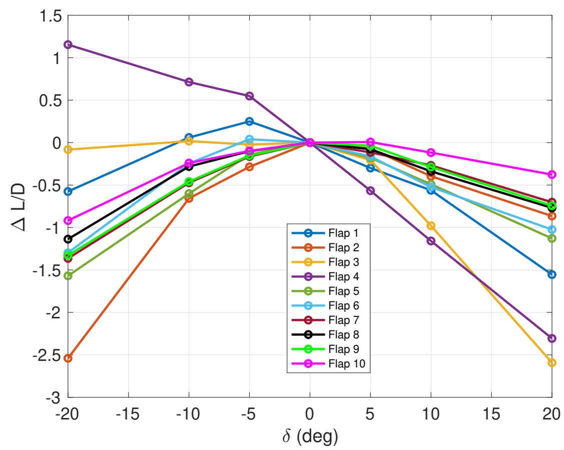

(d) Lift to Drag Ratio

Figure 48 Incremental Aerodynamic Data for CRM at Mach 0.80, $q_\infty = 200$ psf, and $\alpha = 6°$

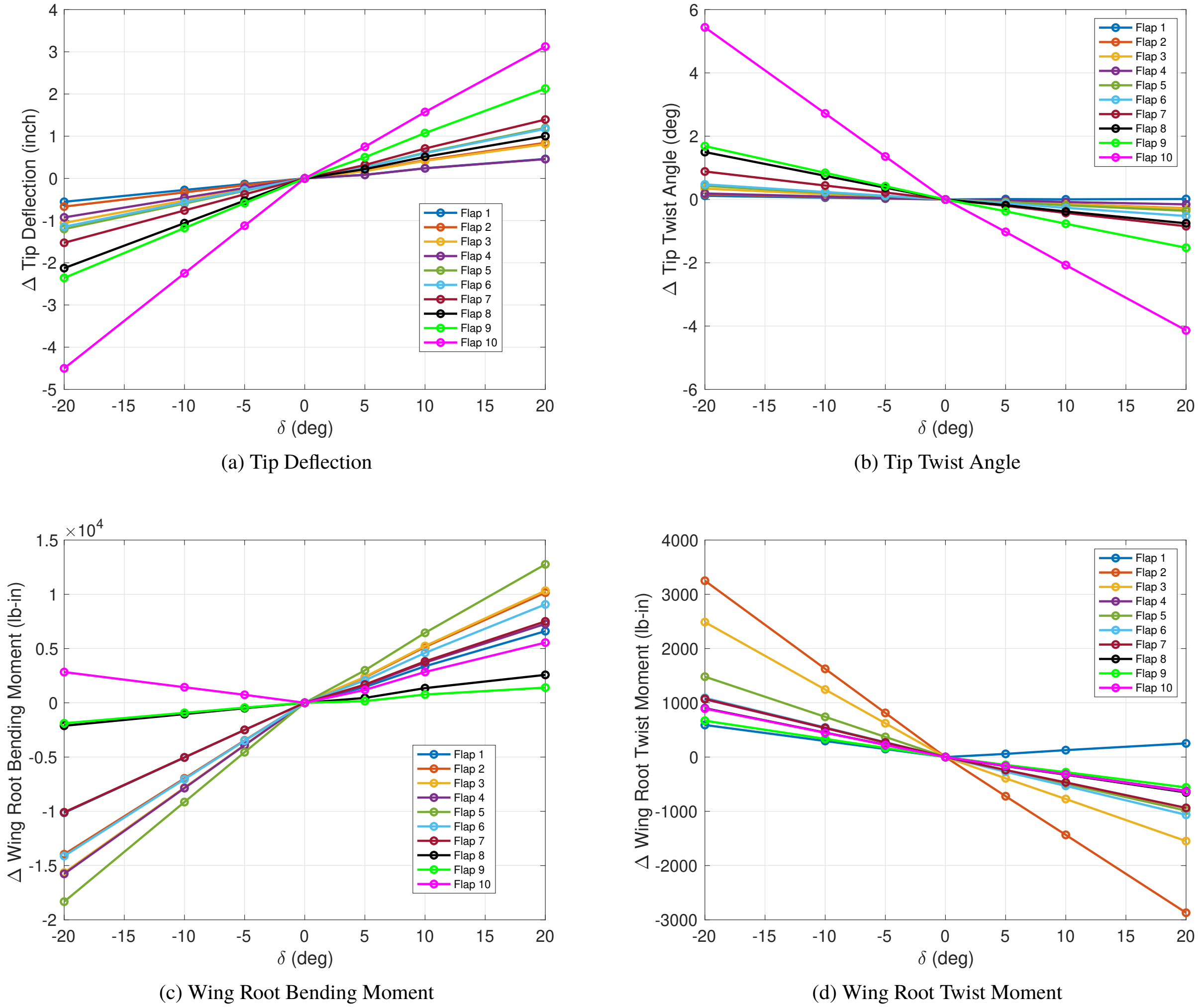

(a) Tip Deflection

(b) Tip Twist Angle

(c) Wing Root Bending Moment

(d) Wing Root Twist Moment

Figure 49 Incremental Structural Data for CRM at Mach 0.80, $q_\infty = 200$ psf, and $\alpha = 6°$

Appendix C

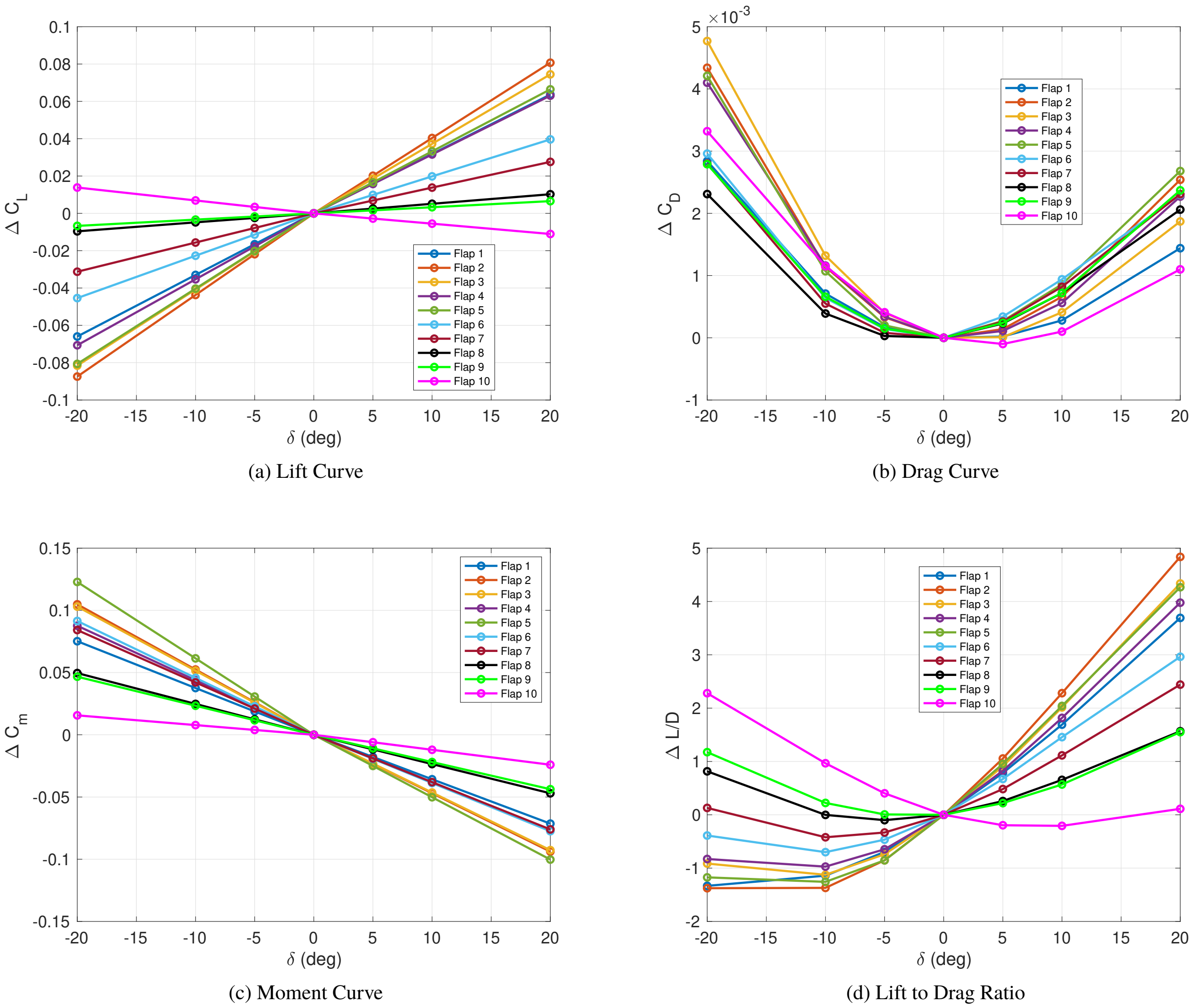

(a) Lift Curve

(b) Drag Curve

(c) Moment Curve

(d) Lift to Drag Ratio

Figure 50 Incremental Aerodynamic Data for CRM at Mach 0.80, $q_\infty = 230$ psf, and $\alpha = -7°$

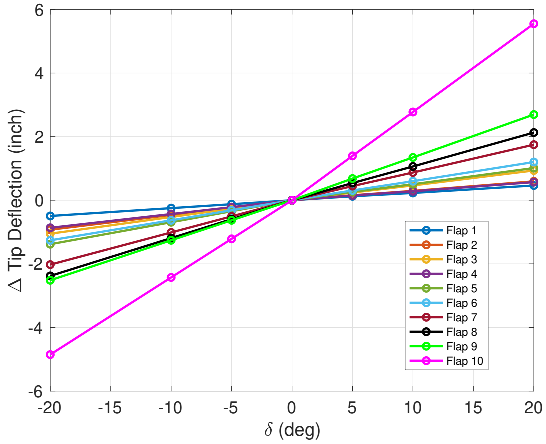

(a) Tip Deflection

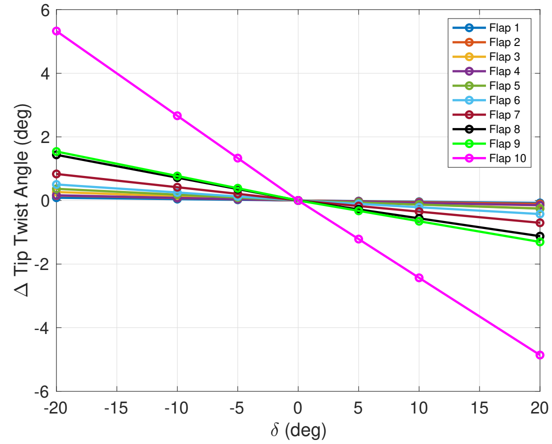

(b) Tip Twist Angle

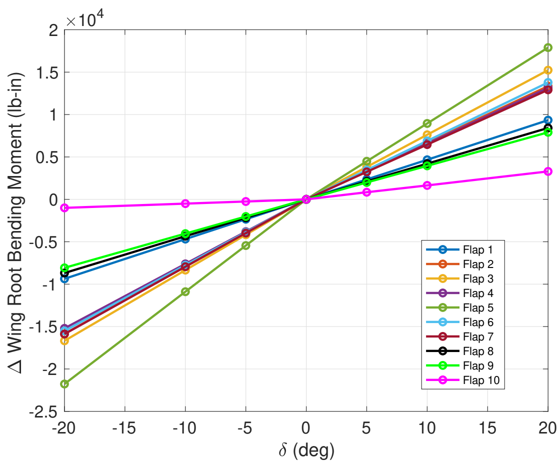

(c) Wing Root Bending Moment

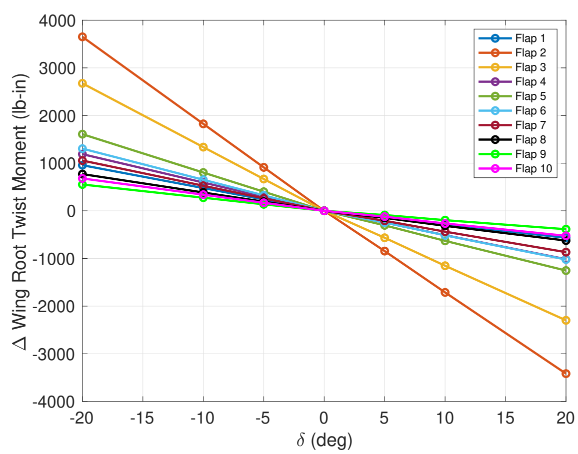

(d) Wing Root Twist Moment

Figure 51 Incremental Structural Data for CRM at Mach 0.80, $q_\infty = 230$ psf, and $\alpha = -7°$

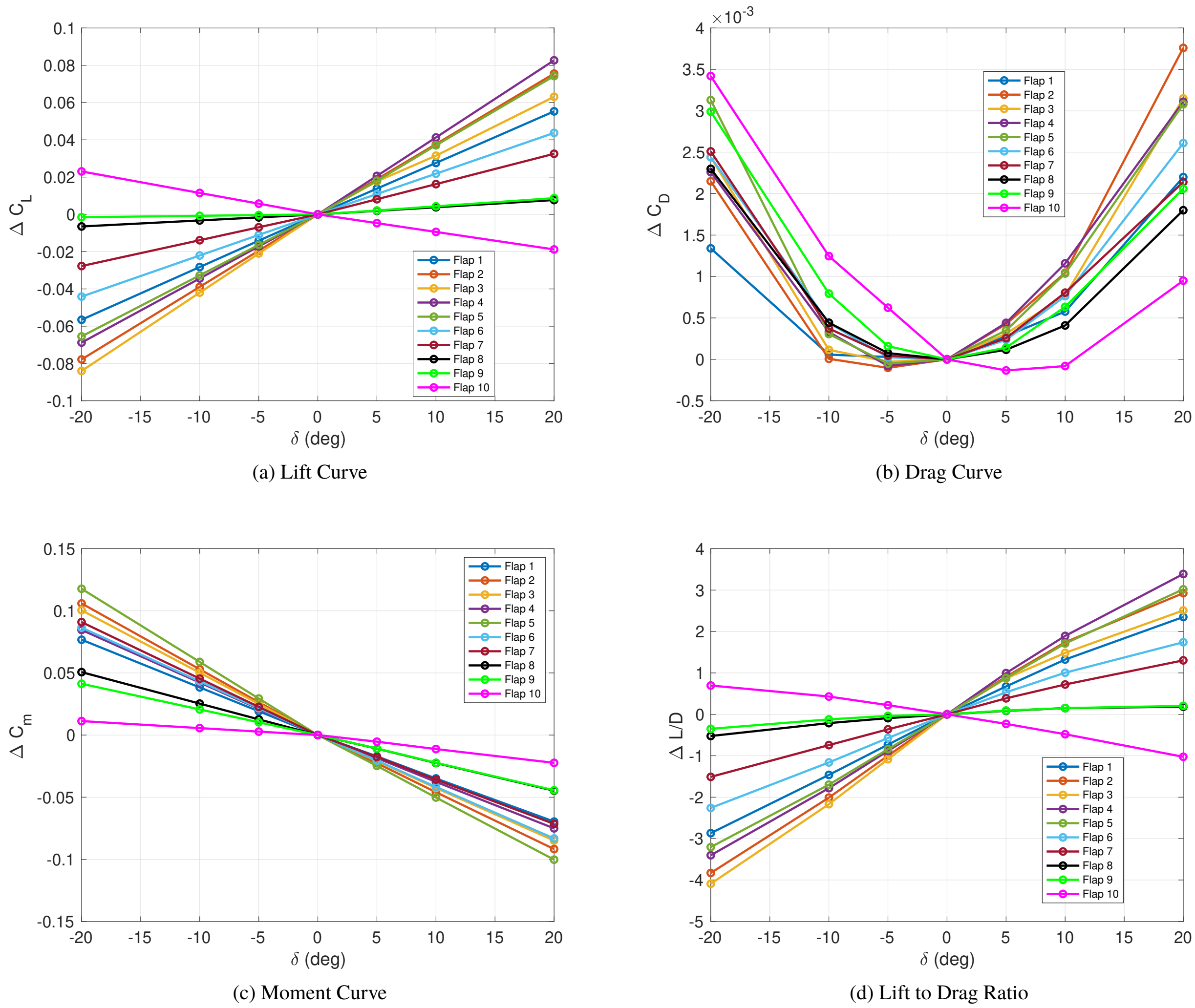

(a) Lift Curve

(b) Drag Curve

(c) Moment Curve

(d) Lift to Drag Ratio

Figure 52 Incremental Aerodynamic Data for CRM at Mach 0.80, q_∞ = 230 psf, and α = −4°

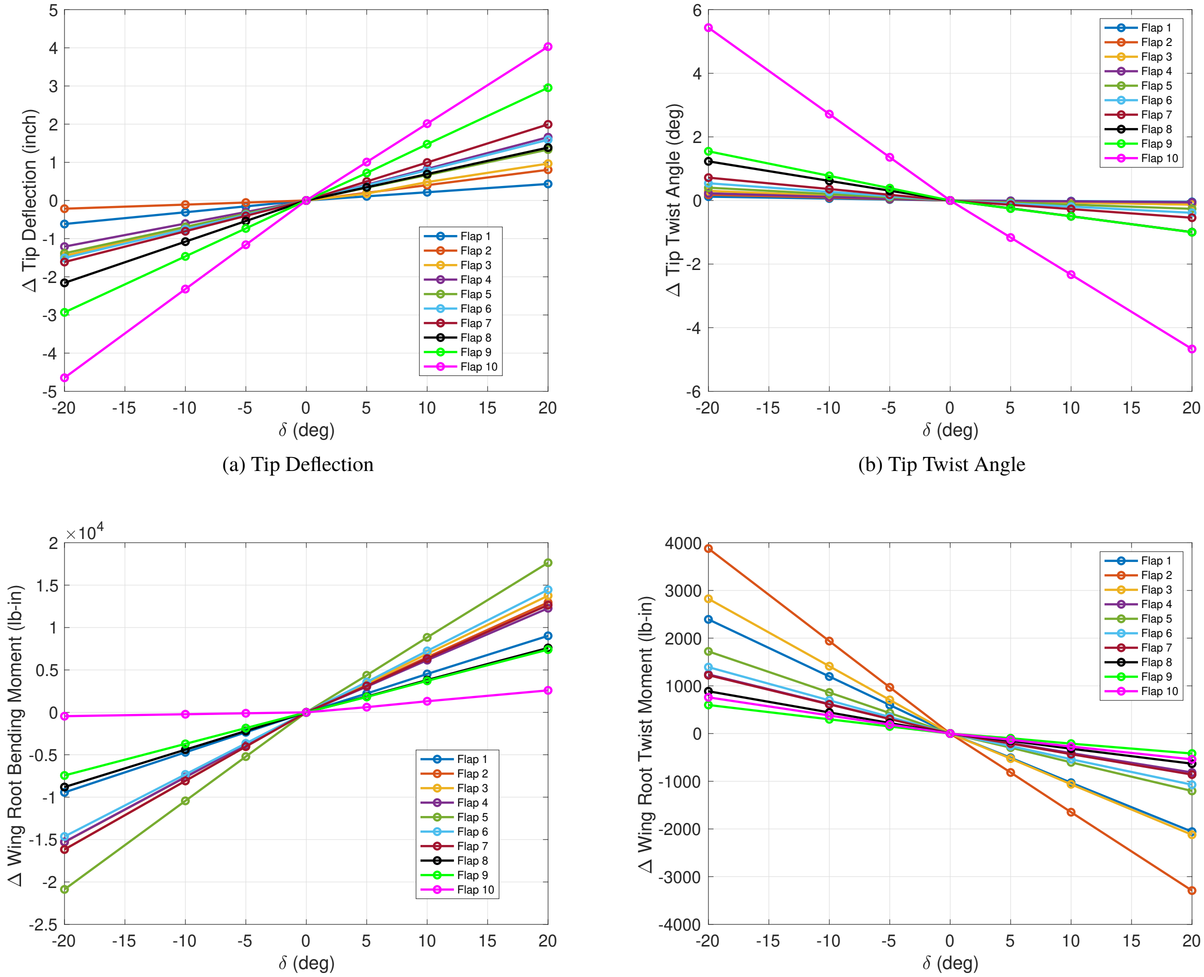

(a) Tip Deflection

(b) Tip Twist Angle

(c) Wing Root Bending Moment

(d) Wing Root Twist Moment

Figure 53 Incremental Structural Data for CRM at Mach 0.80, q_∞ = 230 psf, and α = −4°

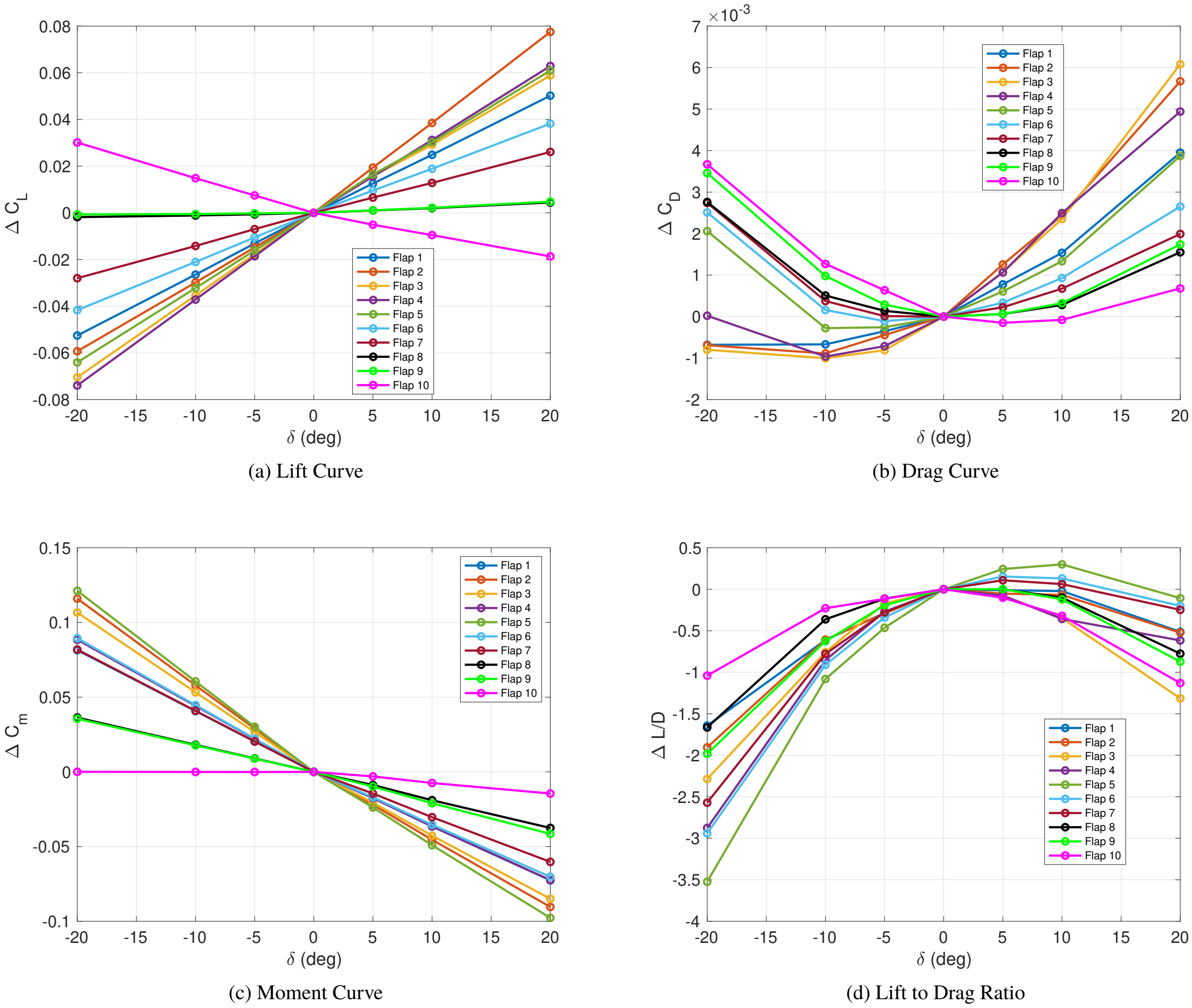

(a) Lift Curve

(b) Drag Curve

(c) Moment Curve

(d) Lift to Drag Ratio

Figure 54 Incremental Aerodynamic Data for CRM at Mach 0.80, $q_\infty = 230$ psf, and $\alpha = 0°$

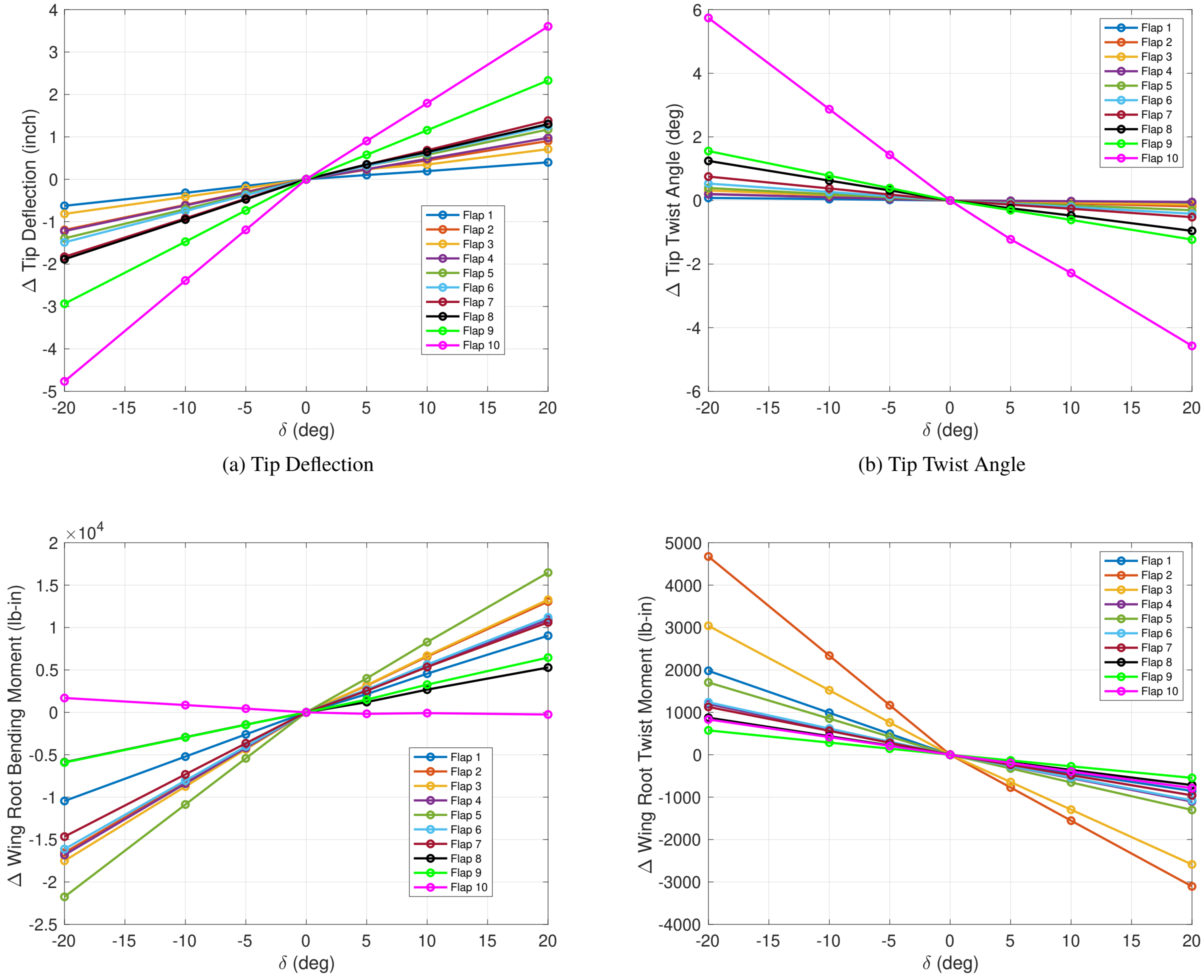

(a) Tip Deflection

(b) Tip Twist Angle

(c) Wing Root Bending Moment

(d) Wing Root Twist Moment

Figure 55 Incremental Structural Data for CRM at Mach 0.80, $q_\infty = 230$ psf, and $\alpha = 0°$

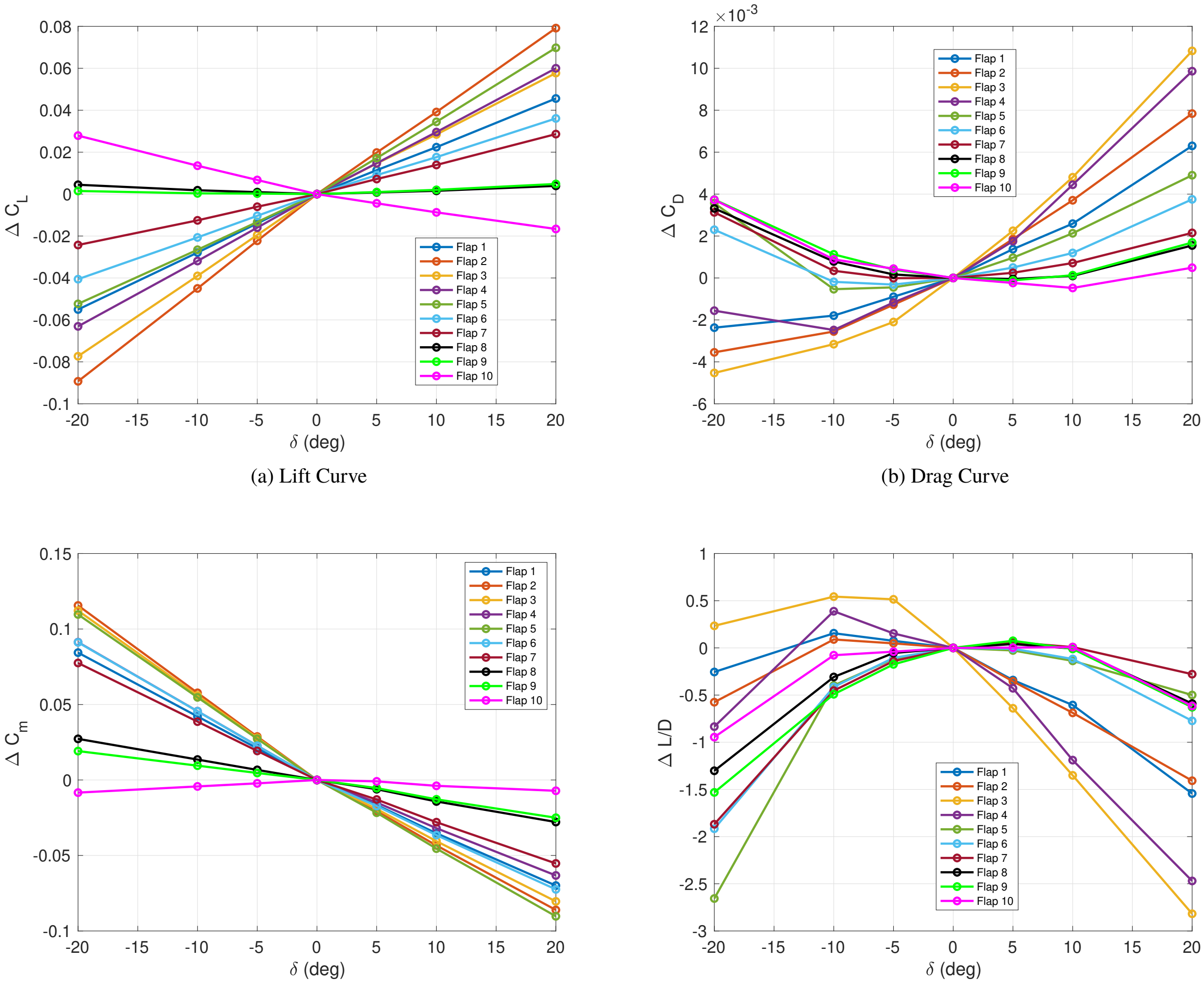

(a) Lift Curve

(b) Drag Curve

(c) Moment Curve

(d) Lift to Drag Ratio

Figure 56 Incremental Aerodynamic Data for CRM at Mach 0.80, $q_\infty = 230$ psf, and $\alpha = 4°$

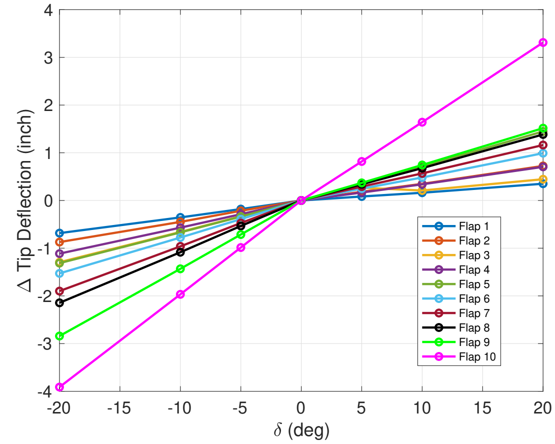

(a) Tip Deflection

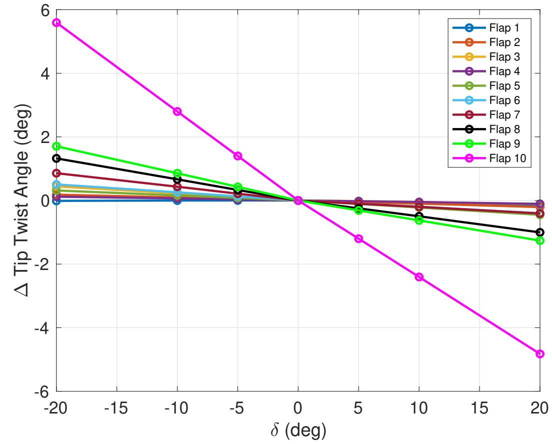

(b) Tip Twist Angle

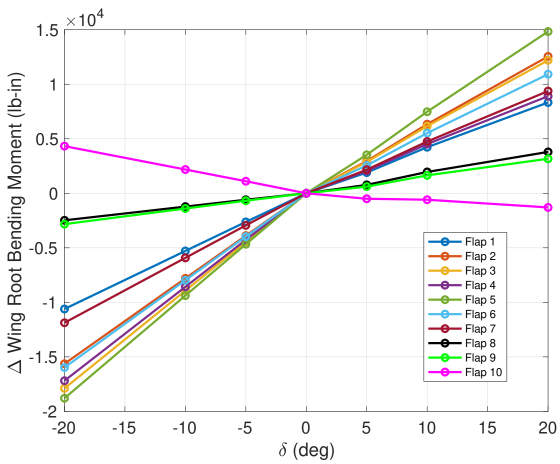

(c) Wing Root Bending Moment

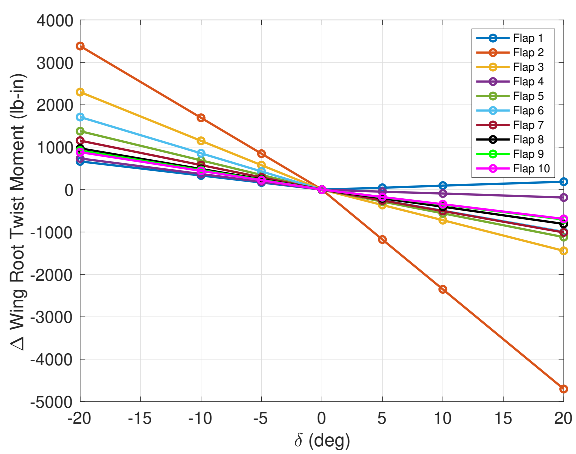

(d) Wing Root Twist Moment

Figure 57 Incremental Structural Data for CRM at Mach 0.80, $q_\infty = 230$ **psf, and** $\alpha = 4°$

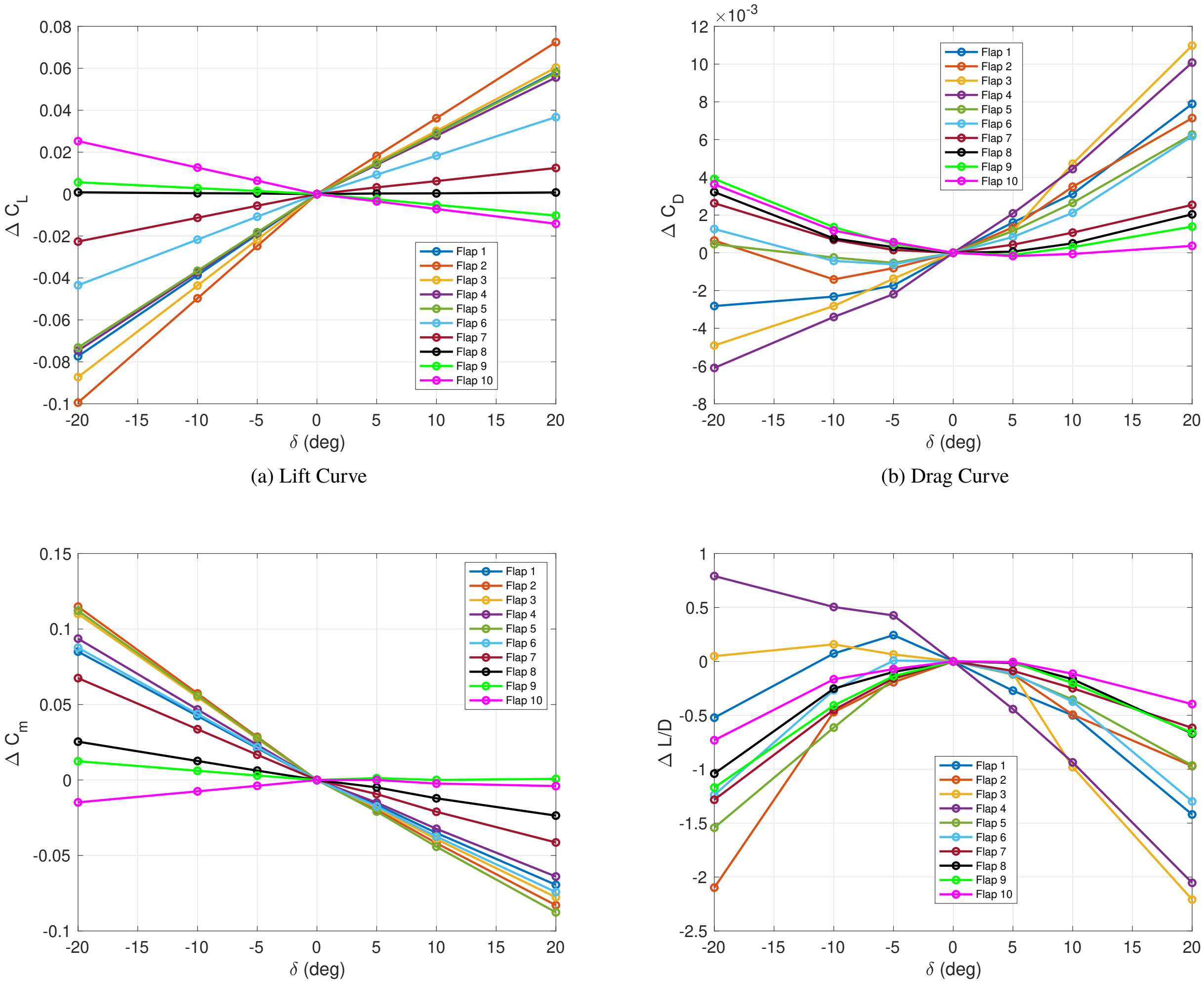

(a) Lift Curve

(b) Drag Curve

(c) Moment Curve

(d) Lift to Drag Ratio

Figure 58 Incremental Aerodynamic Data for CRM at Mach 0.80, $q_\infty = 230$ psf, and $\alpha = 6°$

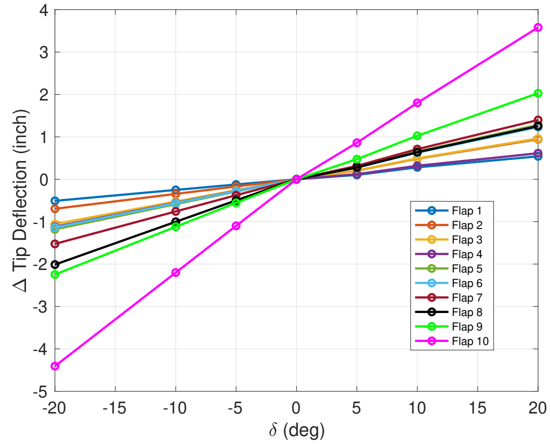

(a) Tip Deflection

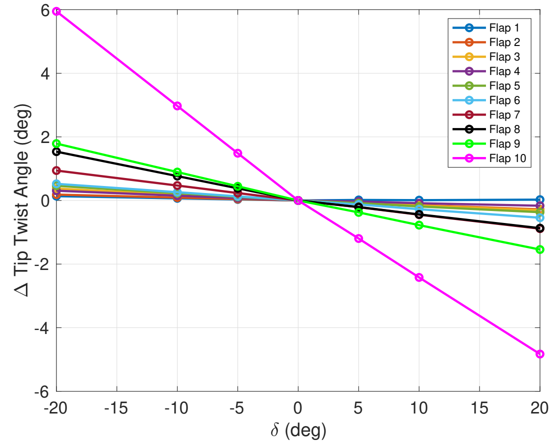

(b) Tip Twist Angle

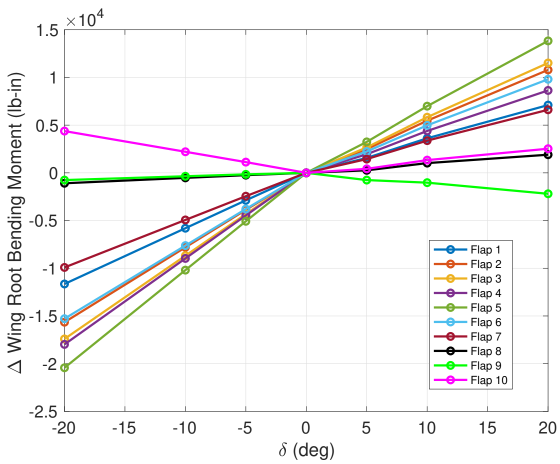

(c) Wing Root Bending Moment

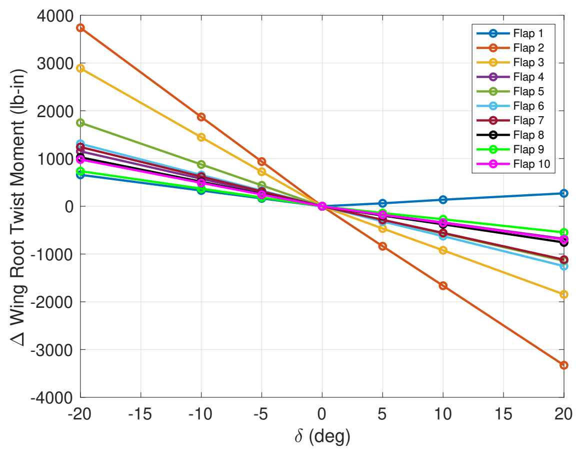

(d) Wing Root Twist Moment

Figure 59 Incremental Structural Data for CRM at Mach 0.80, q_∞ = 230 psf, and α = 6°

Appendix D

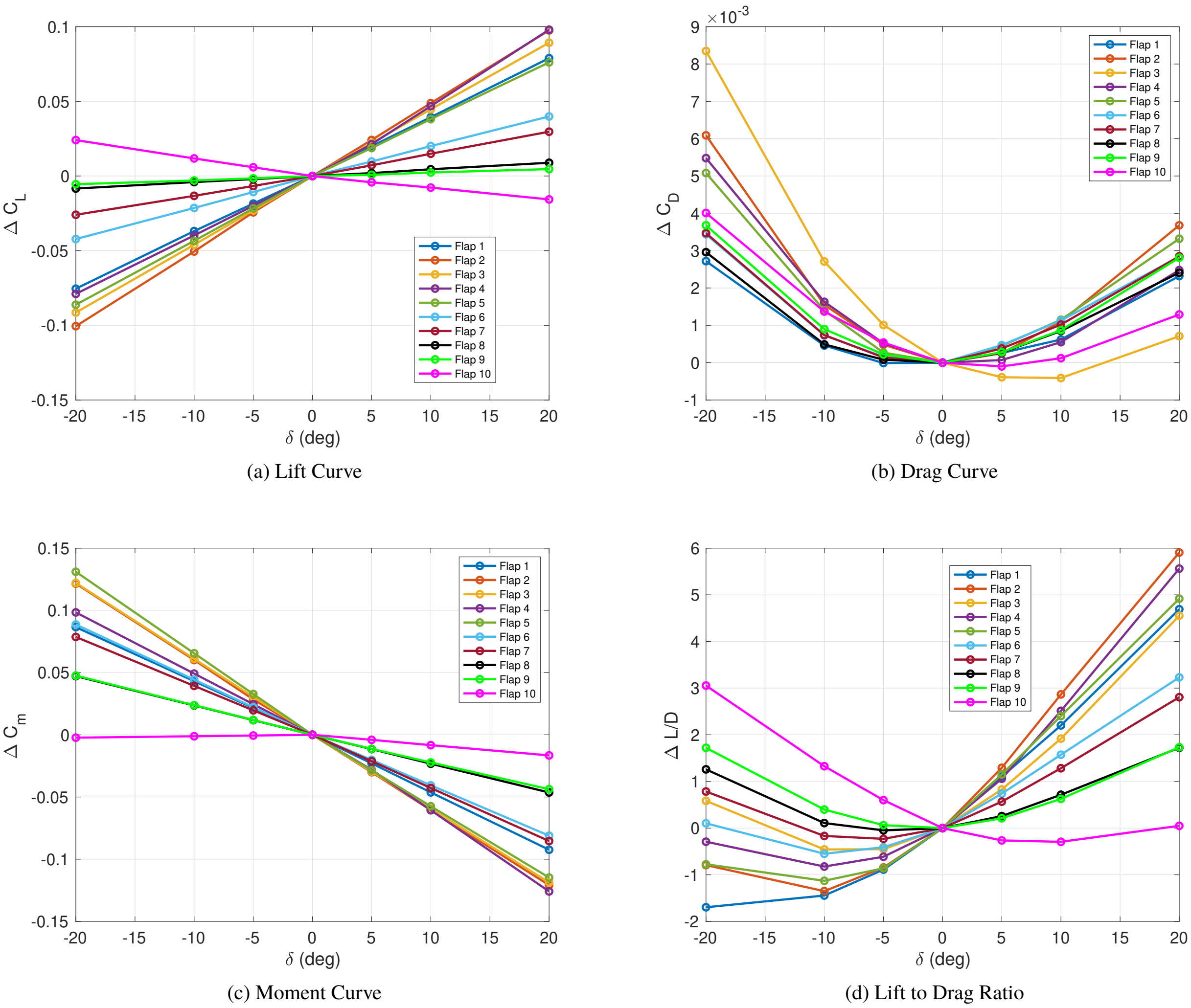

Figure 60 Incremental Aerodynamic Data for CRM at Mach 0.85, q_∞ = 230 psf, and $\alpha = -7°$

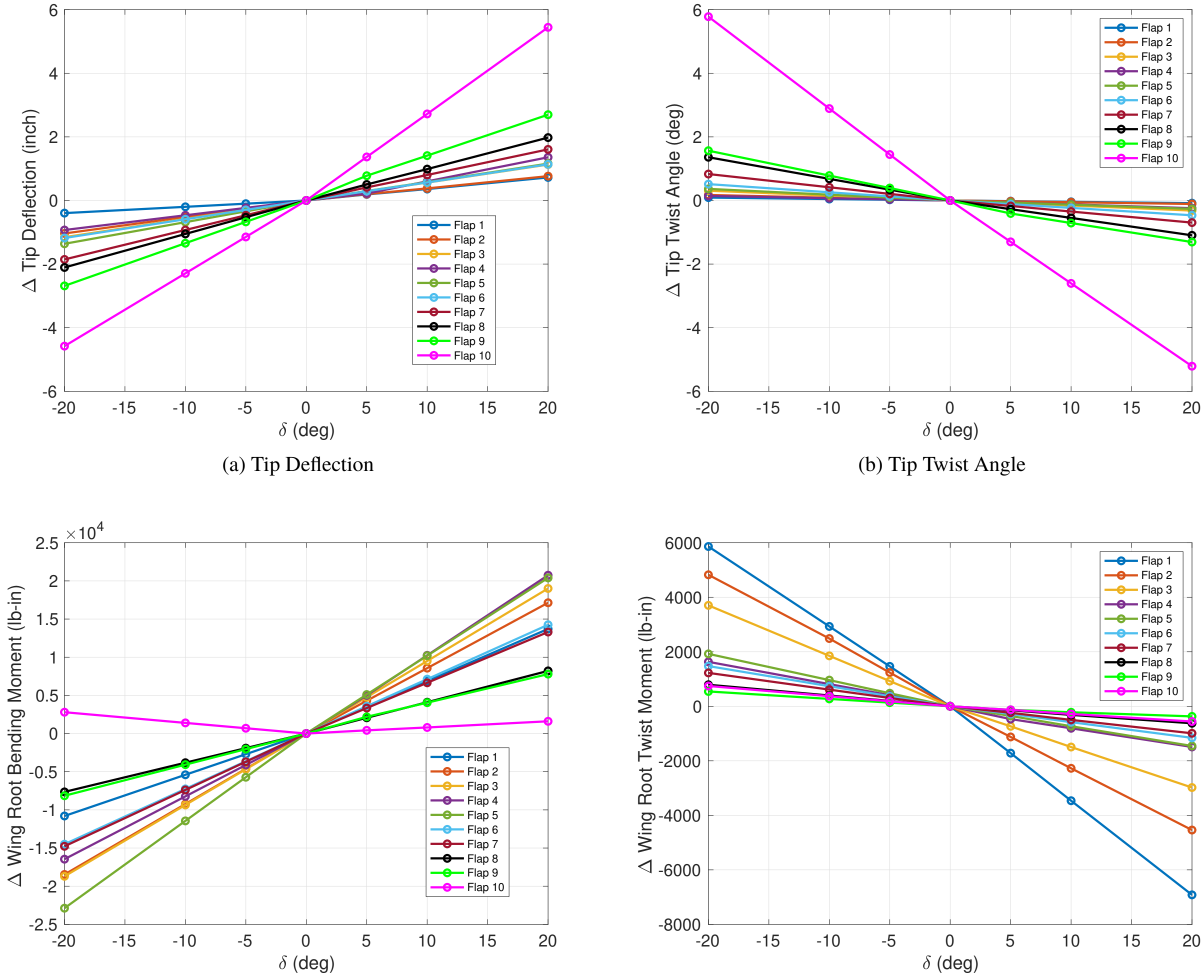

(a) Tip Deflection

(b) Tip Twist Angle

(c) Wing Root Bending Moment

(d) Wing Root Twist Moment

Figure 61 Incremental Structural Data for CRM at Mach 0.85, $q_\infty = 230$ psf, and $\alpha = -7°$

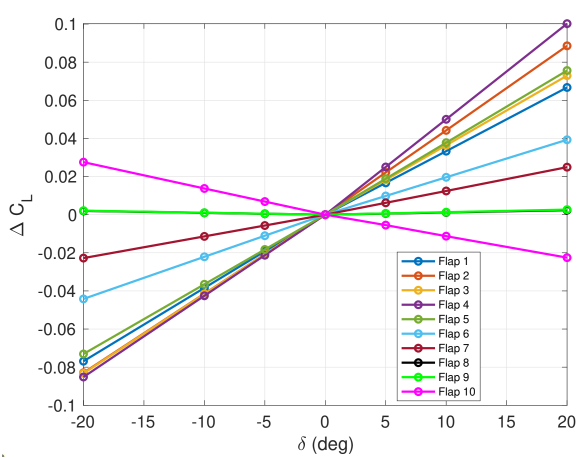

(a) Lift Curve

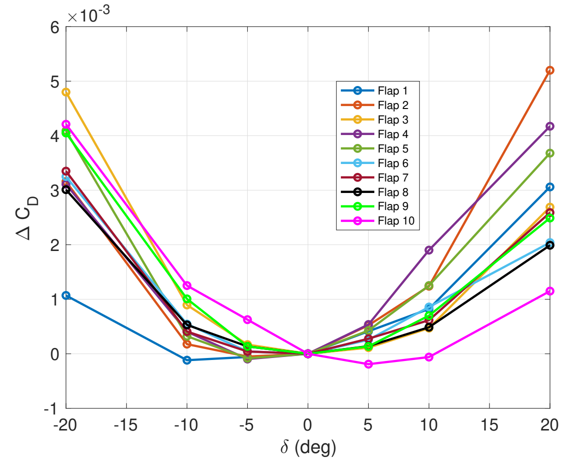

(b) Drag Curve

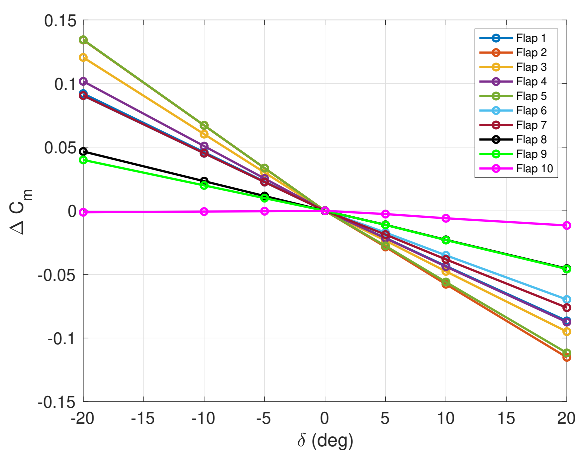

(c) Moment Curve

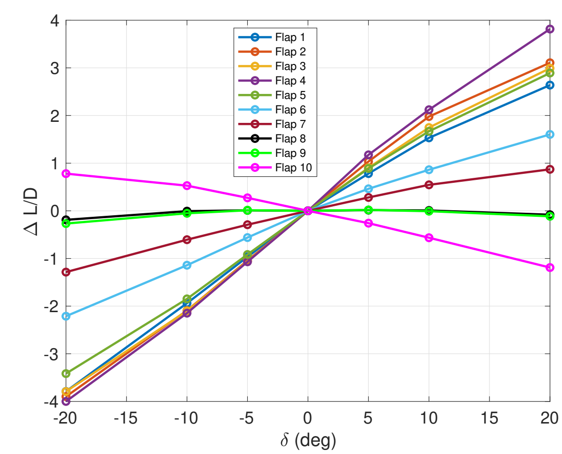

(d) Lift to Drag Ratio

Figure 62 Incremental Aerodynamic Data for CRM at Mach 0.85, $q_\infty = 230$ psf, and $\alpha = -4°$

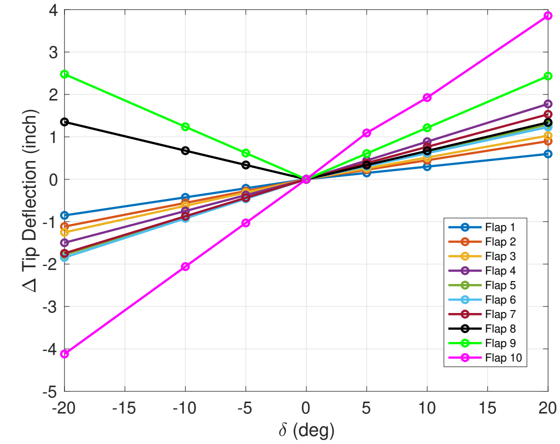

(a) Tip Deflection

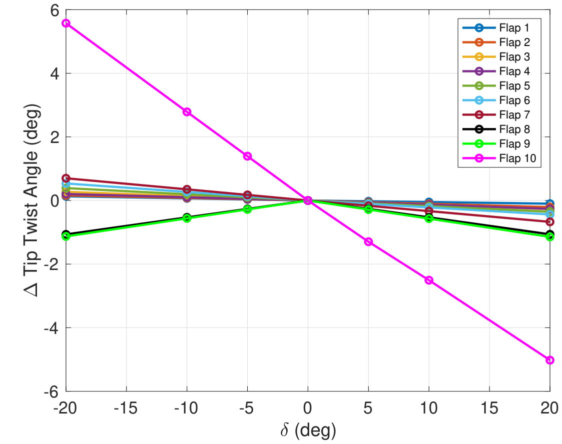

(b) Tip Twist Angle

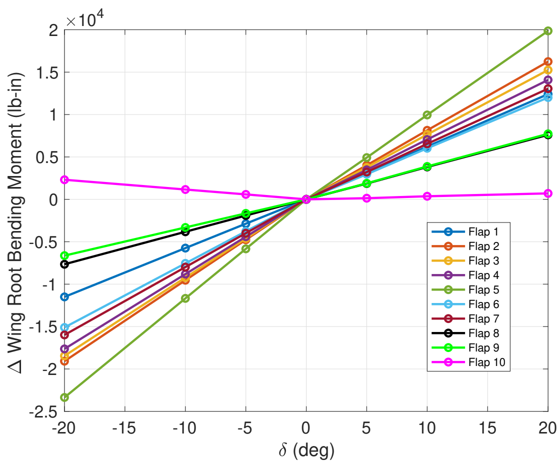

(c) Wing Root Bending Moment

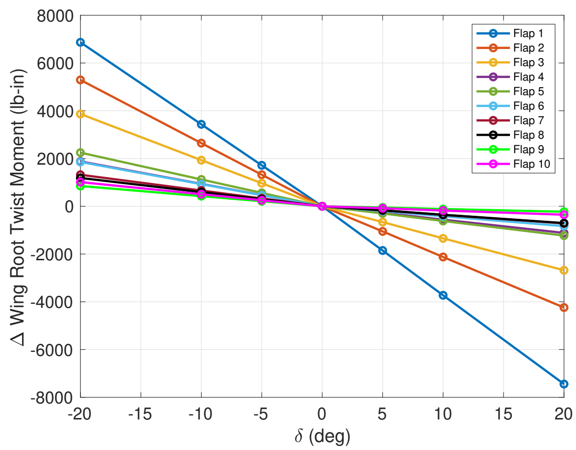

(d) Wing Root Twist Moment

Figure 63 Incremental Structural Data for CRM at Mach 0.85, $q_\infty = 230$ psf, and $\alpha = -4°$

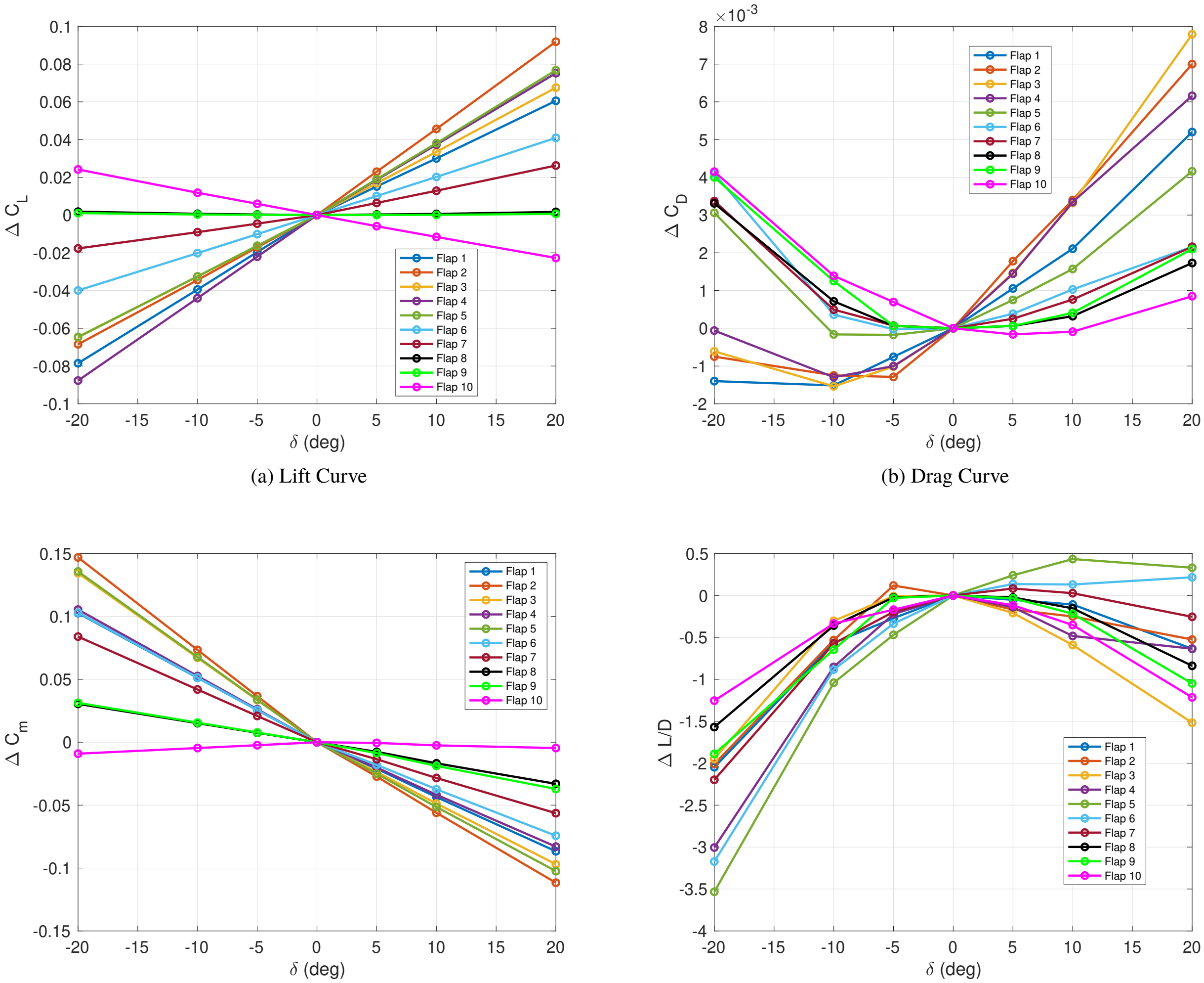

(a) Lift Curve

(b) Drag Curve

(c) Moment Curve

(d) Lift to Drag Ratio

Figure 64 Incremental Aerodynamic Data for CRM at Mach 0.85, $q_\infty = 230$ psf, and $\alpha = 0°$

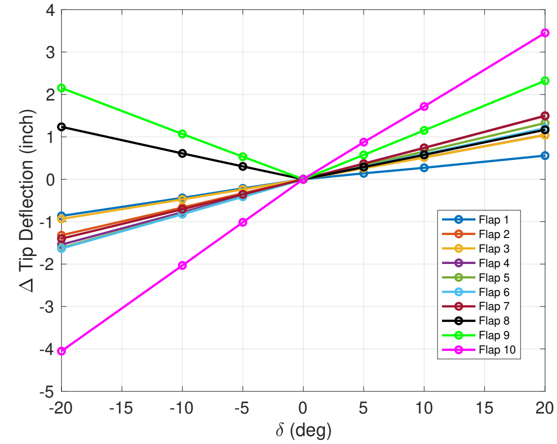

(a) Tip Deflection

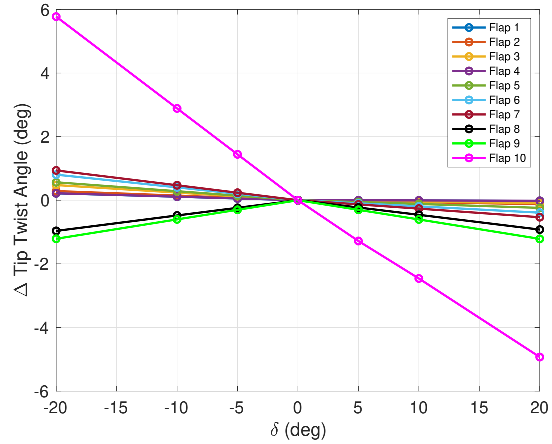

(b) Tip Twist Angle

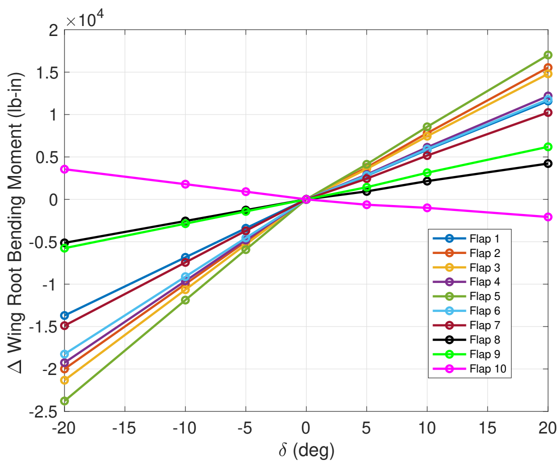

(c) Wing Root Bending Moment

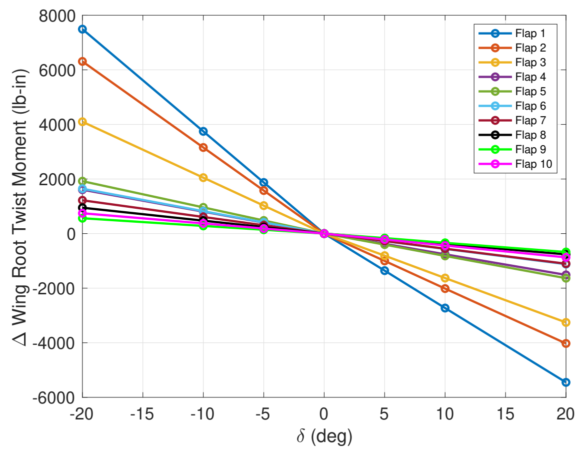

(d) Wing Root Twist Moment

Figure 65 Incremental Structural Data for CRM at Mach 0.85, $q_\infty = 230$ psf, and $\alpha = 0°$

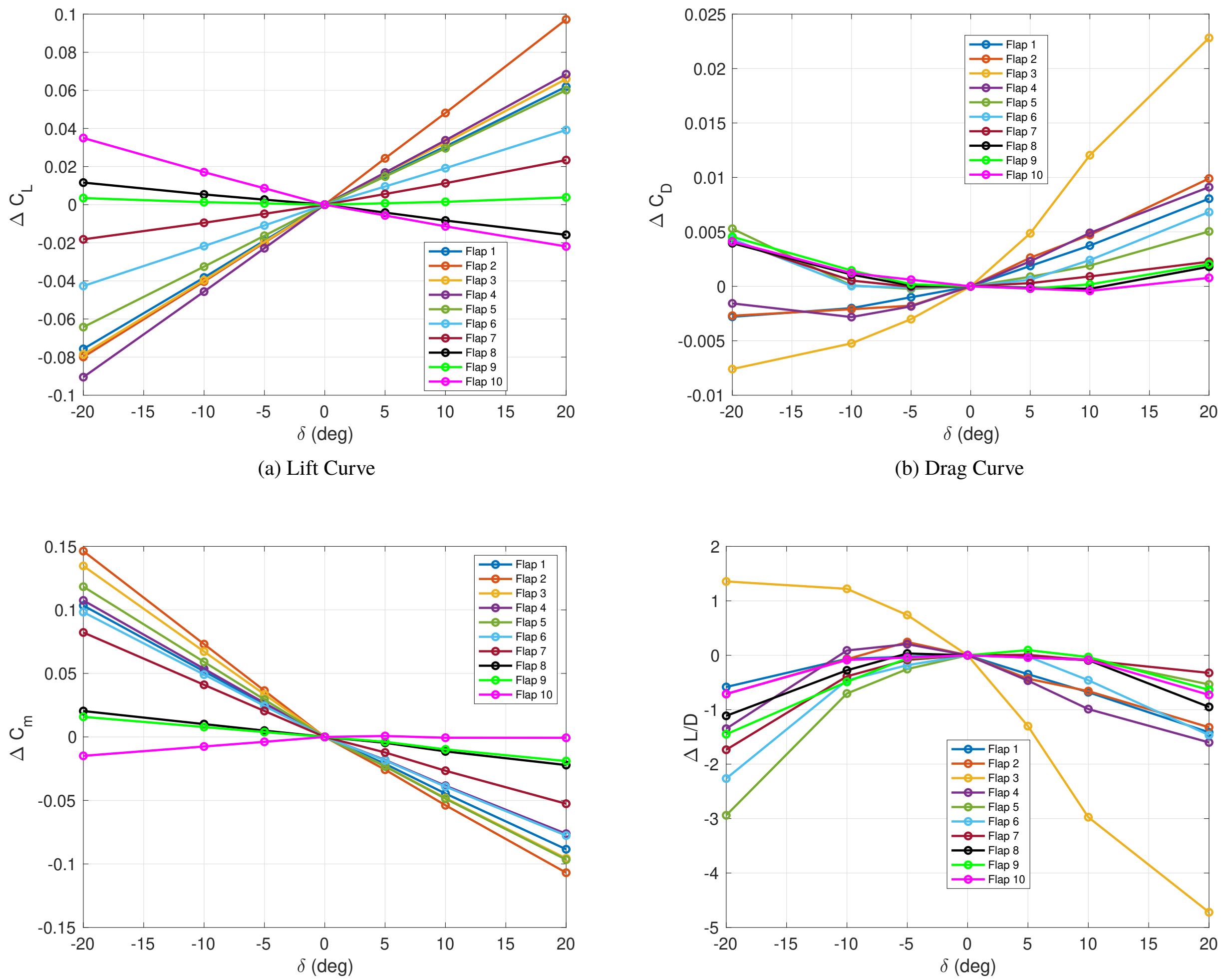

(a) Lift Curve

(b) Drag Curve

(c) Moment Curve

(d) Lift to Drag Ratio

Figure 66 Incremental Aerodynamic Data for CRM at Mach 0.85, q_∞ = 230 psf, and α = 4°

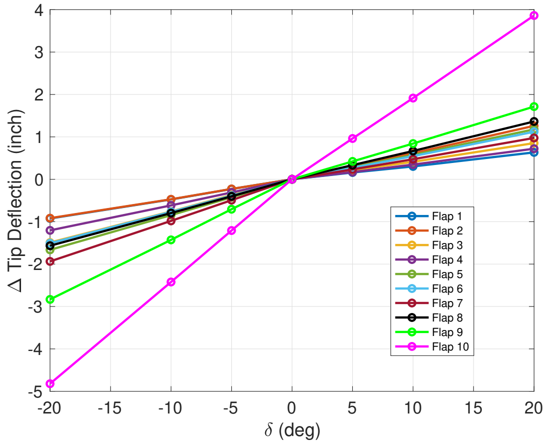

(a) Tip Deflection

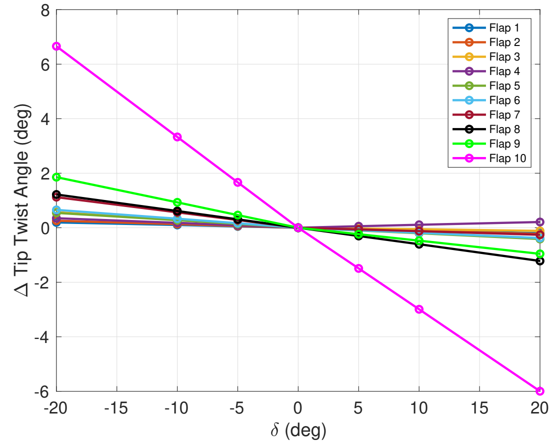

(b) Tip Twist Angle

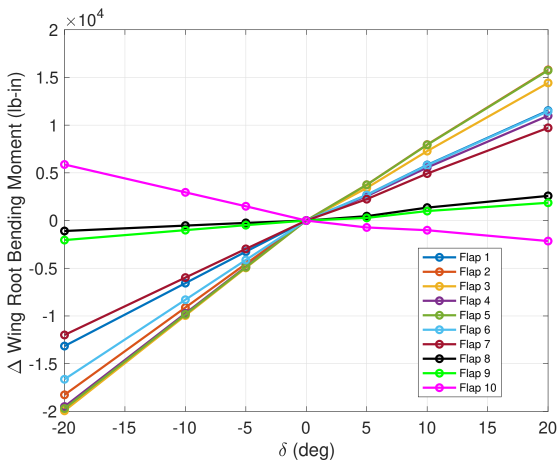

(c) Wing Root Bending Moment

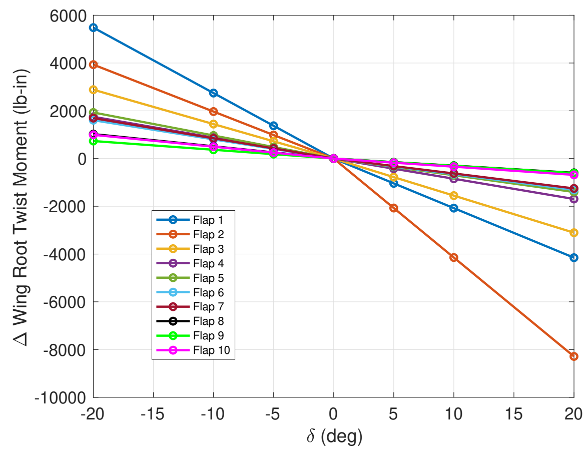

(d) Wing Root Twist Moment

Figure 67 Incremental Structural Data for CRM at Mach 0.85, q_∞ = 230 psf, and α = 4°

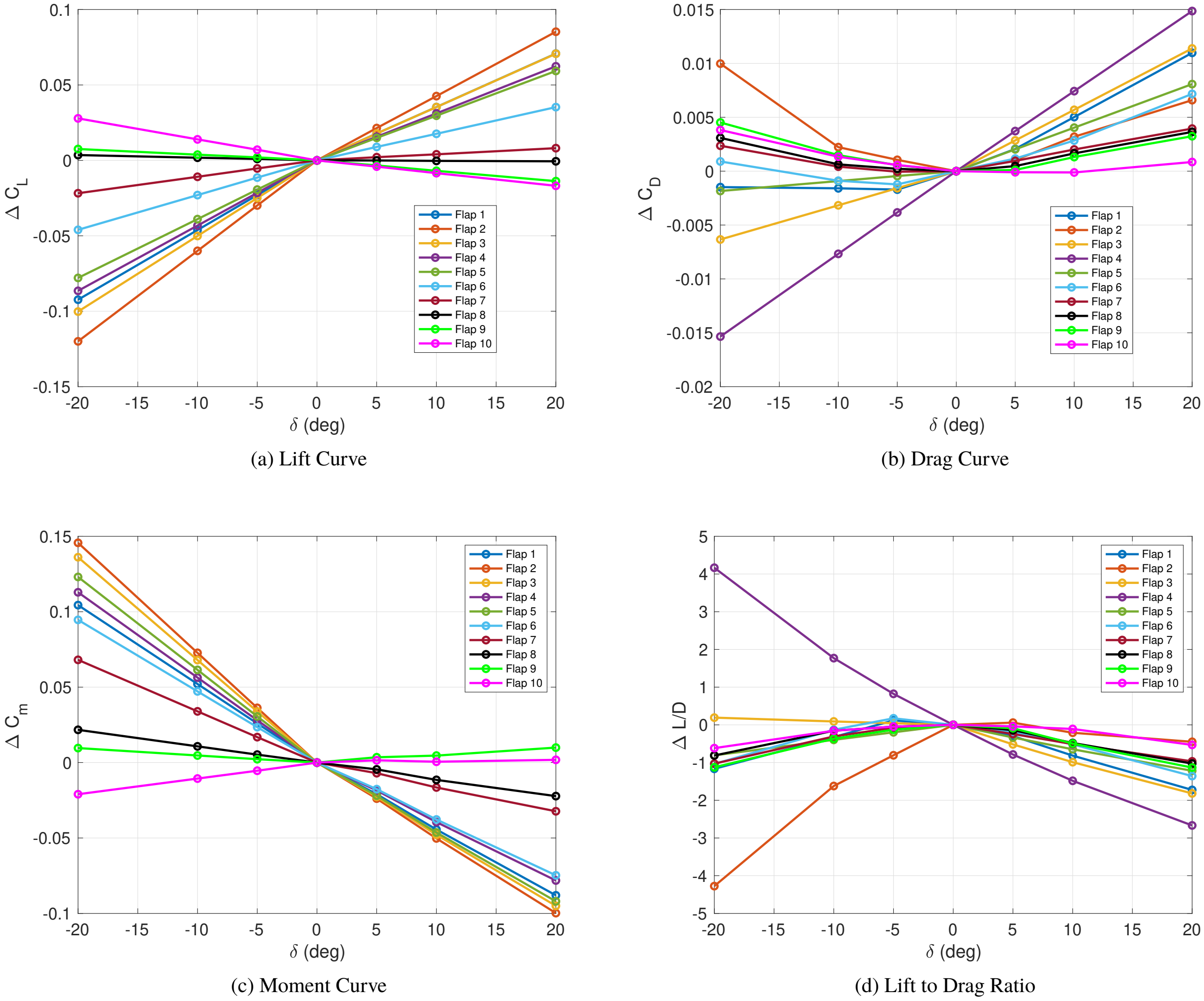

(a) Lift Curve

(b) Drag Curve

(c) Moment Curve

(d) Lift to Drag Ratio

Figure 68 Incremental Aerodynamic Data for CRM at Mach 0.85, $q_\infty = 230$ psf, and $\alpha = 6°$

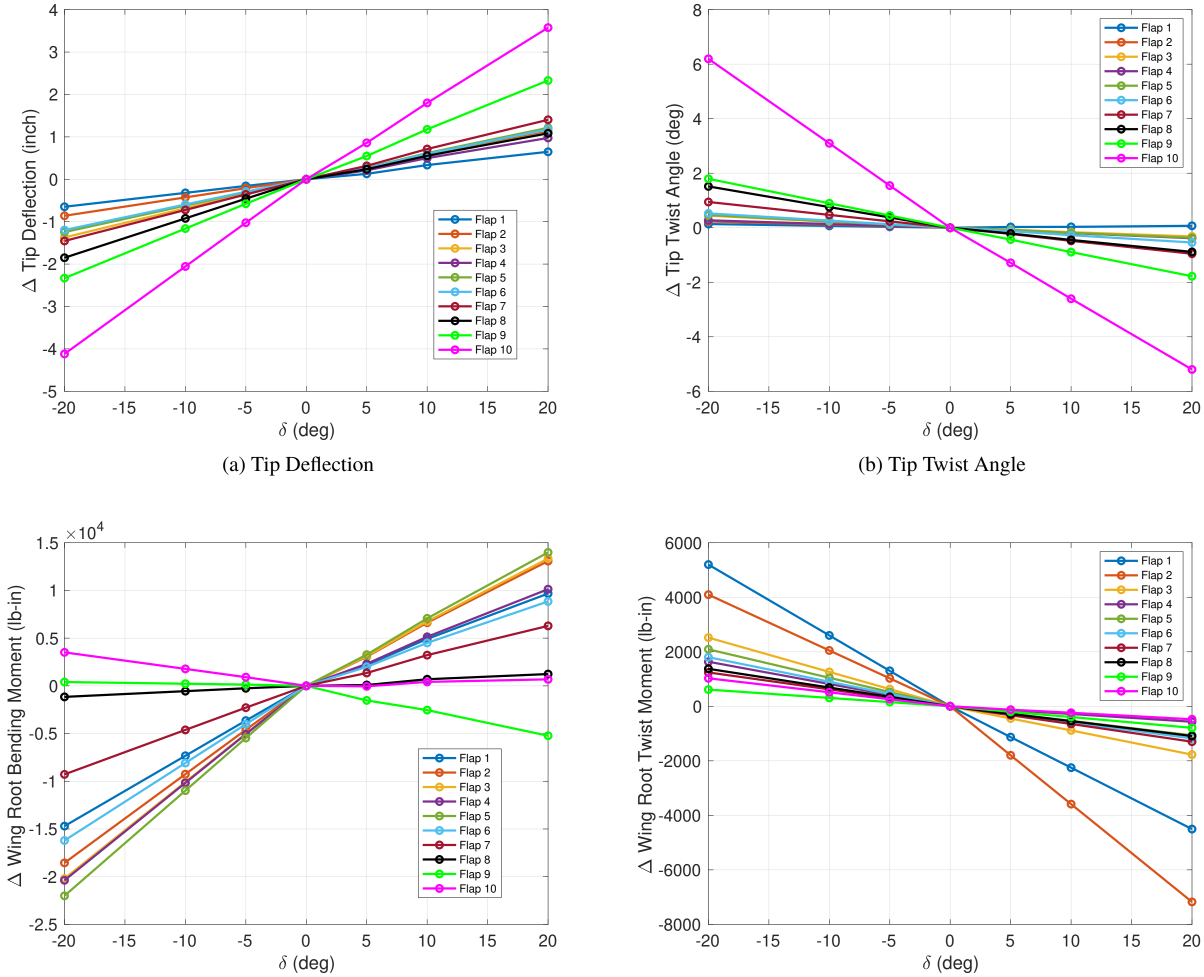

(a) Tip Deflection

(b) Tip Twist Angle

(c) Wing Root Bending Moment

(d) Wing Root Twist Moment

Figure 69 Incremental Structural Data for CRM at Mach 0.85, $q_\infty = 230$ psf, and $\alpha = 6°$

Appendix E

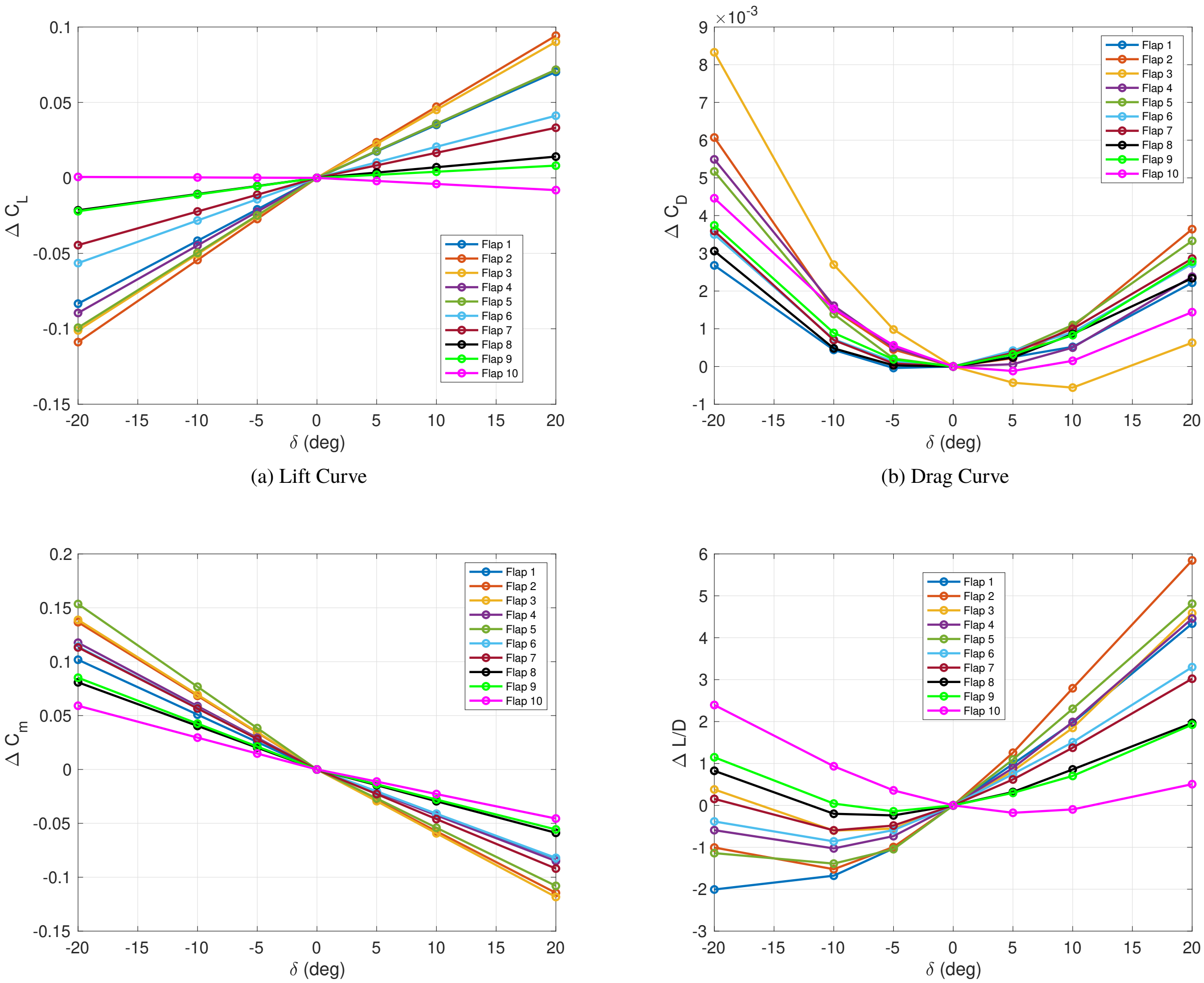

(a) Lift Curve
(b) Drag Curve
(c) Moment Curve
(d) Lift to Drag Ratio

Figure 70 Incremental Aerodynamic Data for CRM at Mach 0.85, q_∞ = 140 psf, and $\alpha = -7°$

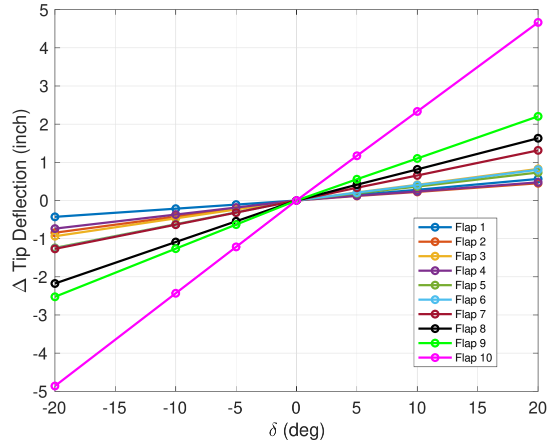

(a) Tip Deflection

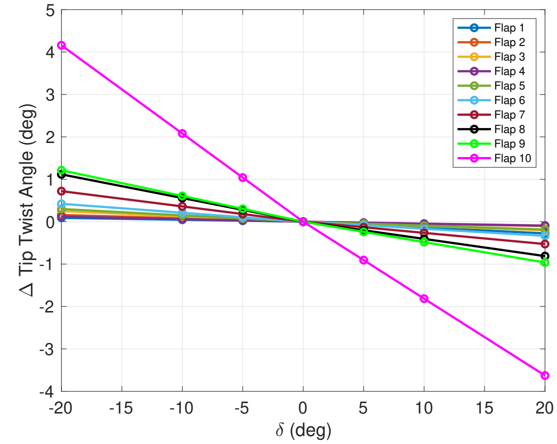

(b) Tip Twist Angle

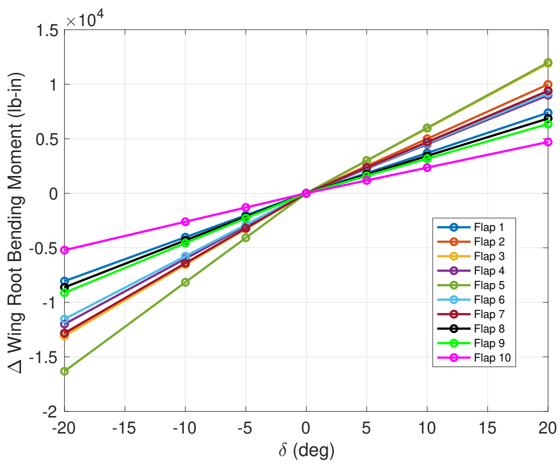

(c) Wing Root Bending Moment

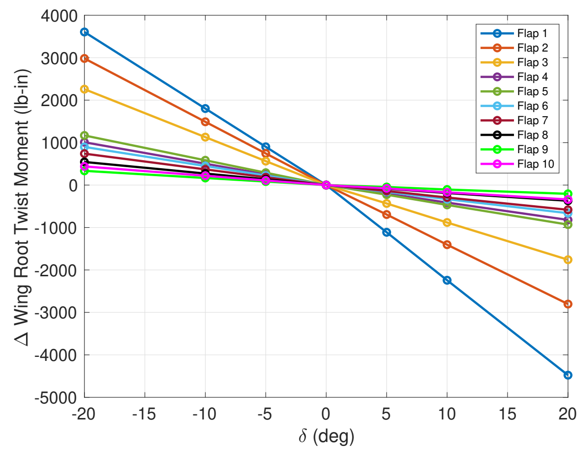

(d) Wing Root Twist Moment

Figure 71 Incremental Structural Data for CRM at Mach 0.85, $q_\infty = 140$ psf, and $\alpha = -7°$

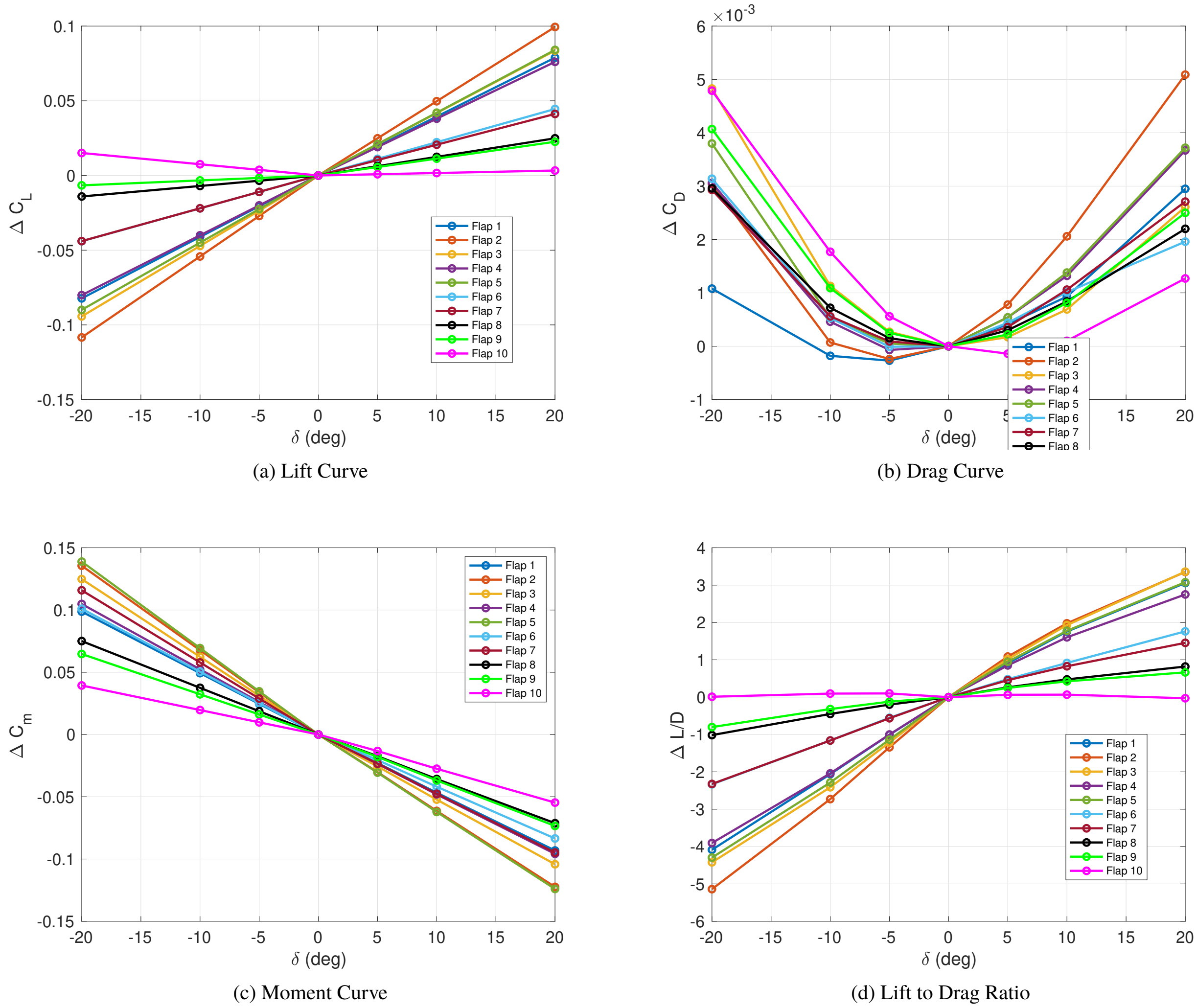

Figure 72 Incremental Aerodynamic Data for CRM at Mach 0.85, q_∞ = 140 psf, and α = −4°

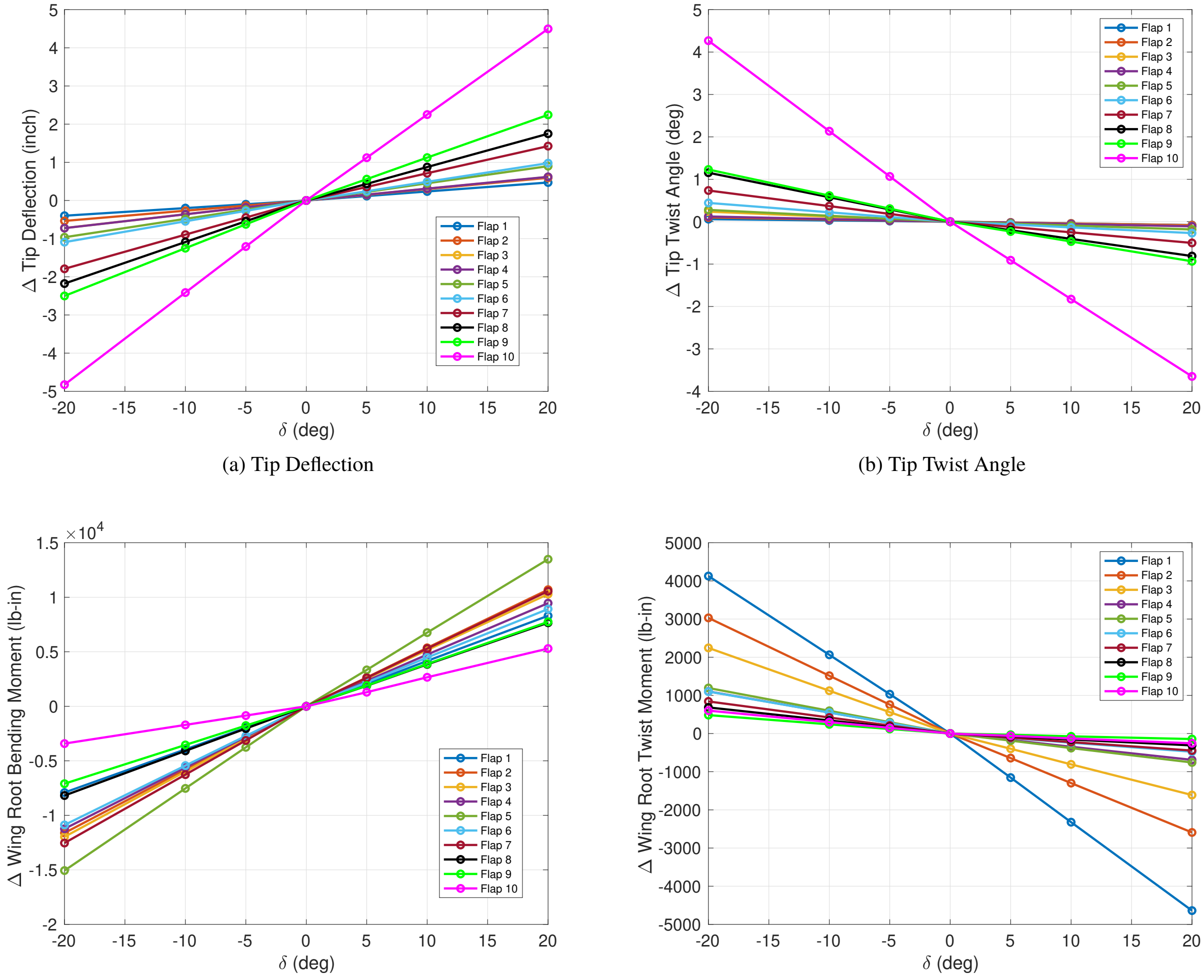

(a) Tip Deflection

(b) Tip Twist Angle

(c) Wing Root Bending Moment

(d) Wing Root Twist Moment

Figure 73 Incremental Structural Data for CRM at Mach 0.85, $q_\infty = 140$ psf, and $\alpha = -4°$

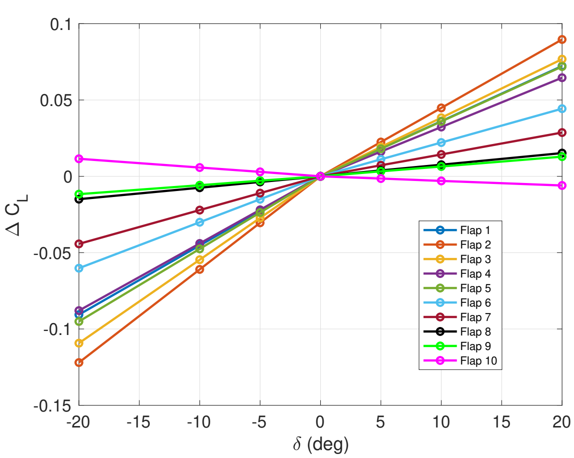

(a) Lift Curve

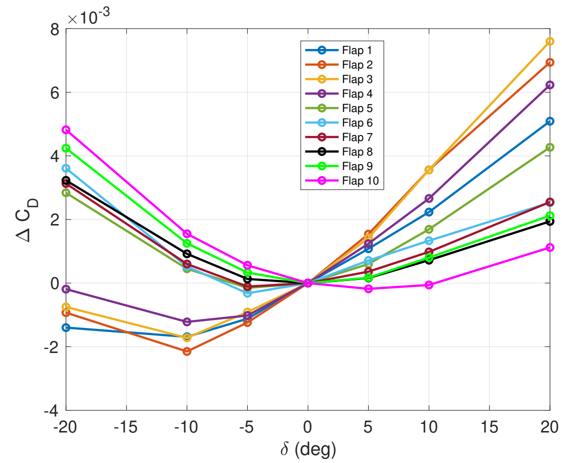

(b) Drag Curve

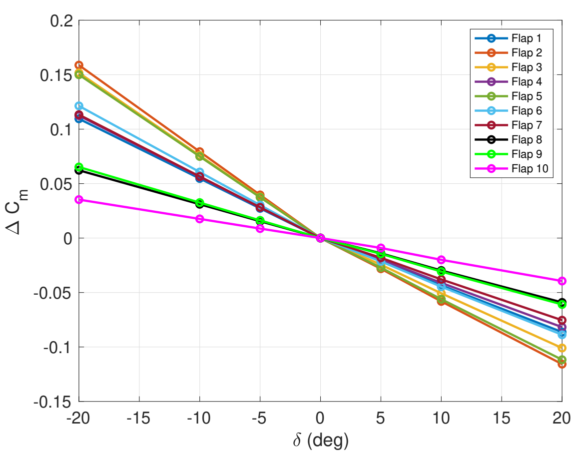

(c) Moment Curve

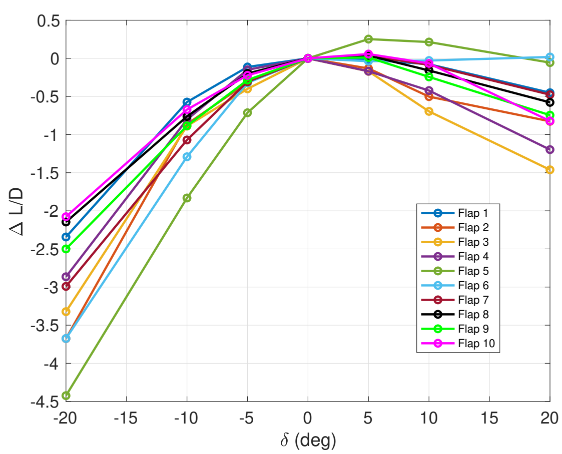

(d) Lift to Drag Ratio

Figure 74 Incremental Aerodynamic Data for CRM at Mach 0.85, $q_\infty = 140$ psf, and $\alpha = 0°$

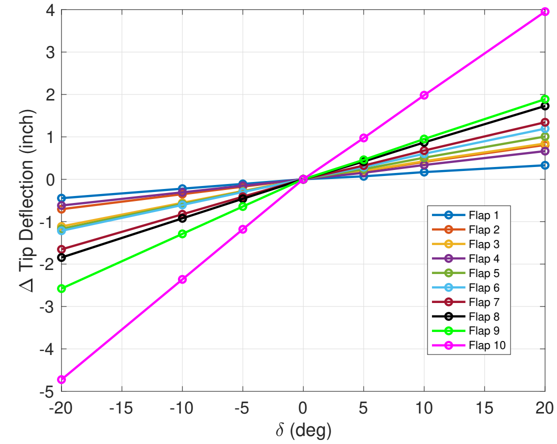

(a) Tip Deflection

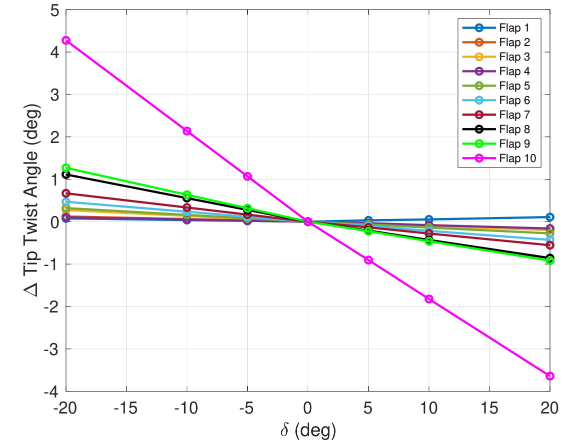

(b) Tip Twist Angle

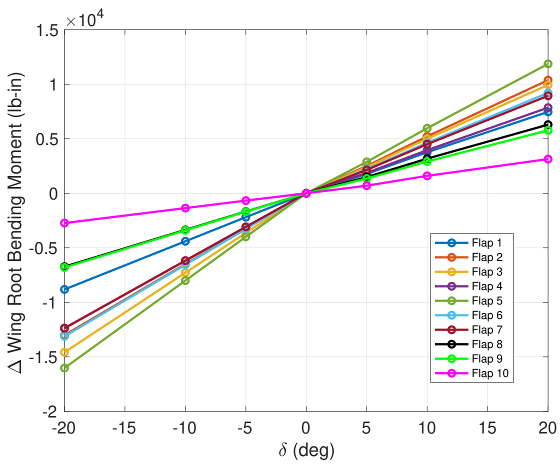

(c) Wing Root Bending Moment

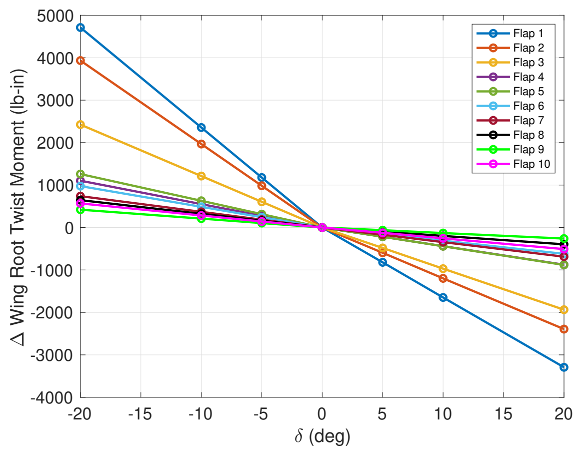

(d) Wing Root Twist Moment

Figure 75 Incremental Structural Data for CRM at Mach 0.85, $q_\infty = 140$ psf, and $\alpha = 0°$

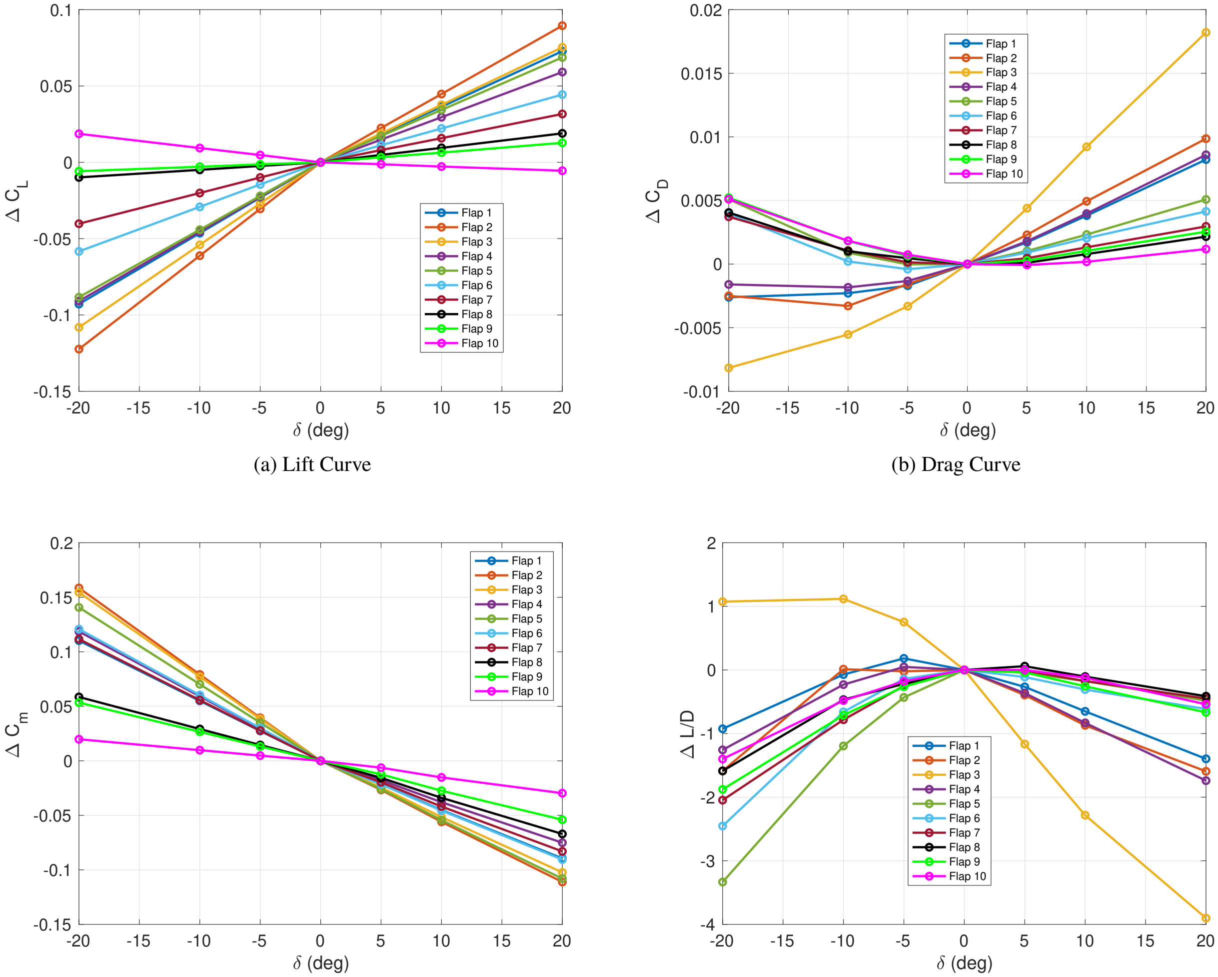

(a) Lift Curve

(b) Drag Curve

(c) Moment Curve

(d) Lift to Drag Ratio

Figure 76 Incremental Aerodynamic Data for CRM at Mach 0.85, $q_\infty = 140$ psf, and $\alpha = 4°$

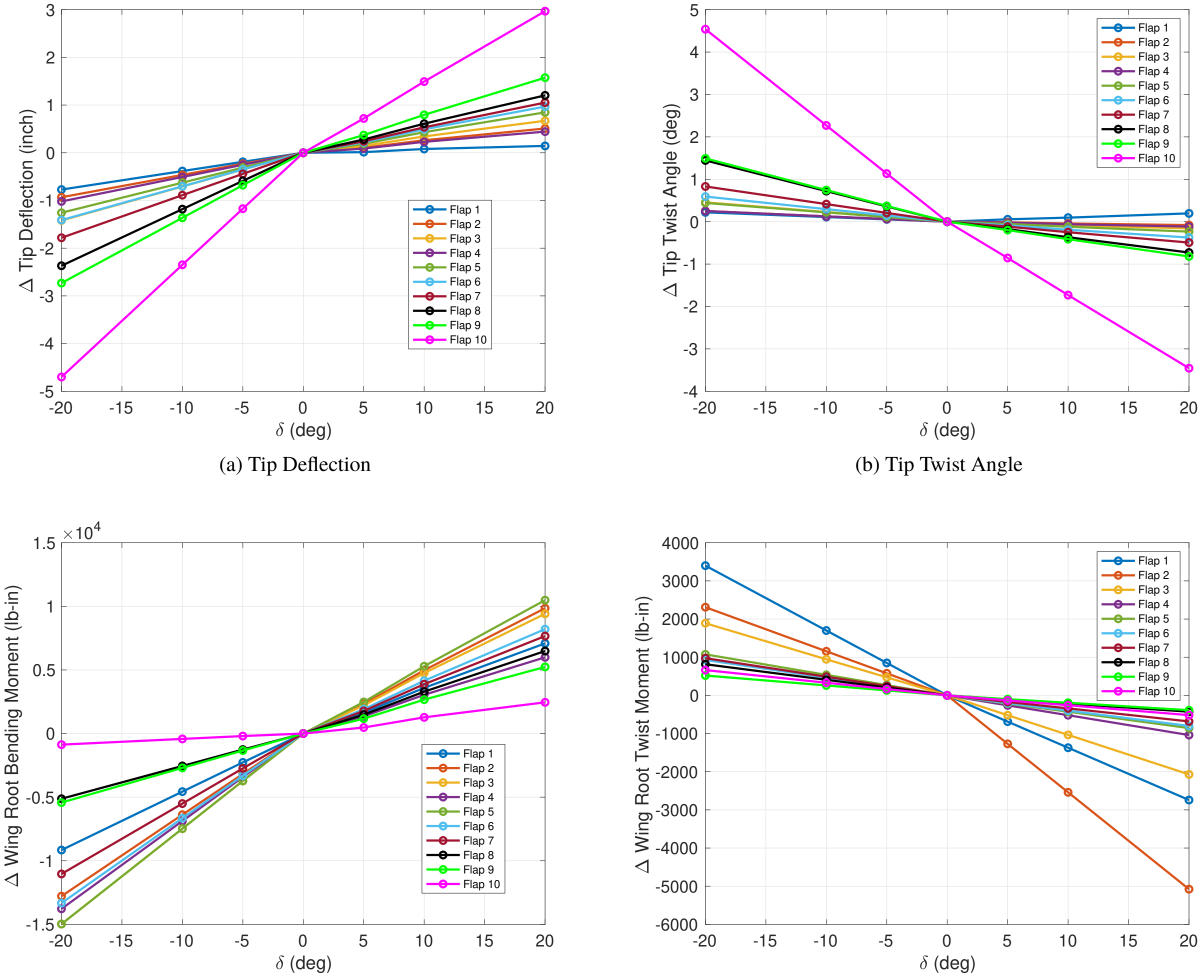

(a) Tip Deflection

(b) Tip Twist Angle

(c) Wing Root Bending Moment

(d) Wing Root Twist Moment

Figure 77 Incremental Structural Data for CRM at Mach 0.85, $q_\infty = 140$ psf, and $\alpha = 4°$

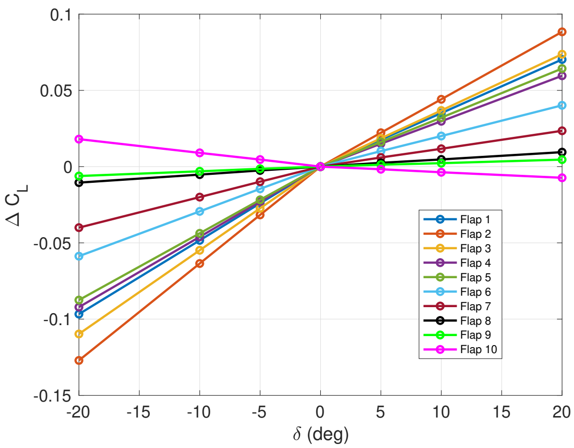

(a) Lift Curve

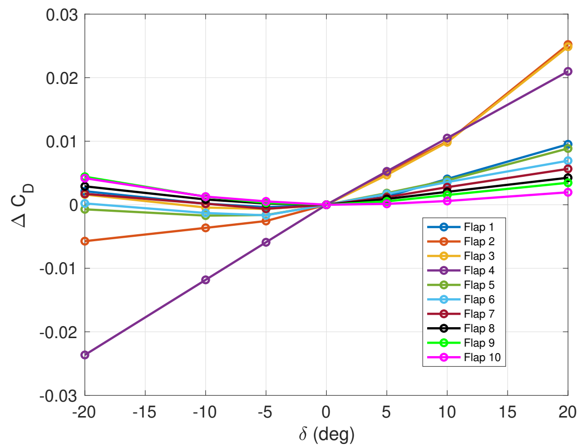

(b) Drag Curve

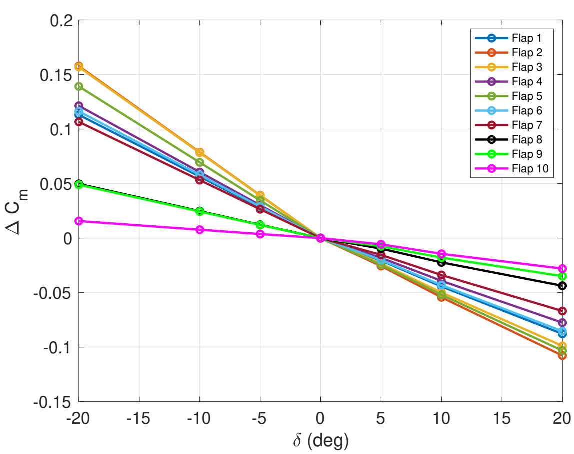

(c) Moment Curve

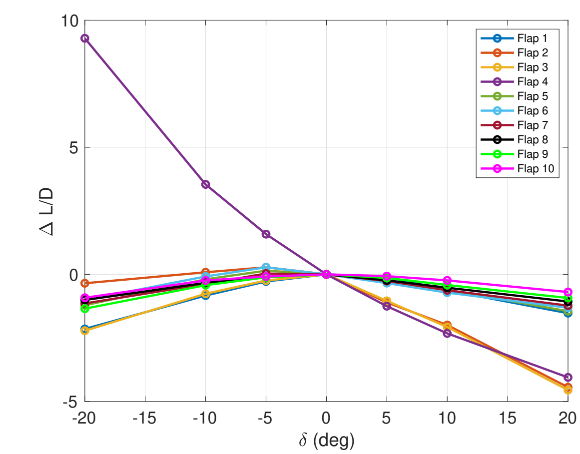

(d) Lift to Drag Ratio

Figure 78 Incremental Aerodynamic Data for CRM at Mach 0.85, $q_\infty = 140$ psf, and $\alpha = 6^\circ$

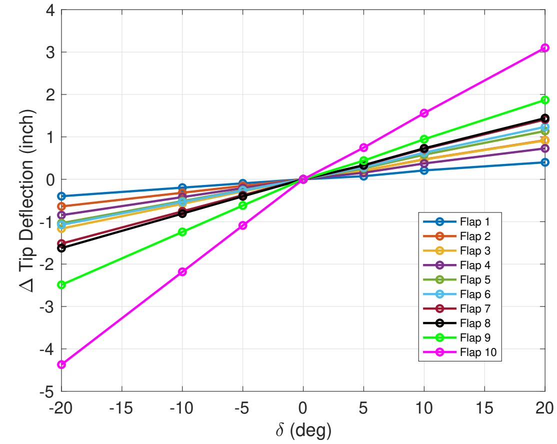

(a) Tip Deflection

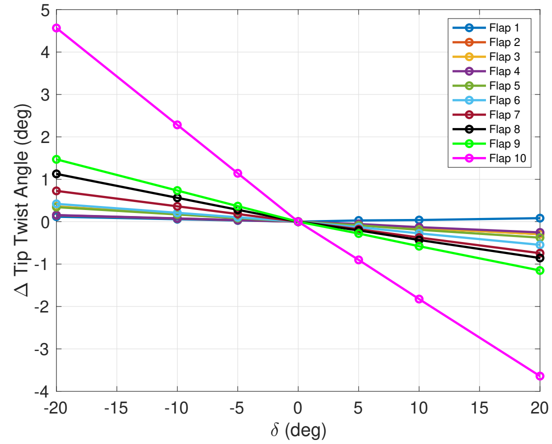

(b) Tip Twist Angle

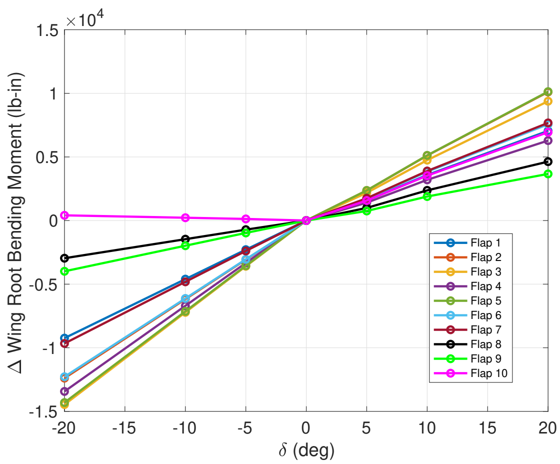

(c) Wing Root Bending Moment

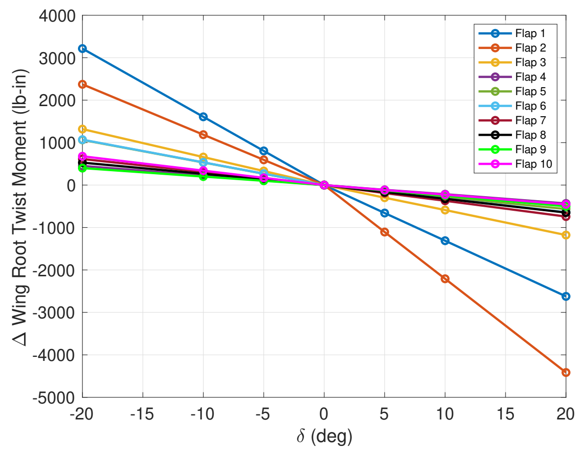

(d) Wing Root Twist Moment

Figure 79 Incremental Structural Data for CRM at Mach 0.85, $q_\infty = 140$ psf, and $\alpha = 6°$